FACOLTÀ DI SCIENZE MATEMATICHE, FISICHE E NATURALI
DIPARTIMENTO DI SCIENZE

Ph. D. in EARTH SCIENCE,
Curriculum in Geodynamics and Volcanology

Ph. D. THESIS

RECENT VOLCANO-TECTONIC EVOLUTION OF THE WESTERN GALÁPAGOS

SUPERVISOR:

Prof. Valerio Acocella
(Università degli Studi di Roma Tre)

CO-SUPERVISORS:

Marco Bagnardi, Ph.D.
(NASA Goddard Space Flight Center)

Prof. Andrew Hooper
(University of Leeds)

AUTHOR:

Federico Galetto

This Ph.D. thesis has been reviewed and approved by:

Prof. Sigurjón Jónsson, Ph.D.

(King Abdullah University of Science and Technology)

Prof. Freysteinn Sigmundsson, Ph.D.

(University of Iceland)

Academic year 2018-2019

Contents

Abstract

Calderas are the most active and dangerous volcanic systems on Earth. All active calderas experience periods of unrest characterized by changes in the baseline monitoring parameters, such as ground deformation, degassing and seismicity, which can last from hours to years. While only some unrest episodes culminate in eruption, most eruptions are preceded by unrest. Therefore, understanding the nature of unrest becomes fundamental to assess volcanic hazard and represents one of the main problems in volcanology. Active mafic calderas undergo repeated unrest episodes, often characterized by multiple and regular cycles of uplift, with pre-eruptive seismicity followed by eruption and co-eruptive deflation. Conversely, felsic calderas are restless for decades or show only isolated and short unrest episodes and erupt infrequently. Mafic calderas, therefore, provide simpler conditions to study unrest. In this group are the six active calderas of the western Galápagos (Ecuador), which share similar characteristics and experienced repeated unrest episodes in the last decades. This Ph.D. Thesis aims at widening the knowledge on the unrest episodes at the western Galápagos calderas and at extending such results to other mafic calderas with similar characteristics.

To pursue this aim, I first analysed eruptive and non-eruptive unrest episodes at two of the less studied calderas of the western Galápagos: Alcedo (article published in Journal of Geophysical Research-Solid Earth) and Cerro Azul (article submitted to Journal of Geophysical Research-Solid Earth). In these studies, I investigated the non-eruptive unrest episodes occurring from 2007 to 2011 at Alcedo and the 2008 eruptive unrest at Cerro Azul. As ground deformation is a constant feature in all the unrest episodes at western Galápagos calderas, I studied surface displacements as measured by Synthetic Aperture Radar Interferometry (InSAR). Then, by modelling the geodetic data, I placed constraints on the sources responsible for these episodes of unrest, as has been done for most of the previous studies of unrest episodes at other western Galápagos calderas. The new results highlight how Alcedo experienced two episodes of uplift due to new magma injections in its shallow magmatic system, separated by an episode with a limited lateral propagation of magma, probably interrupted by the lack of new magma supply to the magmatic system. The same results also hint at a possible relationship between these short-term unrest episodes and the longer-term process of caldera resurgence at Alcedo. The 2008 eruptive unrest of Cerro Azul started with eight months of pre-eruptive uplift of the caldera floor, followed, from May to June 2008, by two eruptive phases related to the lateral propagation of a radial dike. To interpret InSAR phase in terms of a geophysical model it is necessary to estimate the integer ambiguities in the phase through the phase unwrapping process. This is generally done prior to geophysical inversion, but any phase-unwrapping errors will bias the resulting geophysical parameters. To overcome the limiting presence of unwrapping errors affecting

some of the InSAR data of Cerro Azul we have developed a new method to directly invert the wrapped interferometric phase by estimating the integer ambiguities simultaneously with the geophysical parameters.

Finally, I reviewed all the geodetically monitored unrest episodes at the western Galápagos calderas, mainly considering the estimated injected volumes of magma and the related intrusive rates (results included in a not-yet-submitted manuscript). These data were compared to those from other mafic calderas sharing similar characteristics, to find a consistent behaviour. Results highlight a relationship between the rates at which magma is injected inside the shallow magmatic system and the possibility to trigger a magmatic intrusion. In particular, unrest episodes with injection rates > 5 $x10^{-2}$ km^3/year seem to promote the propagation of a dike (eruptive or not) in < 1 year, while rates <9 $x10^{-3}$ km^3/year do not trigger any dike propagation in <1 year and, even over longer time spans, the formation of a dike seems uncommon. Therefore, these data suggest that the rates at which magma is supplied in the shallow system may provide an important informative parameter for the forecast of how the unrest will evolve in a mafic caldera with a shallow magmatic system.

Chapter 1

1- Introduction

Calderas are broad subcircular volcanic depressions resulting from the partial or complete emptying of a shallow reservoir as a consequence of an eruption (Pinatubo, 1991; Stix & Kobayashi, 2008) or of the lateral migration of magma, as for example occurred in 1968 at Fernandina (Galápagos, Ecuador), in 2000 at Miyakejima (Japan) and in 2014‑2015 at Bardarbunga, Iceland (Heiken & McCoy, 1984; Geishi et al., 2002; Gudmundsson et al., 2016; Howard et al., 2018). Calderas can be found in all volcanic environments and are probably the most complex and dangerous type of volcano, with the possibility of triggering the largest catastrophic eruptions and of developing eruptive vents both inside and outside the caldera, along the flank of the volcanic edifice (Lipman, 1984; Cole et al., 2005; Bagnardi et al., 2013; Acocella et al., 2015; Di Vito et al., 2016).

All active calderas have experienced periods of unrest, characterized by a deviation from baseline monitoring parameters, such as changes in seismicity, degassing, and ground deformation, lasting from a few hours to several years (Figure 1; Newhall & Dzurisin, 1988; Acocella et al., 2015; Robertson and Kilburn, 2016). Most of the unrest episodes have a magmatic origin, involving the deep or shallow movement of magma, even if sometimes unrest can be triggered by hydrothermal or tectonic processes (Newhall & Dzurisin, 1988; Chiodini & Frondini, 2001; Hill et al., 2002; Gottsmann et al., 2007; Acocella et al., 2015). Unrest can end in different ways (Figure 1). It can terminate with the storage of new magma inside the magmatic system, with the caldera that progressively returns to its quiescence stage (Figure 1b; e.g. Darwin, Galápagos; Amelung et al., 2000). Otherwise, unrest can culminate with the propagation of magma towards the surface (Figure 1a). In this case, two possibilities may occur: a) the propagating magma gets arrested and unrest becomes non-eruptive (Figure 1 a’’; e.g. Fernandina in 2007; Bagnardi & Amelung, 2012), with the caldera progressively returning to its quiescence state; b) the propagating magma reaches the surface, leading to eruption (Figure 1 a’; e.g. Rabaul, Papua New Guinea; Robertson & Kilburn, 2016) (Figure 1). Unrest, therefore, can culminate with an eruption or not. However, any eruption is always preceded by unrest, indicating that unrest is a necessary but not sufficient condition to have an eruption (Moran et al., 2011; Biggs et al., 2014; Acocella et al., 2015; Sandri et al., 2017). Therefore, understanding the nature of unrest becomes fundamental when assessing volcanic hazard, and determining its outcome represents one of the main challenges for volcanology (Acocella et al., 2015). To pursue this aim, it is equally important to try to understand the processes leading to eruptive unrest

and those leading to non-eruptive unrest, in order to evaluate and possibly forecast the potential eruptibility of unrest.

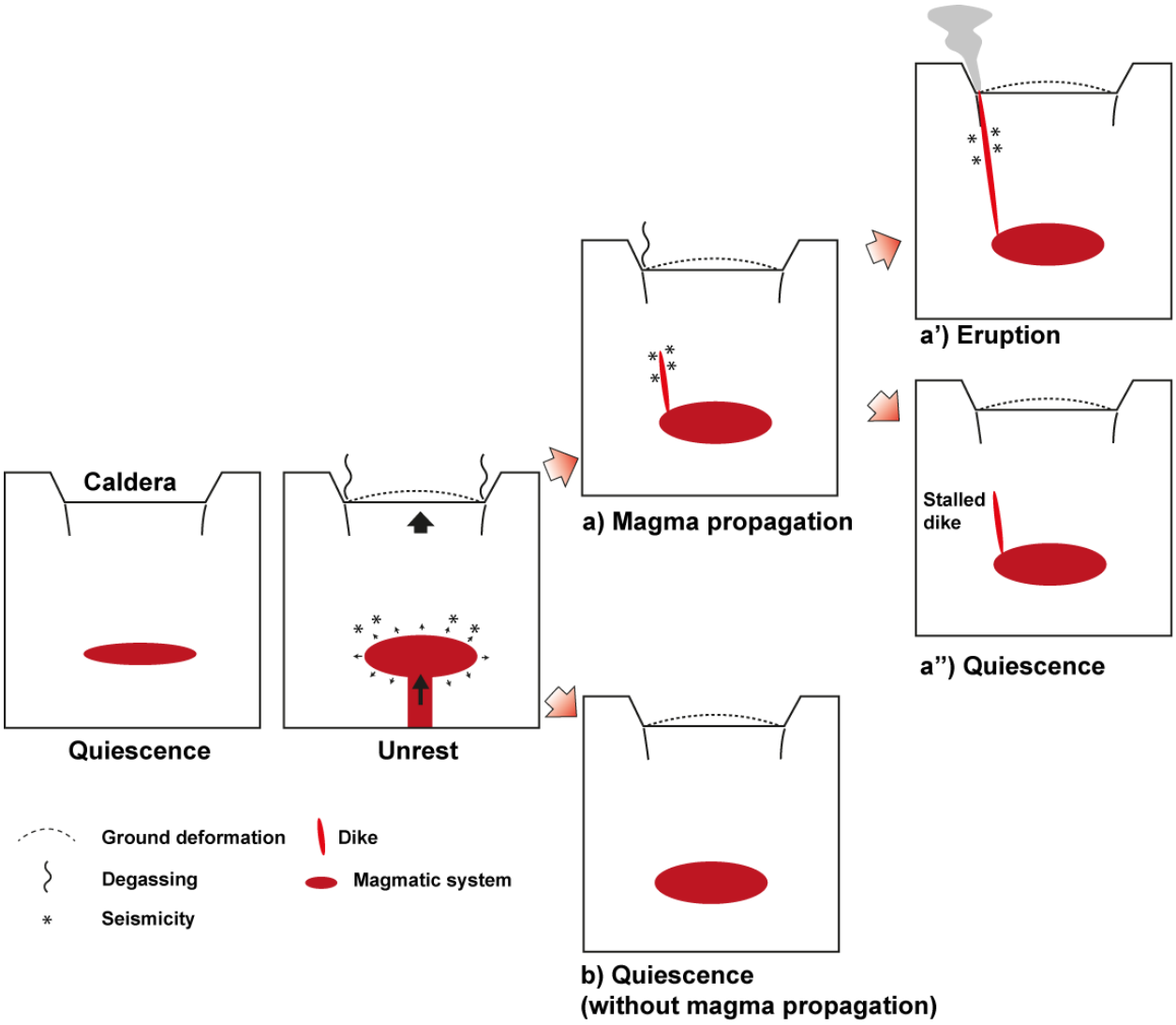

Figure 1. Evolution of caldera unrest. Supply of new magma to the magmatic system can trigger unrest. The unrest can end (a) with or (b) without magma propagation. When magma propagates, it can (a') reach the surface or (a'') stall.

Acocella et al., (2015) proposed an interpretation of unrest behaviours based on the composition and the state of the conduit (open, semi-plugged, plugged) (Figure 2). In open systems, magma and gas can rise and erupt frequently; semi-plugged systems degas, without any open conduit; closed systems do not degas and erupt more seldom. Felsic plugged calderas erupt infrequently and usually have short pre-eruptive unrest; felsic semi-plugged calderas erupt infrequently, but are restless for decades; mafic calderas, especially those with open system, have repeated unrest episodes, which can often end with moderate eruptions (Dvorak & Dzurisin, 1997; Acocella et al., 2015; Robertson & Kilburn, 2016). The pre-eruptive unrest usually lasts less than 1 year, especially in open or semi-plugged

calderas and in calderas with mafic or intermediate composition fed by mafic magmas, while unrest longer than 1 year is usually non-eruptive, suggesting that magma may withstand only a limited period of ‘‘eruptibility”, before becoming stored in the upper crust (Sandri et al., 2017).

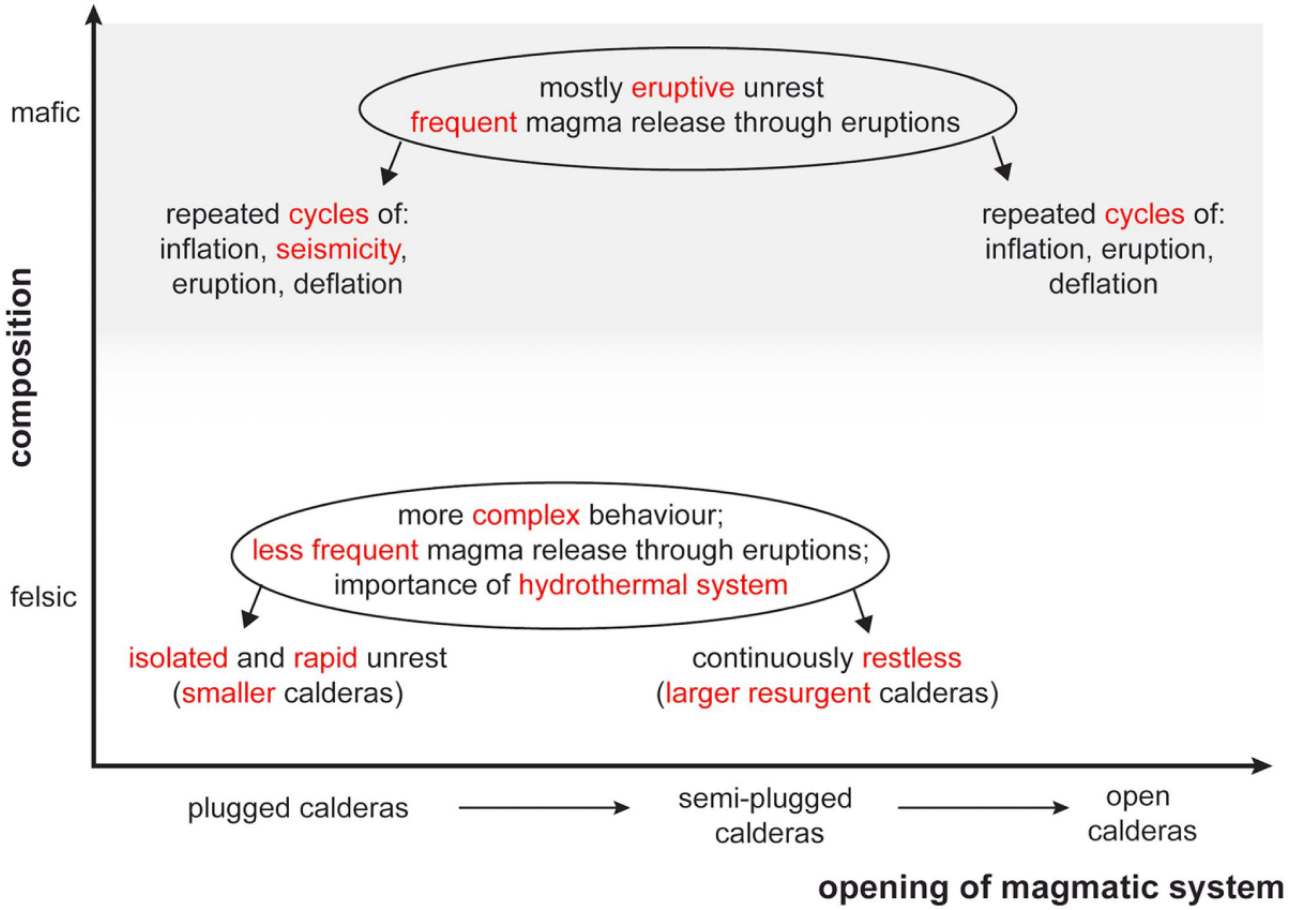

Figure 2. Schematic summary of the types of caldera unrest as a function of the composition and the state of opening of the system (from Acocella et al., 2015).

Mafic calderas seem to provide better conditions to study unrest for the following reasons:

1) They usually experience repeated unrest episodes (Dvorak & Dzurisin, 1997; Nooner & Chadwick, 2016).
2) Unrest episodes often show regular patterns, characterized by multiple cycles of uplift accompanied by seismicity and co-eruptive deflation (Dvorak & Dzurisin, 1997; Nooner & Chadwick, 2016).

In the western Galápagos (Ecuador) there are six active mafic calderas, sharing similar characteristics (see subsection 1.1), which have experienced repeated eruptive and non-eruptive unrest episodes in the last decades (Amelung et al., 2000; Chadwick et al., 2011; Bagnardi et al., 2013; Stock et al., 2018). Here, ground deformation is a constant feature of the unrest episodes. As the other parameters that characterize unrest, such as seismicity and degassing, are not monitored (or are poorly monitored)

at these calderas, most of the previous studies of unrest at the western Galápagos calderas have been focusing on ground deformation using the Synthetic Aperture Radar Interferometry (InSAR) technique (Amelung et al., 2000; Chadwick et al., 2011; Jónsson, 2009; Bagnardi & Amelung, 2012; Xu et al., 2016; Stock et al., 2018). Therefore, these unrest episodes have all been studied using a similar approach and similar methods, providing the opportunity to directly compare their results. In addition, these calderas allow the study of the relationships between ground deformation and eruptive unrest. For these reasons, the western Galápagos provide favourable conditions to investigate unrest at mafic calderas.

1.1- Geological background of the western Galápagos

The Galápagos Archipelago, in the eastern Pacific Ocean, is a widespread (> 40.000 km^2) system of volcanic islands and seamounts and one of the most active magmatic provinces on Earth. These are the surface expression of a hot spot, whose upwelling region is now centred below the western Galápagos Islands, immediately to the southwest of Fernandina Island (Gibson & Geist, 2010; Poland; 2014; Villagomez et al., 2014). The Galápagos Archipelago lies mainly upon a broad volcanic platform overlying young (< 10 Ma) oceanic lithosphere, on the eastward drifting Nazca plate (Figure 3; Feighner & Richards, 1994; Rychert et al., 2014). The Galápagos are placed in a complex geodynamic setting. In fact, 100-300 km to the north of the Archipelago lies the Galápagos Spreading Centre (GSC), an east-west striking intermediate-rate spreading centre that is migrating to the north of the plume, and which separates the Cocos (to the north) and Nazca (to the south) plates. The GSC is offset, at ~90°50' W, by the north-south striking Galápagos Transform Fault (GTF) (Figure 3; Wilson & Hey, 1995; Harpp & Geist, 2002, 2018; Werner et al., 2003; Mittelstaedt et al., 2012; Mittal & Richards, 2017). The perturbation to the lithospheric stress field caused by the GTF probably promoted the formation of volcanic lineaments and faults, such as the northwest-southeast Wolf-Darwin Lineament, which separate the eastern from the western Galápagos (Harpp & Geist, 2002; Mittelstaedt et al., 2012). These constitute two distinct volcanological, petrological, geochemical, and structural provinces (White et al., 1993; Feighner & Richards, 1994; Harpp & Geist, 2018).

Most of the recent volcanic activity focuses on the younger western Galápagos province (Figure 4a), constisting of the volcanoes of Fernandina, Cerro Azul, Sierra Negra, Alcedo, Darwin, Wolf and Ecuador (the coalescence of the latter six makes up Isabela island), placed near the upwelling region of the hot spot (Villagomez et al., 2014). Contrary to the older, eastern Galápagos, the western Galápagos consist of large, flexurally-supported shield volcanoes with summit calderas (Feighner & Richards, 1994; Harpp & Geist, 2018). These fall into two morphometric groups, called Type-1 and Type-2 (Mouginis-Mark et al., 1996; Munro & Rowland, 1996; Naumann & Geist, 2000). Type-1

volcanoes (Darwin, Alcedo and Sierra Negra) have gently dipping flanks over the entire height range and a relatively shallow caldera, while Type-2 volcanoes (Fernandina, Cerro Azul and Wolf) have gently dipping lower flanks, steep upper flanks and deeper calderas.

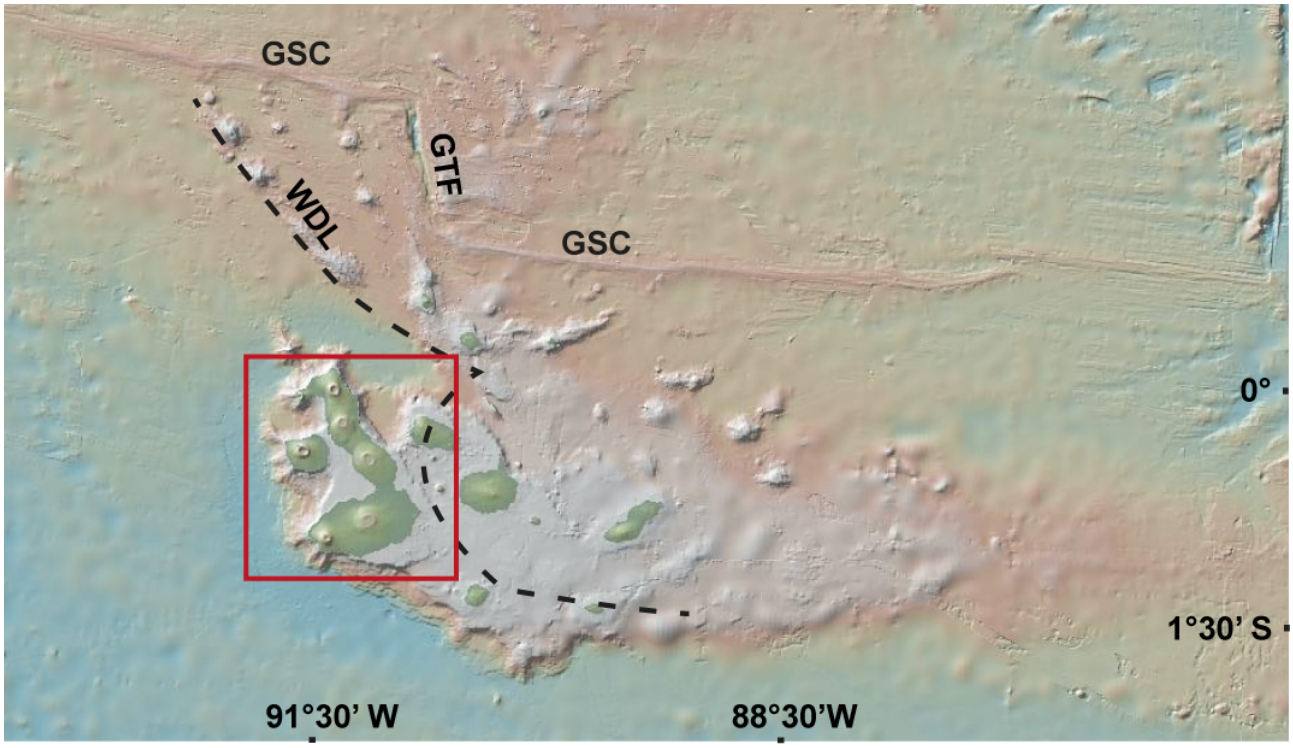

Figure 3. a) Galápagos Archipelago. GSC = Galápagos Spreading Center; GTF = Galápagos Transform Fault; WDL = Wolf-Darwin lineament. The dotted lines separate the region where the lithosphere has an effective elastic thickness of 12 km and volcanoes are flexurally supported, from the region to the east with a lower (<6 km) effective elastic thickness (Feighner and Richards, 1994). The red rectangle outlines the extent of Figure 4a, with the western Galápagos magmatic province.

The western Galápagos calderas are mafic in composition and their magmatic products are tholeiitic basalts, even if Cerro Azul has erupted also alkali basalts and Alcedo a rhyolite (Geist et al., 1994; Naumann & Geist, 1999; Geist et al., 2014). With the possible exception of Cerro Azul, all the western Galápagos have a shallow (1-3 km), flat topped, magmatic system, which overlies a deeper plumbing system, consisting of a mafic cumulate mush, with subordinate liquid magma, probably formed by the interconnection and coalescence of multiple intrusive bodies between the Moho and the shallow portion (Geist et al., 2014).

Geist et al., (2014) and Harpp & Geist, (2018) proposed a three-stage evolutionary model for the western Galápagos volcanoes, mainly based on petrological data. These three-stages are: 1) the juvenile transient phase (Cerro Azul), with a relatively deep, small and hot magmatic system; 2) the mature steady-state phase (e.g. Fernandina, Wolf and Darwin) with a well-developed,

termochemically-buffered plumbing system, composed of a thick mush zone; 3) the dying cooling phase (e.g. Alcedo), with a cooler plumbing system.

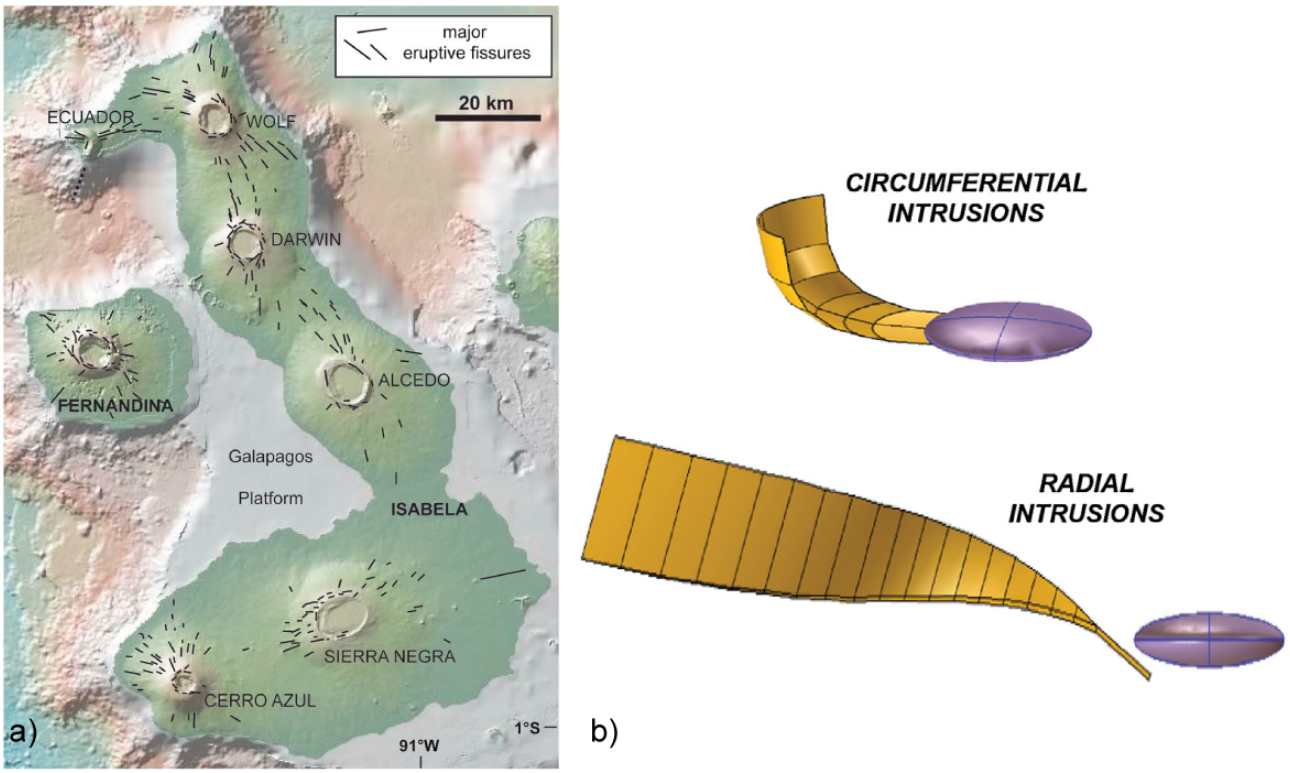

Figure 4. a) Main eruptive fissures at the western Galápagos calderas. These fissures are both circumferential and radial (from Acocella et al., 2015). b) Representation of the circumferential and radial intrusions. In purple is the shallow magmatic system, while in yellow are the intrusions feeding the eruptive fissures (from Bagnardi et al., 2013).

The Western Galápagos volcanoes do not have well-developed rift zones, as is the case at some other volcanic islands fed by a hot spot (e.g., Hawaii; Poland, 2014). On the contrary, the western Galápagos volcanoes show a characteristic pattern of circumferential eruptive fissures just outside the caldera rim and radial eruptive fissures along the flanks of the volcano (Figure 4a; Chadwick & Howard, 1991). Bagnardi et al., (2013) related these fissures to complex shallow magma transfer mechanisms (Figure 4b). Circumferential dikes, which feed circumferential fissures, initiate as sill-like intrusions from the shallow magmatic system that become successively steeper by transitioning into circumferential dikes, parallel to the caldera rim. Radial dikes also initiate as sill-like intrusions from the shallow magmatic system but they instead turn and twist around a radial horizontal axis during their lateral propagation, eventually feeding radial fissures (Bagnardi et al., 2013). The stress field allowing the formation of both types of fissures seems to be mainly controlled by the gravitational unloading after caldera collapse and the stresses from previous intrusions, with further

contribution from the load of the edifice and the pressurization of a flat-topped magma chamber (Bagnardi et al, 2013; Corbi et al., 2015; Chadwick & Dieterich, 1995).

In the last 30 years, the calderas of Fernandina, Cerro Azul, Sierra Negra, Alcedo, Darwin and Wolf experienced repeated unrest events. Table 1 and 2 summarize the available information associated with the intruded and erupted volumes and the rates of magma supply related to these unrest episodes. Some of these unrest episodes culminated in eruptions, as occurred at Fernandina in 1995, 2005, 2009, 2017, 2018; at Cerro Azul in 1998 and 2008; at Sierra Negra in 2005 and 2018 and at Wolf in 2015 (Jónsson et al., 1999; Amelung et al., 2000; Geist et al., 2008; Chadwick et al., 2011; Bagnardi and Amelung, 2012; Stock et al., 2018; Global Volcanism Program, 2008; 2017, 2018). Other unrest episodes were non-eruptive, as those occurred at Fernandina from August 2005 to 2007; at Sierra Niegra from 1992 to 2003; at Alcedo from 1992 to 2011; at Darwin from 1992 to 2000 and at Wolf from 1992 to 2008 (Amelung et al., 2000; Chadwick et al., 2006; Bagnardi & Amelung, 2012; Stock et al., 2018). These non-eruptive unrest episodes are usually characterized by a constant uplift of the caldera floor and often last for more than 2 years, as at Sierra Negra, Alcedo, Darwin and Wolf (Amelung et al., 2000; Chadwick et al., 2006; Stock et al., 2018). In particular, Sierra Negra experienced the most dramatic uplift, of about 5 m between 1992 and 2005 and 2 meters after the 2005 eruption; the uplift was accommodated, in part, inelastically by repeated trapdoor-faulting events (Amelung et al., 2000; Jónsson et al., 2005; Jónsson, 2009; Chadwick et al., 2006). Finally, unrest episodes sometimes are associated with subsidence, as at Alcedo from 1997 to 2001 and at Sierra Negra from 2000 to 2003 (Chadwick et al., 2006; Hooper et al., 2007).

1.2 Method

1.2.1 InSAR theory

Synthethic Aperture Radar (SAR) technique allows creating high resolution radar images from data acquired by side-looking instruments carried by satellites (Massonnet et al., 1998; Burgmann et al., 2000; Dzurisn, 2007; Pinel et al., 2014 and references therein). Each pixel of a SAR image is characterized by two values: the amplitude and the phase. The amplitude can be interpret in terms of the scattering properties of the ground, while the phase is essentially random and, therefore, is not informative (Massonnet et al., 1998; Hooper et al., 2012 and references therein). However, the phase differences between two images, covering almost the same area, can be interpret in terms of the change in range from the satellite to the ground if the scattering characteristics of the ground do not change significantly (Dzurisin, 2007; Lu & Dzurisin, 2014). This is the principle on which SAR interferometry (InSAR) is based. Thus, the phase of the resultant "interferogram" is equal to the phase

differences between the two SAR images and the interferometric phase of each pixel can be described as (Hooper et al., 2012; Pinel et al., 2014):

$$\phi = W\{\phi_{def} + \phi_{topo} + \phi_{atm} + \phi_{or} + \phi_N\} \quad (1)$$

where ϕ_{def} is the contribution due to the displacement from the pixel in the satellite line-of-sight (LOS) direction; ϕ_{topo} is the contribution due to deviations of the real Earth surface from the reference surface due to topography; ϕ_{atm} is the contribution from the difference in the phase delay during propagation of the signal through the atmosphere between acquisitions; ϕ_{or} is the residual phase due to orbit errors; $\phi_N$is the phase noise due to both variability in scattering and thermal noise. W{·} is an operator that drops whole phase cycles (known as "wrapping"), as only the fractional part of the phase can actually be measured (Pinel et al., 2014 and references therein).

If an interferogram is generated from two images acquired at different times, LOS displacements (ϕ_{def}) can be obtained by minimizing as much as possible the contributions to the interferometric phase due to the other terms reported in equation 1. It is important to note that InSAR does not provide an absolute value for displacements, as the phase only records the fractional part of each phase cycle. However, the relative LOS displacement between any two pixels in an interferogram can be estimated by integrating the number of fringes between them, through a process known as phase unwrapping (Hooper et al., 2012; Pinel et al., 2014 and references therein). Therefore, phase unwrapping is the procedure for solving the 2π ambiguity inherent in radar interferograms to calculate the correct integer number of phase cycles to be added to each phase measurement (Dzurisin, 2007). Unwrapping errors cause therefore an incorrect estimation of the LOS displacements (Massonnet et al., 1998).

1.2.2 InSAR method

In this thesis interferograms were formed using the InSAR Scientific Computing Environment (ISCE) software (Rosen et al., 2012). Topographic contributions to the interferometric phase were removed using a 30 m-resolution DEM from the NASA Shuttle Radar Topography Mission (Farr et al., 2007). Interferograms were then combined to study the temporal evolution of surface displacements through a multi-temporal (MT) approach. The MT approach helps minimizing atmospheric, orbital, DEM, and unwrapping errors (Lu & Dzurisin, 2014; Hooper et al., 2012). Among the different MT approaches, I applied the Small Baseline (SB) method using the StaMPS software (Hooper, 2008, Hooper et al., 2012).

1.2.3 Geodetic modelling

To constrain the sources of deformation, InSAR LOS displacement measurements were inverted for possible magmatic sources. Deformation source parameters and uncertainties were estimated using the Bayesian approach implemented in the Geodetic Bayesian Inversion Software (GBIS; Bagnardi & Hooper, 2018). The inversion algorithm uses a Markov-chain Monte Carlo method, incorporating the Metropolis-Hastings algorithm, to find the posterior probability density functions (PDFs) of model parameters.

Through the Bayesian approach, I sampled the joint posterior PDF for the model parameters, taking into account uncertainties in the data, which were directly quantified using experimental semivariograms calculated from the data, and approximated by unbounded exponential one-dimensional functions with a nugget (Bagnardi & Hooper, 2018). To reduce the computational burden, InSAR data were subsampled using an adaptive quadtree method (Decriem et al., 2010**;** Bagnardi & Hooper, 2018).

Deformation source-types used in this thesis were the point source (Mogi, 1958), the finite spherical cavity (McTigue, 1987), the prolate ellipsoid (Yang et al., 1988), the rectangular dislocation with uniform opening (as dikes and sills; Okada, 1985), the rectangular dislocation (RD) and the compound dislocation models (CDM) (Nikkhoo et al. 2017).

As GBIS inverts the unwrapped data, it is essential that the unwrapped phase is not affected by unwrapping errors. The occurrence of the latter prevents the possibility to use GBIS. To overcome any unwrapping errors in Chapter 3 I have presented a new method to invert the wrapped data directly.

1.3- Aims and organization of the Thesis

The aim of this Ph.D. Thesis, written in the form of scientific articles, is to increase the knowledge on the unrest episodes at the western Galápagos calderas and to extend the new results to other mafic calderas sharing similar characteristics. To pursue these aims, first, I analysed previously non-studied eruptive and non-eruptive unrest episodes at two of the less known volcanoes among those of the western Galápagos: Alcedo and Cerro Azul. Specifically, the first article (Chapter 2), published in Journal of Geophysical Research-Solid Earth, investigates the non-eruptive unrest episodes occurred at Alcedo from 2007 to 2011. The second article (Chapter 3), submitted to Journal of Geophysical Research-Solid Earth, analyses the eruptive unrest occurred at Cerro Azul in 2008. Some of the InSAR data of Cerro Azul are affected by unwrapping errors, due to erroneous estimates of the phase integer ambiguities during the so-called unwrapping process. These errors bias InSAR data inversion results. To overcome the unwrapping errors and to properly invert InSAR data, we proposed a new

method to invert the wrapped interferometric phase directly by estimating the integer phase ambiguities simultaneously with the geophysical parameters (see Chapter 3, Section 3.1).

Finally, the third article (Chapter 4; manuscript in preparation), reviews all the geodetically monitored unrest episodes at the western Galápagos calderas, mainly considering the estimated injected volumes of magma and the related intrusive rates. These data are then compared to those from other calderas sharing similar characteristics, to highlight any possible relationship between the outcome of unrest and the rates at which magma is injected into the shallow magmatic system of mafic calderas.

	V (km^3)	Q (km^3/year)	t (year)	V(er)	
Fernandina					
1995 eruption (time span of the interferogram from 1992 to 1997) (Jónsson et al., 1999; Bagnardi et al., 2013)					
Sill	3.47×10^{-3}				Eruption
Radial dike	6.09×10^{-3}				
16 January 2001-13 June 2002 (Geist et al., 2006; Chadwick et al., 2011)					
Shallow system[a]	1.2×10^{-3}	8.5×10^{-4}	1.41		Uplift
From January 2003 to 26 April 2005 (Chadwick et al., 2011)					
Shallow system	$7.6\pm0.4\times10^{-4}$	$3.8\pm0.2\times10^{-4}$	2.02		Pre-eruptive uplift
Deeper system	$5.14\pm0.69\times10^{-3}$	$2.5\pm0.3\times10^{-3}$	2.02		Pre-eruptive uplift
Eruption 13-29 May 2005 (time span of the interferogram 7 May-16 July 2005)					
Circumferential dikes	9.77×10^{-3}				
Shallow system	8.3×10^{-4}				
total				14×10^{-3}	Eruprion
Deeper system[b]	-6.4×10^{-3}				
Post-eruptive (August 2005 - November 2006) (Chadwick et al., 2011)					
Shallow system	$1.36\pm0.11\times10^{-3}$	$1.1\pm0.1\times10^{-3}$	1.25		Post-eruptive uplift
Deeper system	$2.92\pm0.38\times10^{-3}$	$2.3\pm0.3\times10^{-3}$			
27 January 2007 - 21 July 2007 (Bagnardi & Amelung, 2012)					
Shallow system	1.1×10^{-3}	2.3×10^{-3}	0.48		Uplift
27 August - 18 September 2007 (most by 30 August) (deep lateral propagation of magma) (Bagnardi & Amelung , 2012)					
Sill	1.9×10^{-2}				Deep sill propagation
28 September 2007 - 26 April 2008 (Bagnardi et al., 2013)					
Deeper system	1.54×10^{-2}	2.69×10^{-2}	0.57		Uplift
28 September 2007 - 9 April 2009 (Bagnardi 2014)					
Shallow system	4×10^{-3}	2.6×10^{-3}	1.53		Uplift
10 Apr 2009 (13 h before the eruption)					
Sill[c]	7.29×10^{-3}				
Deeper system	-4.55×10^{-3}				
Eruption (10-28 April 2009) (interferogram show that all the deformation occurred before May 5th) (Bagnardi et al., 2013).					
Radial dike	9.73×10^{-3}				
Sill[d]	7.29×10^{-3}				
Total	1.70×10^{-2}				Eruption
Shallow system	-4.8×10^{-3}				
Deeper system	$>-3\times10^{-2}$				

Table 1. Available information on unrest episodes occurred at Fernandina since 1992. V is the intruded volume estimated from the inversion of geodetic data. Q is the rate at which magma is supplied. V(er) is the erupted volume. t is the duration of the event. [a] Data obtained from the inversion

of GPS data only. [b] *The volume lost by the deeper system may have been underestimated (see Chadwick eta l., 2011 for further details).* [c] *This sill is the incipient propagation of the radial dike , which initiates as a sill-like intrusion.* [d] *Same sill of 10 April 2009*

	V (km^3)	Q (km^3/year)	t (year)	
Sierra Negra				
	26 September 1998 to 20 March 1999 (Yun et al., 2006)			
Shallow system	6.7×10^{-3}	1.40×10^{-2}	0.48	Uplift
	5 January 2001 to 3 June 2002 (Geist et al., 2006)			
Shallow system	-4.10×10^{-3}	-2.91×10^{-3}	1.41	Subsidence
	1 April 2003 to 15 April 2005 (Chadwick et al., 2006)			
Shallow system	2.9×10^{-2}	1.40×10^{-2}	2.04	Uplift
	12 February 2004 - 27 January 2005 (Chadwick et al., 2006)			
Shallow system	1.6×10^{-2}	1.70×10^{-2}	0.96	Uplift
	16 April 2005 - 21 October 2005 (Chadwick et al., 2006)			
Shallow system	3.3×10^{-2}	6.40×10^{-2}	0.52	Pre-eruptive uplift
	22 October - 30 October 2005 (Geist et al., 2008)			
	1.5×10^{-1} [(a)]			Eruption
	November 2005 to January 2011 (Bagnardi, 2014)			
Shallow system	6.70×10^{-2}	1.28×10^{-2}	5.24	Uplift
Wolf				
	15 June 1992 – 27 December 2008[b] (Bagnardi, 2014)			
Shallow system	5×10^{-3}	3×10^{-4}	16.55	Uplift
	03 January 2004 - 27 December 2008 (Stock et al., 2018)			
Shallow system	1.5×10^{-3}	3×10^{-4}	4.99	Uplift
	25 May to 11 July 11 2015 (Bernard et al., 2019; Stock et al., 2018; Xu et al., 2016)			
	$8.7 \pm 2.7 \times 10^{-2}$ [(c)]			Eruption
Deeper system	$-5.3 \pm 1.1 \times 10^{-2}$			Eruption
Shallow system	-2.8×10^{-3}			Eruption
Darwin				
	15 June 1992 - November 2000 (Bagnardi, 2014)			
Magmatic system	1×10^{-2}	1.2×10^{-3}	8.39	Uplift
Alcedo				
	October 1997 – January 2001 (Hooper et al., 2007)			
Shallow system	$-1.28 \pm 0.03 \times 10^{-3}$	-3.93×10^{-4}	3.25	Subsidence
Cerro Azul				
	8 March 2017-20 March 2017 (Bagnardi & Hooper, 2018)			
Sill	$3 \pm 1 \times 10^{-2}$	9.1×10^{-1}	0.033	Deep lateral propagation

Table 2. Available information on the unrest episodes occurred at the calderas on Isabela Island in since 1992. V is the intruded volume estimated from the inversion of geodetic data. Q is the rate at which magma is supplied. t is duration of the event. [a] *Erupted volume. This is similar to those estimated from the inversion of the subsidence data associated with the eruption.* [b] *Deformation from 2000 to 2008, and especially from 2004 to 2008, is temporally better constrained.* [c] *is the erupted volume. During the first eruptive phase $4.76 \pm 1.88 \times 10^{-2}$ km^3 (DRE) of magma were erupted, while during the second eruptive phase $3.95 \pm 1.49 \times 10^{-2}$ km^3 (DRE) of magma were erupted (Bernard et al., 2019).*

Chapter 2

Article published on *Journal of Geophysical Research: Solid Earth*,
https://doi.org/10.1029/2018JB017103

Non-eruptive unrest at the caldera of Alcedo Volcano (Galápagos Islands) revealed by InSAR data and geodetic modelling.

Federico Galetto[1], Marco Bagnardi[2,3], Valerio Acocella[1] and Andrew Hooper[2]

[1] Università degli Studi di Roma Tre, Dipartimento di Scienze, Rome, Italy

[2] COMET, School of Earth and Environment, University of Leeds, Leeds, UK

[3] Now at Jet Propulsion Laboratory, California Institute of Technology, Pasadena, CA, USA

Corresponding author: Federico Galetto (federico.galetto@uniroma3.it).

Key Points

2007-2011 non-eruptive unrest at Alcedo caused by shallow emplacement of new magma with limited lateral intrusion.

Uplift during unrest is similar in location and shape to the longer-term weak resurgence of the caldera.

This unrest provides the rare opportunity to document the incremental growth of a basaltic resurgent caldera.

Abstract

Understanding volcanic unrest is crucial to forecasting eruptions. At active mafic calderas unrest culminates in eruption more frequently than at felsic calderas. However, the mafic caldera of Alcedo Volcano (Ecuador) has experienced repeated episodes of unrest without erupting, since at least 1992, when geodetic monitoring began. Here, we investigate the unrest that occurred between 2007 and 2011 using interferometric synthetic aperture radar (InSAR) data and geodetic modelling. We observe

an initial asymmetric uplift of the southern caldera floor (~30 cm of vertical motion) from 2007 to 2009, followed by subsidence of the uplifted area and contemporary uplift of the north-western caldera rim between January and June 2010. Finally, from June 2010 through March 2011, caldera uplift resumed. The first uplift episode is best explained by inflation of a sill and the activation of an inner ring fault. Successive caldera subsidence and rim uplift are compatible with the withdrawal of magma from the previously inflated sill and its north-western migration. The resumption of uplift is consistent with the re-pressurization of the sill. This evolution suggests episodic magma emplacement in a shallow reservoir beneath the caldera, with aborted lateral magma migration, probably due to the discontinuous supply from depth. This short-term deformation pattern matches well geological observations showing a longer-term (hundreds of years at least) asymmetric uplift of the caldera floor, culminating in a weak resurgence of ~30 m. We propose that the monitored episodes of uplift represent short-term stages of the rarely observed incremental growth of a resurgent basaltic caldera.

1 - Introduction

Calderas are broad sub-circular depressions resulting from the partial or complete emptying of a subsurface magma reservoir as consequence of an eruption or lateral migration of magma, as observed in 1968 at Fernandina (Galápagos, Ecuador) and in 2014-2015 at Bardarbunga Volcano, Iceland (Gudmundsson et al., 2016; Howard et al., 2018). Most active calderas experience periods of unrest over decadal time-scales (Newhall and Dzurisin, 1988; Acocella et al., 2015), where unrest is defined as a deviation from baseline monitoring parameters, such as changes in seismicity, degassing and ground deformation. While not all episodes of unrest culminate in an eruption, most eruptions, especially in caldera systems, are preceded by a period of unrest. Therefore, understanding the nature of an episode of volcanic unrest is fundamental when assessing volcanic hazard (Biggs et al., 2014; Acocella et al., 2015; Biggs & Pritchard, 2017). This effort should be pursued regardless of whether the unrest results in eruption or not. In fact, it is equally important to understand both processes leading to eruptions and those that do not; the impact in forecasting eruptions is equally significant in both cases.

Previous studies have shown that unrest at mafic calderas is generally more regular, or "predictable", than at felsic calderas (Dvorak & Dzurisin, 1997; Acocella et al., 2015). At mafic calderas, pre-eruptive inflation and increase in seismicity are commonly followed by an eruption and co-eruptive deflation (Dvorak & Dzurisin, 1997; Acocella et al., 2015), over multiple self-similar cycles. On the other hand, felsic calderas often show subsequent periods of inflation and increase in seismicity that do not culminate into eruptions (Acocella et al., 2015). This basic distinction, however, includes many

exceptions, such as mafic calderas that experience multiple episodes of non-eruptive unrest, a behaviour more characteristic of felsic systems. Among these is the mafic caldera of Alcedo Volcano (Isabela Island, Galápagos, Ecuador), where previous geophysical measurements have identified periods of unrest without eruptions. Our understanding of these non-eruptive unrest episodes remains limited (Amelung et al., 2000; Hooper et al., 2007), despite being of fundamental importance for the definition of the mechanisms hindering the rise of magma to the surface and for our capability of forecasting eruptions.

In this study we use interferometric synthetic aperture radar (InSAR) data acquired at Alcedo between 2006 and 2011, which record surface displacements during multiple deformation events that did not end with an eruption and that have similar characteristics to episodes of non-eruptive unrest that occurred between 1992 and 2001 (Amelung et al., 2000; Hooper et al., 2007). Through modelling the geodetic data, we place constraints on the sources responsible for these episodes of unrest. In addition, we link these shorter-term episodes to the longer-term evolution of the caldera, where geological and geomorphological observations suggest the development of a weak resurgence.

2 - Geological Background: Galápagos and Alcedo

Alcedo Volcano lies in the Galápagos Archipelago, a widespread (> 40,000 km^2) system of volcanic islands and seamounts in the eastern Pacific Ocean, and one of the most active magmatic provinces. Galápagos volcanism is related to a hot-spot, whose head is centred below the western islands of the archipelago, immediately to the SW of Fernandina Island (Naumann & Geist, 2000; Hooft et al., 2003; Gibson & Geist, 2010; Villagómez et al., 2014). The Galápagos islands and seamounts have grown above a broad and thick platform, which overlays young (<10 Ma) oceanic lithosphere (Feighner & Richards, 1994; Rychert et al., 2014). The Galápagos Archipelago is located on the eastward-moving Nazca plate, ~170 km south of the Galápagos Spreading Centre (GSC), an E-W striking intermediate-rate spreading centre, which separates the Cocos (to the north) and Nazca (to the south) plates (Figure 1a; Canales et al., 1997; 2002; Werner et al., 2003; Mittelstaedt et al., 2012; Harpp & Geist, 2018). The NW-SE trending Darwin-Wolf lineament (DWL) separates the Eastern from the Western Galápagos, which are two distinct volcanological, petrological, geochemical and structural provinces (Figure 1a; White et al., 1993; Feighner & Richards, 1994; Harpp & Geist, 2018). The younger Western Galápagos are characterized by large and flexurally-supported shield volcanoes with summit calderas, while the older Eastern Galápagos volcanoes are smaller and do not have well developed calderas (Feighner & Richards, 1994; Harpp & Geist, 2018).

Most of the recent volcanic activity in the Galápagos has focussed on the seven shield volcanoes forming the western islands of Isabela and Fernandina, near the upwelling region of the hot-spot (Gibson & Geist, 2010; Villagómez et al., 2014). These volcanoes are Fernandina, Ecuador, Wolf, Darwin, Alcedo, Sierra Negra and Cerro Azul (the coalescence of the last six volcanoes makes up Isabela Island) (Figure 1b). Western Galápagos volcanoes have gently-sloping outer flanks, steep upper flanks, and well-established summit calderas (Mouginis-Mark et al, 1996; Munro & Rowland, 1996; Naumann & Geist, 2000). With the exception of Cerro Azul, all these volcanoes have shown evidence for shallow (1-3 km beneath the caldera floor) flat-topped magma reservoirs (Geist et al., 2014 and references therein).

The Western Galápagos volcanoes have been classified in three evolutionary stages (Geist et al., 2014; Harpp & Geist, 2018): 1) juvenile transient phase (e.g., Cerro Azul), with a deep, hot, and small magmatic system; 2) mature steady state phase (e.g., Fernandina, Darwin, and Wolf), characterized by high magma supply rates and a well-developed, thermochemically buffered, thick mush zones with a shallow, flat top; 3) dying cooling phase (e.g., Alcedo), with a cooler, less fed, and more evolved magmatic system. The dying phase of Alcedo is supported by a decrease in eruption rate since ~120 ka, from 1.8×10^6 to 0.1×10^6 m^3/yr (Geist et al., 1994). In addition, even if Alcedo mainly erupts transitional basalts, at ~120 ka it erupted rhyolitic pumice and lava, which are the most fractionated and evolved products in the Western Galápagos (Geist et al., 1995).

The volcanic edifice of Alcedo reaches a maximum elevation of 1130 m above sea level, with gently dipping lower flanks, steeper upper flanks (33°) and a large (41.6 km^2) but shallow caldera (270 m deep). This morphology has been related to a decrease in magmatic activity (Nordlie, 1973; Geist et al., 1994; Murno & Rowland, 1996; Mouginis-Mark et al., 1996; Naumann & Geist, 2000). The caldera is elliptical in shape (7 x 6 km) and has its major axis oriented NW-SE (Murno & Rowland, 1996) (Figure 1c). Alcedo caldera shows a complex morphology, with three fault scarps delimiting the NW side and one scarp in the SSW part. The scarps to the NW have been interpreted as blocks of the caldera floor that have been broken and faulted during repeated cycles of caldera collapse and filling, with the centre of the collapse progressively migrating southward. This migration may reflect that of a shallow magma reservoir, which therefore would currently lie below the southern part of the caldera floor (Geist et al., 1994). The SSW intra-caldera ring fault system is responsible for the formation of the caldera moat and of the trapdoor uplift of the southern caldera floor (Figure 1c, d). Such an uplift, reaching ~30 m, indicates a weak resurgence of the caldera (Geist et al. 1994), a feature rarely observed at mafic calderas, but that it is also occurring at the nearby mafic caldera of Sierra Negra (Galetto et al., 2017). This ring fault has been interpreted as an older caldera fault reactivated with opposite motion during the uplift, or resurgence (Geist et al., 1994). This area is also

characterized by intense fumarolic activity, fed by a shallow geothermal system located below the SW sector of the caldera (Goff et al., 2000). In this sector two phreatic explosions occurred between 1993 and 1994 (Green, 1994).

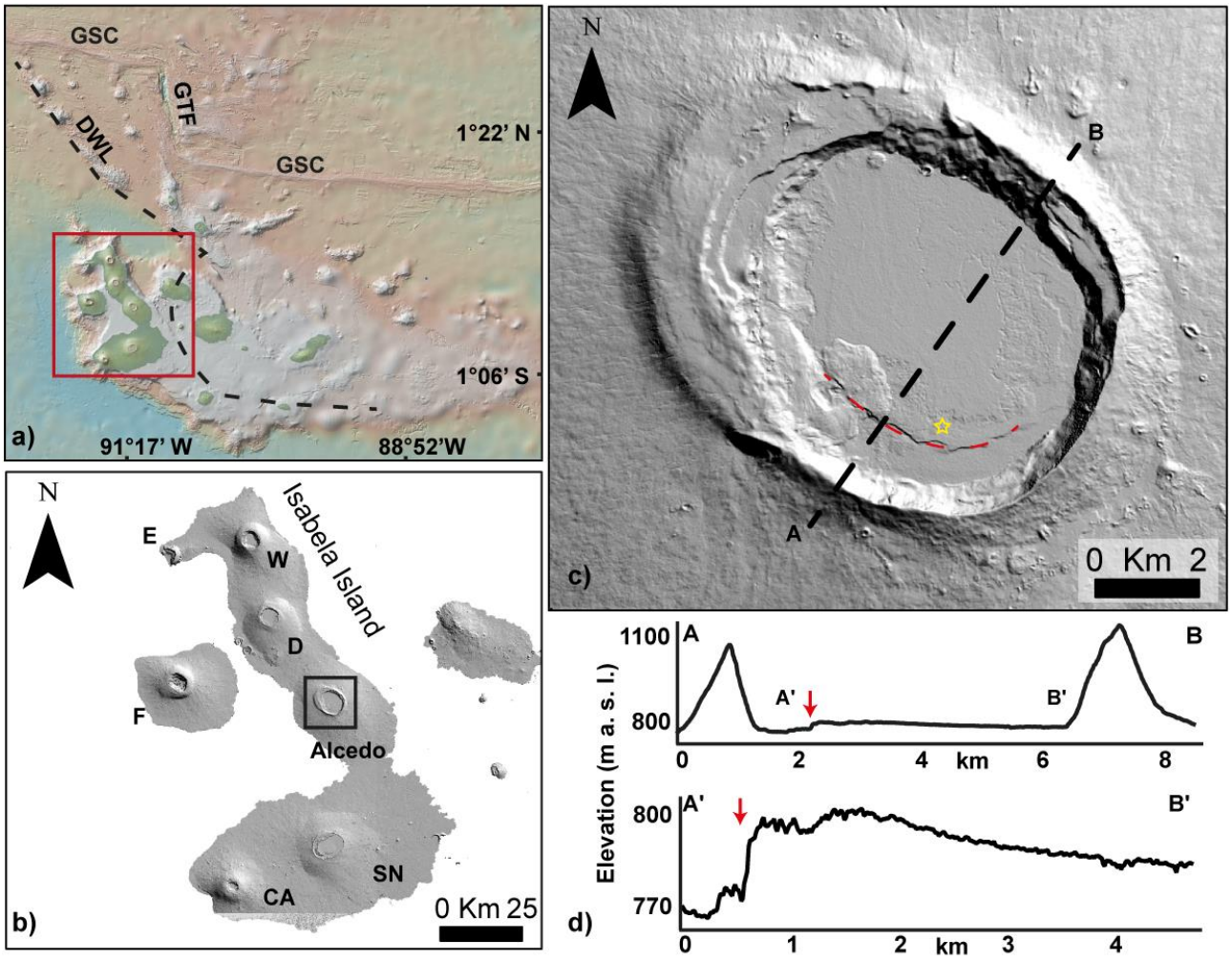

Figure 1. *(a) Topography and bathymetry of the Galápagos Archipelago. GSC: Galápagos Spreading Centre; GTF: Galápagos Transform Fault; the dashed line marks the Darwin-Wolf lineament (DWL) separating Western and Eastern Galápagos, as traced by Feighner & Richards (1994) (digital elevation model from GeoMappApp). The red square outlines the extent of panel b. (b) Shaded relief map (from WorldDEM data) of Fernandina (F) and Isabela Islands, on which lie the volcanoes Ecuador (E), Wolf (W), Darwin (D), Alcedo (the black square outlines the extent of panel (c)), Sierra Negra (SN) and Cerro Azul (CA). (c) Shaded relief map of Alcedo caldera. The yellow star indicates the location for which deformation time-series are shown in Figure 2c,d,j,k. The red dashed line marks the southern intra-caldera fault. The black dashed line A-B marks the location of the topographic profile in panel (d). (d) Topographic profile across the caldera floor (A-B profile) and the snapshot (A'-B' profile) that highlights the uplift, or weak resurgence, of the southern part.*

Elevation is with respect to sea level. The red arrows point the location of the southern intra-caldera fault.

The last recorded magmatic eruption occurred in the mid-1900s (Geist et al., 1994; 1995). In recent decades, geophysical measurements have shown that Alcedo experienced repeated episodes of non-eruptive unrest. Between 1992 and 1997, InSAR data showed a >90 cm net uplift, mainly focussed on the southern part of the caldera (Amelung et al., 2000; Hooper et al., 2007). Such data, however, offer poor temporal sampling and are not sufficient to determine if the uplift occurred episodically or at a stable rate throughout the six-year interval. Successively, between 1997 and 2001, uplift switched to subsidence (<11 cm), which has been interpreted as deflation of an ellipsoid-like body at ~2.2 km below sea level (Hooper et al., 2007). Conversely to Cerro Azul, Fernandina and Wolf (Amelung et al., 2000; Bagnardi et al., 2013; Xu et al. 2016; Stock et al., 2018), no deformation is recorded outside the caldera of Alcedo in the last 30 years.

3 – Data and Methods

To measure surface deformation at Alcedo, we processed 83 SAR images acquired by the European Space Agency's ENVISAT satellite (C-band, wavelength λ = 5.63 cm), 35 from an ascending track (T61) acquired between January 2006 and May 2010, and 48 from a descending track (T140) acquired between January 2003 to May 2010 (Figure 2). We also processed 38 SAR images from the Japanese Space Agency's ALOS-1 satellite (L-band, wavelength λ=23.6 cm), 20 from an ascending track (T133) acquired between January 2007 and March 2011 and 18 from a descending track (T474) acquired between January 2007 and July 2010 (Figure 2).

Interferograms were formed using the InSAR Scientific Computing Environment (ISCE) software (Rosen et al., 2012) and by applying conventional differential InSAR processing techniques. Topographic contributions to the interferometric phase were removed using a 30 m-resolution digital elevation model from the NASA Shuttle Radar Topography Mission (Farr et al., 2007). Interferograms were then combined to study the temporal evolution of surface displacements through a multi-temporal approach. We applied the Small Baseline (SB) method using the StaMPS software (Hooper, 2008, Hooper et al., 2012) and selected the processing parameters that maximized the signal-to-noise ratio. In Figure S1 we show the optimal networks of interferograms used for the SB analyses plotted as function of their perpendicular and temporal baselines. Finally, we used the method of Wright et al. (2004) to convert the ALOS-1 satellite line-of-sight (LOS) displacements

from two different viewing geometries into vertical and horizontal (E-W) components of displacement (Figure 3).

To constrain the sources of deformation, we inverted the ALOS-1 LOS displacement measurements. These datasets, compared to the ENVISAT data, offer much denser spatial data coverage, since L-band data can maintain better coherence in vegetated areas, such as the flanks of Alcedo. We estimated deformation source parameters and uncertainties using the Bayesian approach implemented in the Geodetic Bayesian Inversion Software (GBIS; Bagnardi & Hooper, 2018). The inversion algorithm uses a Markov-chain Monte Carlo method, incorporating the Metropolis-Hastings algorithm, to find the posterior probability density functions (PDFs) of model parameters. When available, the ascending and descending ALOS-1 LOS data were jointly inverted to better constrain the deformation source parameters.

Through the Bayesian approach we sampled the joint posterior PDF for the model parameters, taking into account uncertainties in the data, which were directly quantified using experimental semivariograms calculated from the data, and approximated by unbounded exponential one-dimensional functions with a nugget (Bagnardi & Hooper, 2018). Since no prior information on the source parameters was available, we set non-informative uniform prior PDFs bounded by geologically realistic values (Tables 1, 2 and 3). To reduce the computational burden, InSAR data were subsampled using an adaptive quadtree method (Decriem et al., 2010; Bagnardi & Hooper, 2018). In each inversion, we sampled the posterior PDFs through 1,000,000 iterations. Depth estimates are referred to as distance from the surface.

Together with deformation source-types already implemented in GBIS (e.g., point source [Mogi, 1958], finite spherical cavity [McTigue, 1987], prolate ellipsoid [Yang et al., 1988], rectangular dislocation with uniform opening [Okada, 1985]), we tested the rectangular dislocation (RD) and the compound dislocation models (CDM) of Nikkhoo et al. (2017). The RD is similar to the rectangular dislocation with uniform opening of Okada (1985) but has full rotational degrees of freedom. The CDM is able to simulate a sill/dike of finite thickness with full rotational degrees of freedom, and is free of artifact singularities (Nikkhoo et al., 2017). For all the models we assumed an isotropic elastic half-space with a Poisson's ratio $\nu = 0.25$. Under these assumptions, the estimated volume changes (ΔV) may underestimate the volume of magma that flowed in. In fact, these models do not consider the eventuality that the injection of new magma in a reservoir can be partly accommodated without surface deformation by the compression of the magmatic system (especially the gas and liquid phases) (Huppert & Woods, 2002; Voight et al., 2010), or by the viscous response of the host rock (Jellinek & DePaolo, 2003). Therefore, even though the effect of any viscous process may become significant

on time-scales that are longer than our data coverage (Jellinek & DePaolo, 2003; Degruyter & Huber, 2014), the volume changes presented in this study should be considered as minimum estimates.

4 - Results

4.1. – Surface deformation

From the analysis of InSAR time series calculated from ENVISAT and ALOS-1 data, we observe that the caldera of Alcedo subsided ~6 cm between the start of data coverage in 2003 and the end of 2006, with a minor, short-lived episode of uplift during the second half of 2004 (Figure 2c,d). From January 2007, we identify three main deformation events on which we focus our subsequent analyses.

4.1.1 First event

From January 2007 to the end of 2009, both the ALOS-1 and ENVISAT data show a temporally linear (Figure 2c,d) but spatially asymmetric (Figure 2a,b,e,f, Figure 3a,b) uplift of the southern part of the caldera. The maximum vertical displacement, ~30 cm, with a mean uplift rate of ~8.9 cm/yr, is recorded at the SW edge of the uplifted area (Figure 3a), where it is also bounded by the southern intra-caldera fault (Figure 1c).

4.1.2 Second event

From January to June 2010, ALOS-1 data show that the previously uplifted area subsided by a maximum of ~8 cm in a spatial asymmetric pattern peaking near the southern intra-caldera fault (Figure 2g, h; Figure 3c, d), as during the first event. During the same time interval, the western portion of the caldera rim, across the three faults scarps, uplifted by up to ~5 cm.

4.1.3 Third event

From July 2010 to March 2011, data coverage is limited to the ascending ALOS-1 track. These data show uplift of the previously subsiding area in the southern part of the caldera, corresponding to the uplifted area during the first event (Figure 2i and 2j). The maximum LOS displacement is ~10 cm, corresponding to a displacement rate of ~13 cm/yr, which is ~4cm/yr higher than during the first event.

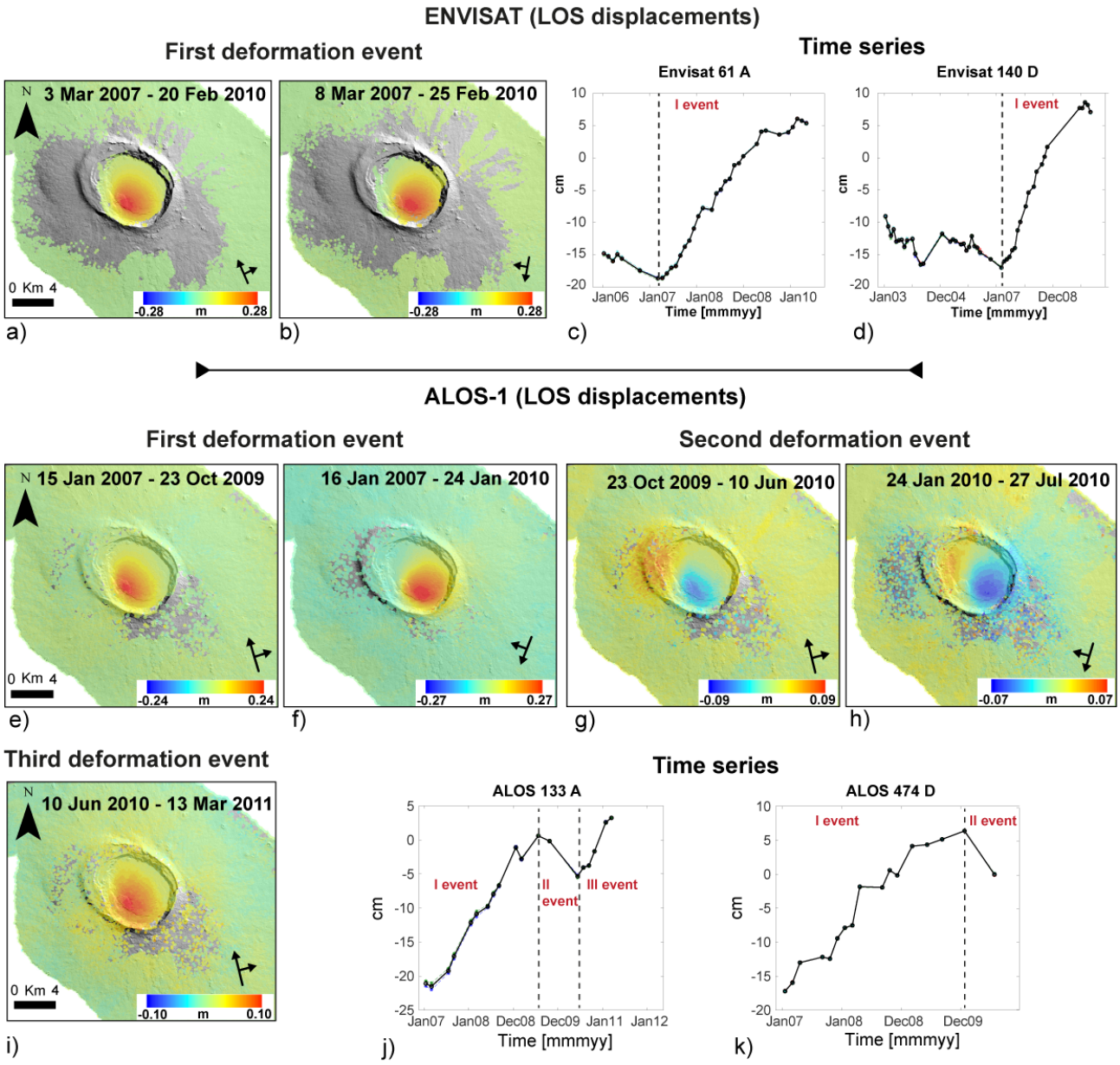

Figure 2. *Time-series results. (a) ENVISAT LOS displacement map for ascending orbit 61 (March 2007 - February 2010) and (b) for descending orbit 140 (March 2007 -February 2010). (c and d) ENVISAT time series (ts) (see star in Figure 1c for location). (e) ALOS-1 LOS displacement map for ascending orbit 133 (January 2007 to October 2009) and (f) for descending orbit 474 (January 2007 - January 2010). (g) ALOS-1 LOS displacement map for ascending orbit 133 (October 2009 to June 201) and (h) for descending orbit 474 (January 2010 to July 2010). (i) ALOS-1 LOS displacement map for ascending orbit 133 (June 2010 to March 2011). (j and k) ALOS-1 time series (see star in Figure 1c for location). In (a), (b) and (e)-(i) data are unwrapped, and spatially-correlated look-angle errors (including orbital ramps) are removed. Displacement maps are overlaid onto shaded relief map from WorldDEM data. LOS = line-of-sight.*

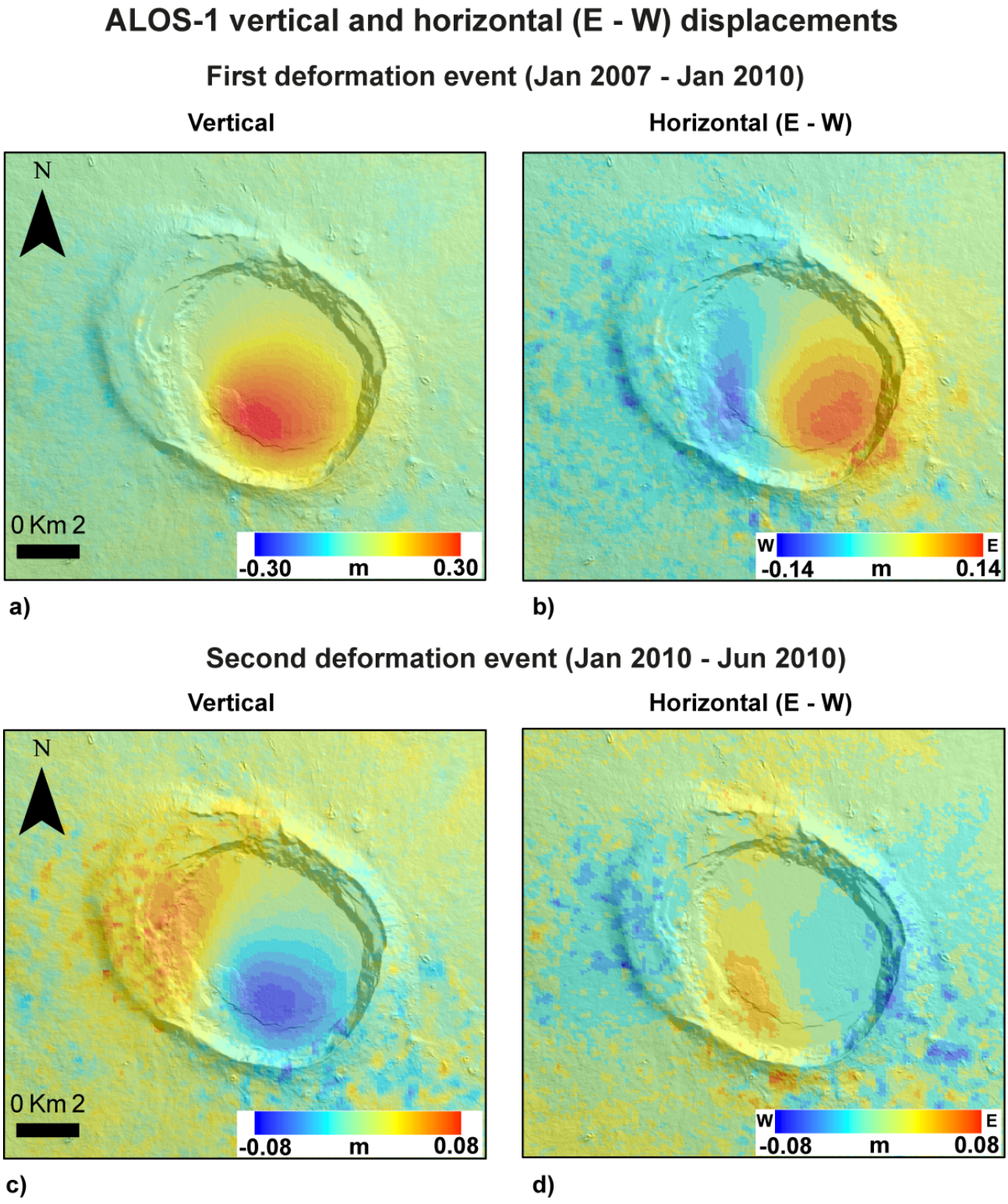

Figure 3. *ALOS-1 vertical and horizontal (E-W) displacement maps from the combination of ascending and descending LOS data (e.g., Wright et al., 2004). (a) Vertical and (b) horizontal displacements during the first deformation event, from January 2007 to January 2010. (c) Vertical and (d) horizontal (E-W) displacements during the second deformation event, from January 2010 to*

June 2010). In (b) and (d), blue colors represent westward horizontal motion and red colors eastward motion. Displacement maps are overlaid on a shaded relief map from WorldDEM data.

4.2 – Geodetic modelling

For the first deformation event we tested different source geometries. Point source (Mogi, 1958), finite spheroid (McTigue, 1987), and ellipsoid (Yang et al., 1988) sources were not able to reproduce the observed displacements (Figure S2 and Table S1). A better fit to the data was instead obtained using sill-like geometries, modelled as both CDM and RD (Figure 4). For the CDM, the model converged towards a rectangular, slightly inclined (<20°) sill, whose centroid lies at 2.2 ±0.1 km below the southern caldera floor, with opening of 0.78 ±0.1 m (Figure 4c-f, Table 1). The corresponding volume change (ΔV) is 9.7±1.1 $x10^{-3}$ km^3, with an average injection rate of 3.4 ±0.6 $x10^{-3}$ km^3/yr. To account for the asymmetric uplift, solutions converge towards a sill that is rotated about an axis orthogonal to it (ωX parameter, see Nikkhoo et al., 2017 for details). Using the RD we obtained solutions (Figure 4k-n; Table 2) that are similar to the CDM, with inversions that converged for an inclined (>30°) sheet, whose centre lies at 2.2 ±0.09 km below the southern caldera floor. The opening is 0.86±0.09 m, with an estimated ΔV of 7.1 (±0.6) $x10^{-3}$ km^3, corresponding to an average injection rate of 2.5±0.3 $x10^{-3}$ km^3/yr.

As the intra-caldera fault bounds the uplifting area (Figure 3a), we tested a combination of a slipping RD and a CDM/RD inflating sill. For the RD fault, we set the angle θ = 0, so that the two uppermost corners of the fault are at the same depth. In this configuration, the RD model becomes equal to that of Okada (1985) (Nikkhoo et al., 2017). Caldera inner ring faults are generally high-angle outward dipping (Acocella, 2007, and references therein). Therefore, we imposed a high dip angle (80°) and an outward dipping geometry. We also tested shallower dip angles (e.g., 70°) but obtained similar results (Figure S3, Table S2), implying that our data cannot fully constrain high dip angles. As for the fault length (L) and width (W), we set the prior PDFs so that a realistic aspect ratio L/W<5 (Leonard, 2010) could be maintained (Table 1).

In the case of the RD fault + CDM sill, the Bayesian analysis converged for a rectangular normal fault with uniform dip-slip of 0.53±0.23 m, whose centre lies at 0.96±0.11 km below the caldera floor (Figure 4g-j; Table 1). This fault is combined with a CDM sill, with opening of 0.6±0.08 m, whose centre is at 2.17±0.15 km below the southern caldera floor. With this source combination the rotational parameter ωX shows a significant decrease with respect to the CDM solution without the fault. The estimated ΔV is 8.55±1.05$x10^{-3}$ km^3 and the corresponding rate is 3±0.5$x10^{-3}$ km^3/yr, are slightly lower than that estimated in the CDM solution without the fault. As for the RD fault + RD

sill model, we obtained convergence for a rectangular normal fault with uniform dip-slip of 0.54±0.20 m. The centre of the fault is at 0.89± 0.08 km below the caldera floor (Figure 4o-r; Table 2), the RD sill has 0.6±0.07 m of opening, and its centre is at 2.20±0.14 km below the southern caldera floor. This RD sheet is less inclined (<30°) than in solutions without the fault and can be properly classified as a sill (Stephens et al, 2017). The estimated ΔV is 7.4±0.7 $x10^{-3}$ km^3 (injection rate of 2.55±0.35 $x10^{-3}$ km^3/yr), similar to that estimated without the fault, and ~12% lower than that estimated by the model RD fault + CDM sill.

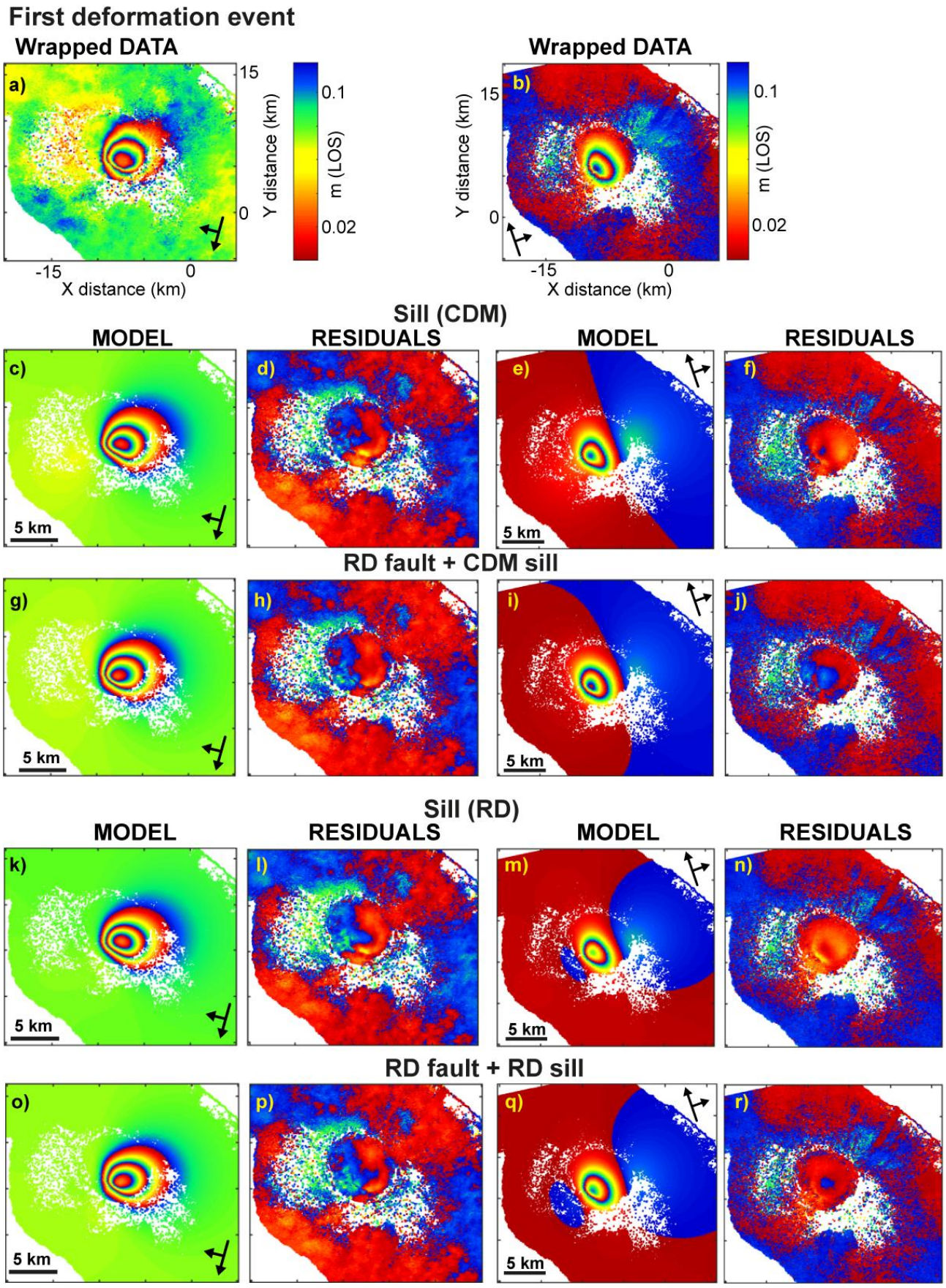
First deformation event
Wrapped DATA
a)
15
0
-15
0
X distance (km)
Y distance (km)
0.1
m (LOS)
0.02
Wrapped DATA
b)
15
0
-15
0
X distance (km)
Y distance (km)
0.1
m (LOS)
0.02
Sill (CDM)
MODEL
RESIDUALS
MODEL
RESIDUALS
c)
d)
e)
f)
5 km
5 km
RD fault + CDM sill
g)
h)
i)
j)
5 km
5 km
Sill (RD)
MODEL
RESIDUALS
MODEL
RESIDUALS
k)
l)
m)
n)
5 km
5 km
RD fault + RD sill
o)
p)
q)
r)
5 km
5 km

Figure 4. *(a) Wrapped ALOS-1 LOS displacements for descending track 474 (January 2007- January 2010), and (b) for ascending track 133 (January 2007 - October 2009). Each fringe (full colour cycle) represents 11.8 cm of LOS displacement. Local origin coordinates: longitude 91°05'W and latitude 0°49'S. (c and e) Predicted displacements for the CDM model, (g and i) for the CDM + RD fault model, (k and m) for the RD model, and o and q) for the RD fault + RD model, using the maximum a posteriori probability solutions. Panels (d),(f),(h),(j),(l),(n),(p),(r) show the relative residuals. LOS = line-of-sight; CDM= compound dislocation model; RD = rectangular dislocation.*

For the second deformation episode we tested both a combination of two CDMs and a combination of two RDs sources to test the possibility of simulating displacements from a deflating source and a lateral intrusion. We set prior PDFs for the length and width of the sills so that an aspect ratio >1/6 is maintained. Lower aspect ratios are considered to be less realistic, since sills tend to have tabular geometries with aspect ratios >1/6 (Thomson & Hutton, 2004; Currier et al., 2017). Furthermore, this aspect ratio is consistent with that of the first event (Table 1 and 2) and of sills emplaced at the other western Galápagos calderas of Sierra Negra, Fernandina and Wolf (Jónsson et al., 2005; Bagnardi et al., 2013; Xu et al., 2016).

In the case of two CDMs, the inversion converged for a first sill/inclined sheet, located approximately in the same position of the previously inflated sill (Figure S4), with a contraction (or closure) of -0.37±0.15 m, and a second rectangular sill placed below the western portion of the caldera with positive opening of 0.35±0.22 m. The corresponding volume changes are $-3.8\pm1.5 \times 10^{-3}$ km^3 (deflation rate $-7\pm3 \times 10^{-3}$ km^3/yr) for the deflating sill and $3.15\pm1.45\times10^{-3}$ km^3 (inflation rate of $6\pm3\times10^{-3}$ km^3/yr) for the inflated sill; therefore, the deflated and inflated sills of the second deformation event yield similar volume variations (Figure 5a-f, Table 2). The inner edge of the inflating sill partially overlaps that of the deflating sill (Figure S5).

In the case of two RDs (Figure 5g-l; Table 2), the geometry and position of the sources are similar to those from the solution with two CDMs. The deflating sill has a contraction of -0.48±0.23 m, with a corresponding volume loss of $-2.3\pm0.7 \times 10^{-3}$ km^3 (deflation rate $-4.25\pm1.75\times10^{-3}$ km^3/yr), while the inflating sill has an opening of 0.58±0.38 m, with a volume increase of $2.35\pm0.85\times10^{-3}$ km^3 (rate of $4.4\pm2\times10^{-3}$ km^3/yr), again comparable to the volume lost by the deflating sill.

Confidence intervals for the model parameters, for both the CDM and RD solutions, are broader than in the first event, likely due to a lower amplitude of the deformation signal leading to a lower signal-to-noise ratio in the data, with some parameters that remain poorly constrained by this analysis (Table 1, 2). As for the depths of the two sill centroids in both the RD and CDM models, the 95% confidence intervals only partially overlap, especially in the RD model where the centre of the inflating sill tends to be deeper than that of the deflating one. However, such difference may be due to the ~150 m

elevation change between the two areas under which the sills are emplaced (Lisowski, 2007), an effect for which we do not correct for in our half-space modelling approach.

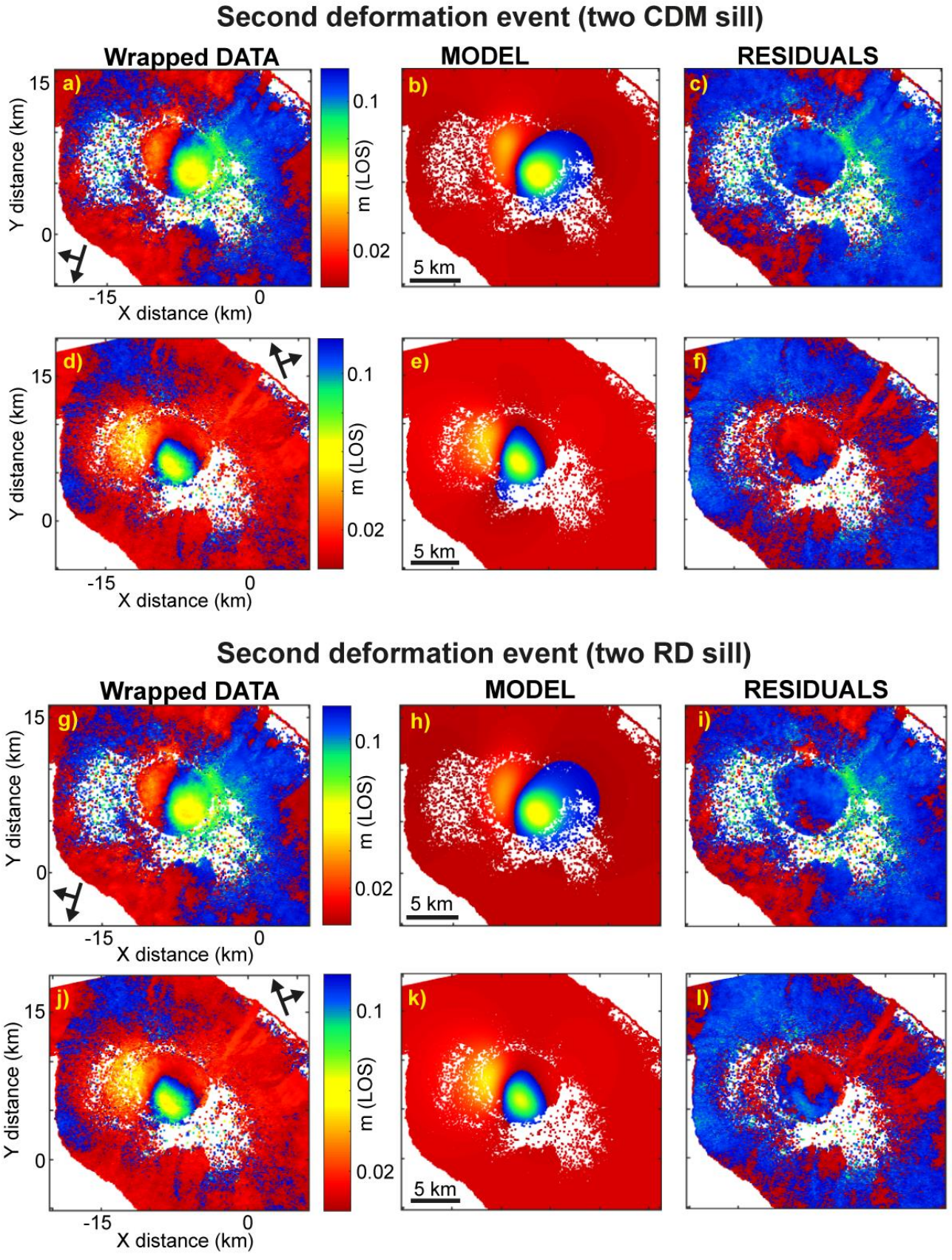

Figure 5. *(a and g) Wrapped ALOS-1 LOS displacements for descending track 474 (January 2010 - July 2010) and (d and j) for ascending track 133 (October 2009 - June 2010). Each fringe (full colour cycle) represents 11.8 cm of LOS displacement. Local origin coordinates: longitude 91°05'W and latitude 0°49'S. (b and e) Predicted displacements for two CDM models using the maximum a posteriori probability solution and (c and f) the related residuals. (h and k) Predicted displacements for two RD models using the maximum a posteriori probability solution and (i and l) the related residuals. LOS = line-of-sight; CDM = compound dislocation model; RD = rectangular dislocation.*

Table 1 *Results of the Bayesian analysis.*

First event (CDM)											
	X (m)	**Y (m)**	**Z (m)**	**ω X**	**ω Y**	**ω Z**	**ax (m)**	**ay (m)**	**az (m)**	**Op. (m)**	**ΔV (x10^6 m^3)**
Optimal	-7971	5841	2180	-36	16	211	1736	1365	242	0.76	9.5
2.50%	-8054	5727	2104	-40	14	209	1655	1230	203	0.69	8.6
97.50%	-7888	5928	2316	-34	19	215	1851	1478	287	0.88	10.8
Lower	-10000	3000	2000	-50	-30	180	800	800	4	0	
Upper	-5000	8000	4000	50	40	360	4000	4000	500	10	
First event (CDM + fault)											
FAULT											
	X (m)	**Y (m)**	**Z (m)**	**L (m)**	**W (m)**	**Dip[a]**	**Strike**	**Rake[a]**	**Slip (m)**		
Optimal	-8863	5223	1030	1765	908	80	122	-90	0.39		
2.50%	-8932	5185	854	1562	420	80	119	-90	0.31		
97.50%	-8802	5308	1071	1942	940	80	126	-90	0.76		
Lower	-10000	4000	700	800	400	80	90	-90	0.1		
Upper	-5000	6000	1600	2900	950	80	180	-90	2		
CDM											
	X (m)	**Y (m)**	**Z (m)**	**ω X**	**ω Y**	**ω Z**	**ax (m)**	**ay (m)**	**az (m)**	**Op. (m)**	**ΔV (x10^6 m^3)**
Optimal	-7783	5938	2144	-19	-15	273	1581	1935	214	0.57	8.7
2.50%	-7883	5850	2025	-23	-19	269	1437	1848	104	0.52	7.5
97.50%	-7735	5991	2323	-17	-12	277	1641	2016	252	0.68	9.6
Lower	-10000	3000	2000	-50	-40	180	800	800	4	0	
Upper	-5000	8000	4000	50	30	360	4000	4000	500	10	
Second event (two CDM)											
First CDM											
	X (m)	**Y (m)**	**Z (m)**	**ω X**	**ω Y**	**ω Z**	**ax (m)**	**ay (m)**	**az (m)**	**Op. (m)**	**ΔV (x10^6 m^3)**
Optimal	-8240	5832	2326	7	32	112	836	1948	371	-0.37	-3.9
2.50%	-8494	5555	2105	-11	17	109	806	1373	138	-0.51	-5.3
97.50%	-7755	6328	2815	12	47	144	1255	2353	578	-0.22	-2.3
Lower	-9500	4000	2000	-20	0	60	800	800	1	-5	
Upper	-6500	7500	4000	20	50	360	2500	2800	600	0	
Second CDM											
	X (m)	**Y (m)**	**Z (m)**	**ω X**	**ω Y**	**ω Z**	**ax (m)**	**ay (m)**	**az (m)**	**Op. (m)**	**ΔV (x10^6 m^3)**
Optimal	-10275	7468	2174	15	-10	257	2470	876	527	0.18	2.8
2.50%	-10582	7215	2154	-3	-27	235	1140	714	15	0.13	1.7
97.50%	-9810	7981	3726	42	-1	292	2743	1523	636	0.57	4.6
Lower	-14000	5800	2000	-10	-60	220	700	700	1	0	
Upper	-8000	10000	4000	50	0	359	3000	3000	700	5	

Notes. Optimal = maximum a posteriori probability solution. The percentages 2.50% and 97.50% are the lower and upper boundaries of the 95% credible intervals. Lower and Upper are the bounds of the prior distribution used for the inversion. X and Y are the local coordinates of the centre of CDM and the centre of the RD fault. Local coordinates origin (see Figure 4a and b): longitude 91° 05' W and latitude 0° 49' S. Z is the depth (with respect to the caldera floor) (positive downward). ωZ is the strike angle, ω X and ω Y are respectively the rotational angle along the X and Y direction. ax, ay and az are the lengths of the semi-axes of the CDM along the x, y, and z axes, respectively (see Nikkhoo et al., 2017 for a better explanation). Op. is the opening. L is the Length of the fault, while W is its width. Rake is the rake of the fault, while strike is its strike angle. Dip is the dip angle of the fault. Volume change (ΔV) has been calculated with the formula ΔV=4(opening)*[(ax*ay)+(ay*az)+(ax*az)] (Nikkhoo et al., 2017).*

[a] *Parameter held fixed.*

Finally, we inverted data spanning the third deformation event using a RD model (Figure 6). Likely due to the low-magnitude deformation signal and to the single viewing geometry (ascending), the geometric parameters of the RD source are not well constrained (Table 3). However, the narrower range of solutions of the ΔV (4.45±2.05x10^{-3} km^3, Table 3) indicates this is because the parameters on which the ΔV depends trade off against each other (Figure S6). The corresponding injection rate is 5.85±2.75x10^{-3} km^3/yr, which is ~57 % higher than the injection rate of the first deformation event and ~25 % higher than that of the inflated sill in the second event. The depth of the centre of the RD source is at 3.4±0.7 km below the caldera floor.

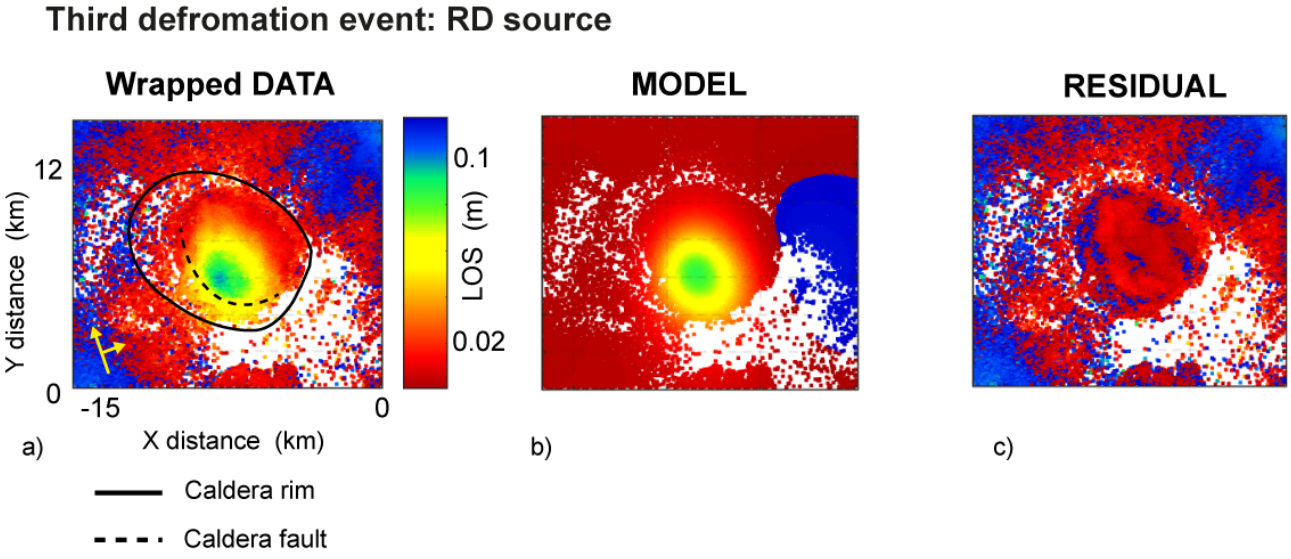

Figure 6. *(a) Wrapped ALOS-1 LOS displacements for ascending track 133 (June 2010 and March 2011). Each fringe (full colour cycle) represent 11.8 cm of LOS displacement. Local origin coordinates: longitude 91°05'W and latitude 0°49'S. (b) Predicted displacements for a RD model using the maximum a posteriori probability solution. (c) Related residual. LOS = line-of-sight; RD = rectangular dislocation.*

Table 2 *Results of the Bayesian analysis.*

					First event (RD)					
	X (m)	**Y (m)**	**Z (m)**	**L (m)**	**W (m)**	**θ**	**Dip**	**Strike**	**Op. (m)**	**ΔV (x10^6 m^3)**
Optimal	-8056	5714	2174	3662	2286	-37	35	329	0.83	7
2.50%	-8126	5633	2109	3523	2084	-41	34	326	0.77	6.5
97.50%	-7998	5770	2294	3819	2458	-32	37	332	0.96	7.7
Lower	-11000	2000	2000	800	800	-60	0	0	0	
Upper	-5000	8000	4000	4500	4000	0	50	360	10	
					First event (RD Fault + RD)					
					Fault					
	X (m)	**Y (m)**	**Z (m)**	**L (m)**	**W (m)**	**Dip[a]**	**Strike**	**Rake[a]**	**Slip (m)**	
Optimal	-8858	5225	871	1664	474	80	121	-90	0.58	
2.50%	-8906	5164	820	1507	406	80	119	-90	0.35	
97.50%	-8787	5260	971	1844	764	80	125	-90	0.74	
Lower	-10000	4000	700	800	400	80	90	-90	0.1	
Upper	-5000	6000	1600	2900	950	80	180	-90	2	
					RD					
	X (m)	**Y (m)**	**Z (m)**	**L (m)**	**W (m)**	**θ**	**Dip**	**Strike**	**Op. (m)**	**ΔV (x10^6 m^3)**
Optimal	-7829	5895	2164	3142	4003	31	26	333	0.58	7.3
2.50%	-7913	5828	2058	2968	3811	27	24	328	0.53	6.7
97.50%	-7777	5942	2341	3299	4113	37	29	337	0.67	8.1
Lower	-11000	2000	2000	800	800	0	0	240	0	
Upper	-5000	8000	4000	4400	4500	50	50	360	10	
					Second event (two RD)					
					RD					
	X (m)	**Y (m)**	**Z (m)**	**L (m)**	**W (m)**	**θ**	**Dip**	**Strike**	**Op. (m)**	**ΔV (x10^6 m^3)**
Optimal	-8282	5866	2675	4380	918	14	19	294	-0.56	-2.3
2.50%	-8582	5582	2322	3245	911	-28	5	281	-0.71	-3
97.50%	-7833	6269	2943	4968	1913	25	30	335	-0.25	-1.6
Lower	-10000	4000	2100	1000	900	-35	-1	180	-2	
Upper	-5000	8000	4000	5200	4000	35	35	360	0	
					RD					
	X (m)	**Y (m)**	**Z (m)**	**L (m)**	**W (m)**	**θ**	**Dip**	**Strike**	**Op. (m)**	**ΔV (x10^6 m^3)**
Optimal	-10029	7562	3080	1331	4083	49	23	217	0.43	2.3
2.50%	-10537	7251	2788	915	2495	5	6	195	0.21	1.5
97.50%	-9797	8054	3825	2274	5479	59	33	256	0.96	3.2
Lower	-11000	5000	2100	900	2000	-1	-10	100	0	
Upper	-7000	9000	4000	2500	6000	60	40	360	2	

Notes. Optimal = maximum a posteriori probability solution. The percentages 2.50% and 97.50% are the lower and upper boundaries of the 95% credible intervals. Lower and Upper are the bounds of the prior distribution used for the inversion. X and Y are the local coordinates of the centre of RD.

*Local origin coordinates (see Figure 4a and b): longitude 91° 05' W and latitude 0° 49' S. Z is the depth (with respect to the caldera floor) (positive downward). θ is the angle between the RD upper edge and the intersection of the RD plane with the free surface. L and W are respectively the length and the width. Rake is the rake of the fault. Op. is the opening. Dip is the dip angle. Strike is the strike angle (see Nikkhoo et al., 2017 for a better explanation of all these parameters). ΔV is the volume change calculated with the formula ΔV=L*W*Op. RD = rectangular dislocation.*

[a] *Parameter held fixed.*

Table 3 *Results of the Bayesian analysis of the third deformation event using an RD source.*

	X (m)	Y (m)	Z (m)	L (m)	W (m)	θ	dip	strike	Op. (m)	ΔV (x10^6 m^3)
Optimal	-7971	6086	3207	2521	3788	19	23	10	0.42	4.1
2.50%	-8560	5788	2674	1035	2111	1	4	1	0.26	2.4
97.50%	-7647	6566	4131	3179	4143	34	37	64	1.92	6.5
Lower	-11000	2000	2300	1000	2000	0.1	0	0	0	
Upper	-5000	8000	5000	3700	4200	35	50	180	5	

*Optimal = maximum a posteriori probability solution. The percentages 2.50% and 97.50% are the lower and upper boundaries of the 95% credible intervals. Lower and Upper are the bounds of the prior distribution used for the inversion. X and Y are the local coordinates of the centre of RD. Local origin coordinates: longitude 91° 05' W and latitude 0° 49' S. Z is the depth (with respect to the caldera floor) (positive downward). θ is the angle between the RD upper edge and the intersection of the RD plane with the free surface. L and W are respectively the length and the width. Op. is the opening. Dip is the dip angle. Strike is the strike angle (see Nikkhoo et al., 2017 for a better explanation of all these parameters). ΔV is the volume change calculated with the formula ΔV=L*W*Op. RD = rectangular dislocation.*

5 - Discussion

5.1. – Interpretation of the three deformation events

From the analysis and modelling of InSAR data, we infer that Alcedo experienced a phase of non-eruptive unrest between 2007 and 2011, which can be divided in three main events.
We model the first deformation event as either due to an inflating sill or the combination of an inflating sill and reactivation of the southern intra-caldera fault. In both cases, the estimated volume changes are similar. However, solutions that include the fault better reproduce the observed asymmetric deformation, especially on the ALOS-1 ascending track. Models that include the fault also converge towards a more horizontal sill geometry, as the fault accounts for part of the asymmetric deformation, as for example previously observed at Sierra Negra (Jónsson, 2009). Since this fault has been interpreted as a pre-existing caldera fault (Geist et al., 1994), we modelled it using the typical outward dipping geometry (Acocella, 2007). However, we cannot exclude any inward dipping geometry, as inferred for the 2005 uplift of Sierra Negra (Jónsson, 2009). In any case, even when using an 80° inward dipping fault we obtain similar results (Figure S7 and Table S3).

The second deformation event is consistent with the partial emptying of the previously inflated sill (~44% of contraction of the previously intruded volume for the CDM, ~30% for the RD) and the intrusion of a sill in the western caldera. Other processes such as cooling and crystallisation of previously emplaced magma are less probable since they could not easily explain such a rapid (<6 months) and significant (~30-44%) volume loss (Caricchi et al., 2014). These processes would also not account for the contemporaneous uplift of the western caldera rim. Similarly, viscoelastic relaxation cannot play an important role during this deflationary event, as this mechanism would require a period of transition, from uplift to subsidence, characterized by a decrease in the uplift rate (Newman et al., 2006). Such transition does not seem to occur at Alcedo, where the InSAR data show a sudden change from uplift to subsidence. The similar volumes of the deflating sill and that of the inflated sill, as well as their juxtaposition, suggest a lateral propagation of the sill formed during the first event from below the caldera (Figure 7). Since in some of our solutions the inflated sill is deeper than the deflating one, some downward migration of magma from the deflating sill may have occurred during the lateral propagation, as proposed at larger scale for the 2001-2002 subsidence occurred at Sierra Negra (Geist et al., 2006).

This process has been observed previously, though reaching a much farther lateral propagation, at other Western Galápagos calderas, such as Fernandina (Bagnardi et al., 2013), and may have been controlled by the stress field that results from the topographic unloading due to the caldera depression

(Corbi et al., 2015, and references therein). However, in the case of Alcedo, the lateral propagation of the sill was limited (only a few kilometres) and the intrusion aborted soon, without any eruption, near the caldera boundary, where important stress changes occur (Corbi et al., 2015, and references therein). We interpret this aborted lateral magma propagation to the discontinuity in the supply of magma from depth. This event underlies the importance of a continuous supply in the propagation of magma to the surface and feed eruptions.

Finally, the third deformation event is compatible with the inflation of a source approximately located in the same position as the source that inflated during the first event and deflated during the second event (Figure 7). Even if the source depth is not as well constrained, its 95% confidence interval (Table 3) shows only a partial overlap with previous sources, suggesting that this intrusion may be emplaced below the one that caused the first episode of uplift. The positive volume change during the third event corresponds to ~60 % of that observed during the first event.

We can explain the asymmetric uplift during the first event as the combined effect of magma addition to the source and fault reactivation. The asymmetric deformation also observed during the second and third events suggests that the same fault, even though not included in our models, may have been subsequently active. The deformations at Alcedo from 1992 to 2001 (Amelung et al., 2000; Hooper et al., 2007), occurred in the same area and showed the same asymmetrical pattern, suggesting that this fault was active also during the previous unrest.

5.2 A general model for Alcedo

According to the general evolutionary model for western Galápagos volcanoes, Alcedo may be in a dying phase and its magmatic system may be characterized by a mush zone that should be no longer in a thermal steady state, and cooler with respect to that of the nearby calderas (Geist et al., 2014; Harpp & Geist, 2018). Geist et al (1994) suggested, on morphological and geologic evidence, that the shallower portion of the magmatic system of Alcedo lies now below the southern part of the caldera, where Alcedo also hosts a shallow (located above sea level) hydrothermal system (Goff et al., 2000). Our data, as well as the geodetic data from 1992 to 2001 (Amelung et al., 2000; Hooper et al., 2007), support this hypothesis, suggesting that this shorter-term deformation (years long) focuses in the southern part of the caldera. The 2-3 km depth of the sills centroids in our study is also consistent with the depth of the source that caused the subsidence of the southern part of the caldera from 1997 to 2001 (Hooper et al., 2007). Furthermore, this depth agrees with that of the top of the shallow magmatic systems of the nearby calderas at Fernandina, Sierra Negra and Wolf (from 1 to 3 km depth below the caldera; Jónsson, 2009; Bagnardi et al., 2013; Stock et al., 2018). Such depths are more

consistent with those of magmatic sources than with that of the shallow hydrothermal system of Alcedo. However, we cannot exclude a minor contribution of the hydrothermal system to the total deformation signal, which could be possibly triggered by the inflow of new magmatic fluids linked to the new intrusions (Hurwitz et al., 2007). Our observations suggests that sill inflation during the first and third events were related to the replenishment of the shallow magmatic system, possibly as intrusions within the magmatic mush, from which the magma propagated laterally (during the second event). However, not only did the lateral propagation of magma not result in an eruption, but it also terminated as a stalled intrusion at a short distance. This aborted lateral propagation of the sill is interpreted as being due to the fact that the magmatic system was not being replenished during the second deformation event, or was being replenished at much lower rates, as indicated by the similar volume changes of the inflating laterally propagating sill and the deflating sub-caldera sill. The second event at Alcedo thus may provide an interesting example of magma propagation aborted by the lack of continuous replenishment of the main shallow reservoir. Pressure decrease in the feeding sill and magma solidification in the propagating sill (Rubin, 1995; Rivalta, 2010) may both have caused the arrest of the laterally propagating sill, although stress changes caused by the morphology of the caldera rim may have also contributed to its arrest (Corbi et al., 2015).

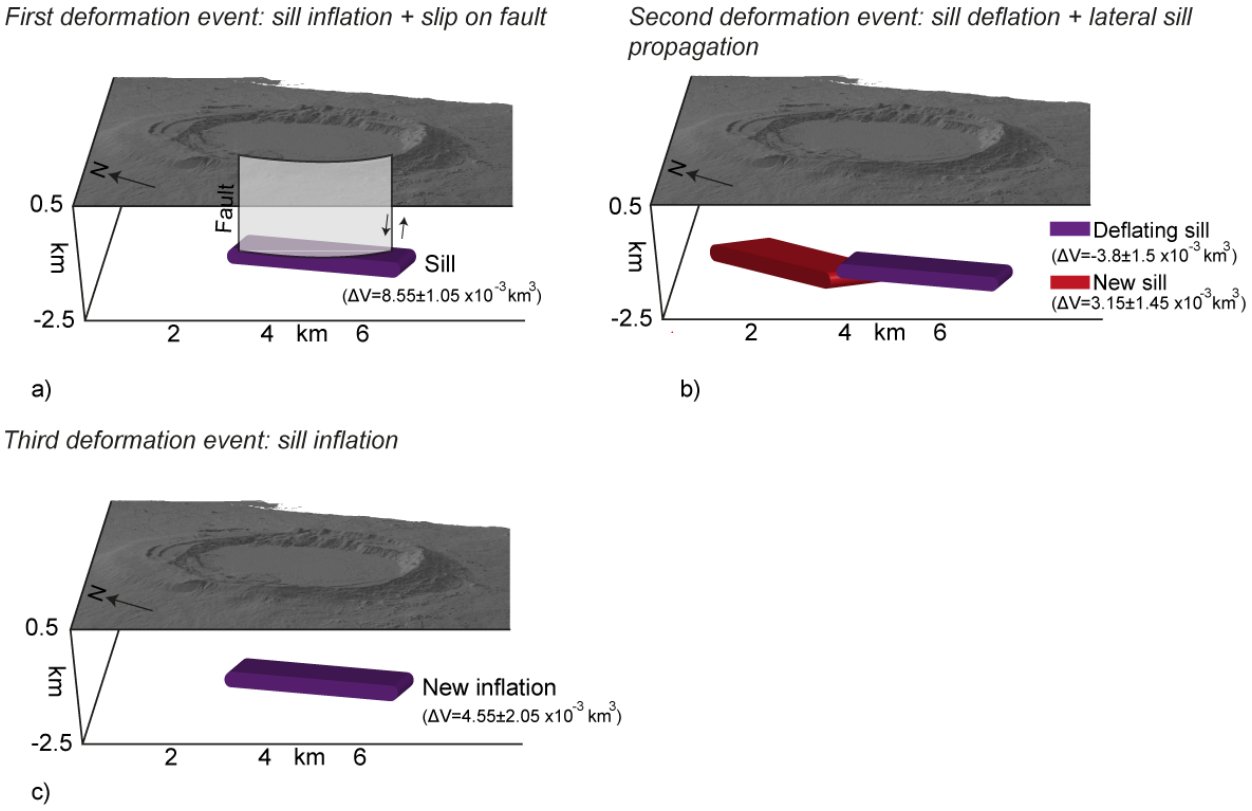

Figure 7. *Conceptual models summarizing the three deformation events at Alcedo. (a) First event with sill inflation and reactivation of an intra-caldera fault. (b) Second event: lateral magma propagation and sill deflation. (c) Third event: sill re-inflation.*

Our data suggest that the sill responsible for the third event may have been emplaced below that of the first event, even if replenishment of the former sill cannot be excluded. Thus, the intrusive system of Alcedo may grow through the emplacement of stacked sills, possibly within the magmatic mush, and not necessarily by the replenishment of the same sill. Our results allow for the possibility that the stacked sills touch each other. This is consistent with the fact that a partially molten magma body can act as a rheological barrier for the new intrusion, hindering its upward propagation (Galetto et al., 2017), as also confirmed by some eroded laccoliths and plutons (Miller et al., 2011, Leuthold et al., 2012).

A further insight obtained from the analysis of surface deformation data during recent decades is its possible relation with the longer-term (decades at least) behaviour of the caldera. During the time period here analysed, as well as between 1992 and 2001 (Amelung et al., 2000; Hooper et al., 2007, the amount of uplift was greater than that of subsidence, resulting in a net asymmetric uplift of the southern caldera floor. This asymmetric uplift matches with the morphology of the southern part of the caldera, which shows ~30 m of trapdoor uplift (Figure 1) confined by the same intra-caldera fault that was active during our first event and probably the subsequent ones. We speculate that the trapdoor uplift geodetically detected here may represent the nearly-instantaneous expression of a decades-to-centuries long process of weak resurgence at Alcedo (Geist et al., 1994). These geodetically detected uplift episodes would thus provide the opportunity to observe a specific moment of growth of a resurgence, implying that resurgence is a discontinuous and incremental process, also involving episodes of limited subsidence. This in turn implies that resurgence results from the repeated and cumulative emplacement of shallow intrusions within the mushy magmatic system, each with its distinct history, probably supported by the thermal state of the crust, as suggested for the Campi Flegrei caldera (Amoruso et al., 2017). The weak resurgence of Alcedo would be related to its relatively late evolutionary stage (dying phase, Geist et al., 2014), characterized by a cooling shallow magmatic system shifted towards a more felsic composition and, as also witnessed during the second deformation event, by a discontinuous magma supply. All these features are characteristic of most of the resurgent calderas and could promote the accumulation of magma at depth and resurgence (Galetto et al., 2017). The trapdoor resurgence at Alcedo is also similar in shape (asymmetric) and extent (several tens of m) to that observed at nearby Sierra Negra (Galetto et al., 2017, and references therein), and is among the very rare examples of resurgence observed at basaltic calderas. However,

resurgence at the caldera of Alcedo grows with lower (up to one order of magnitude) rates than at Sierra Negra (Geist et al., 2006), which could be related to the much lower magma supply to Alcedo.

Therefore, the non-eruptive unrest at Alcedo described here, as well as that which occurred between 1992 and 2001, may represent short-term intrusion episodes related to a longer-term resurgence. These geodetically observed episodes provide the unusual opportunity to witness the short-term stages of growth of a rare resurgence in a basaltic caldera.

6 Conclusions

We have identified two distinct episodes of shallow sill emplacement at Alcedo, triggering a net uplift of ~26 cm from January 2007 to January 2010 and from June 2010 to March 2011. In between (January 2010 – June 2010), the previously intruded sill, even though not replenished, migrated laterally, without erupting. We relate the arrest of the sill to the discontinuous supply of magma, supported by our estimates of the volume variations of the deflated and inflated sills in the first half of 2010. This indicates the importance of the continuity in the supply of magma to have eruptive unrest.

We also highlight that all the deformation episodes from 1992 to 2011 occurred in the southern caldera floor and showed the same asymmetric pattern, bordered by the same intra-caldera ring fault to the south. This shorter-term deformation is consistent, in location (southern part of the caldera) and shape (asymmetry) with the longer-term one deduced from geologic evidence, highlighting a weak (~30 m uplift) resurgence. This consistency suggests that Alcedo has been experiencing incremental and discontinuous episodes of growth of its resurgent block, related to the emplacement of multiple sills, a rare occurrence to witness at basaltic calderas. Future studies should investigate if the intrusive magmatic systems of the other western Galápagos calderas also grow through the emplacement of multiple stacked sills, as inferred at Alcedo.

Acknowledgments

We thank K. Spaans, R. Amey and J. Giniaux for their helpful suggestions. We also thank D. Geist and an anonymous reviewer for the constructive suggestions.

MB was supported by the NERC Centre for the Observation and Modelling of Earthquakes, Volcanoes and Tectonics (COMET) and by an appointment to the NASA Postdoctoral Program at

the Jet Propulsion Laboratory, administered by the Universities Space and Research Association (USRA) through a contract with NASA.

The Grant to Department of Science, Roma Tre University (MIUR-Italy Dipartimenti di Eccellenza, ARTICOLO 1, COMMI 314 – 337 LEGGE 232/2016) is gratefully acknowledged.

The Envisat data are distributed by the European Space Agency (ESA) via ESA's Virtual Archive (http://eo-virtual-archive4.esa.int/) in the framework of the Geohazard Supersites and Natural Laboratory initiative. The ALOS-PALSAR data are copyright JAXA/METI.

All the other information that support this study are in the Supporting Information file.

Chapter 3

Article submitted to *Journal of Geophysical Research: Solid Earth*
(date of submission: 8/8/2019)

The 2008 eruptive unrest at Cerro Azul volcano (Galápagos) revealed by InSAR data and a new method for geodetic modelling.

Federico Galetto[1], Andrew Hooper[2], Marco Bagnardi[2,3] and Valerio Acocella[1]

[1] Università degli Studi di Roma Tre, Dipartimento di Scienze, Rome, Italy

[2] COMET, School of Earth and Environment, University of Leeds, Leeds, UK

[3] Now at NASA Goddard Space Flight Center, Greenbelt, MD, USA

Corresponding author: Federico Galetto (federico.galetto@uniroma3.it).

Key points (<140 characters):

1) The 2008 eruption of Cerro Azul was preceded by a pre eruptive inflation.
2) The 2008 eruptive unrest at Cerro Azul (Galápagos) was associated to the propagation of a radial dike.
3) To avoid unwrapping errors, we applied a new method for the inversion of InSAR data, based on wrapped phase differences.

Key words: Unrest, Cerro Azul, unwrapping errors, geodetic modelling, radial dike, Galápagos.

Abstract

Understanding unrest is fundamental to mitigate volcanic risk. Cerro Azul is one of the most active volcanoes in the western Galápagos Islands, but its unrest episodes are poorly studied. Here an unrest, started in 2007, culminated in two eruptive phases from May 29th to June 11th 2008. We investigate this unrest and the associated eruptions using interferometric synthetic aperture radar (InSAR) data

and geodetic modelling. To overcome the unwrapping errors affecting some of our InSAR data we invert the wrapped phase directly by estimating the integer ambiguities simultaneously with the geophysical parameters. Our results highlight how the eruption was preceded by long-term pre-eruptive inflation (October 2007 – April 2008). During the first eruptive phase, most of the magma responsible for the inflation fed the lateral propagation of a radial dike, which caused a first deflation of the magmatic reservoir. During the second eruptive phase, the further lateral propagation of the dike fed a radial eruptive fissure at the base of the edifice, causing further deflation of the magmatic reservoir. From the first to the second eruptive phase, the radial dike changed its strike when it propagated from below the volcanic edifice to a topographic low, between Cerro Azul and Sierra Negra.

1 - Introduction

Basaltic shield volcanoes with a summit caldera usually experience repeated unrest, during which the baseline of the monitoring parameters (e.g. degassing, seismicity and ground deformation) deviates from quiescence (Acocella et al., 2015; Newhall & Dzurisin, 1988). Unrest episodes have important volcanic hazard implication, as nearly all eruptions are preceded by unrest episodes, although not all unrest necessarily culminates into an eruption (Acocella et al., 2015; Biggs et al., 2014; Sandri et al., 2017). Understanding the nature and possible outcome of unrest becomes, therefore, crucial for the assessment of volcanic risk. Adequate ground-based monitoring is often limited by the fact that many volcanic systems lie in remote areas, hindering the study of many unrest episodes. Volcano monitoring through remote sensing techniques, such as Synthetic Aperture Radar Interferometry (InSAR) can, on the other hand, overcome these limitations and allow investigating unrest globally (Pinel et al., 2014). InSAR has proven to be successful at different volcanic provinces worldwide (e.g. Amelung et al., 2007; Baker & Amelung, 2012; Biggs et al., 2016; Ebmeier et al., 2013; Gonzalez et al., 2015; Poland et al., 2017; Sigmundsson et al., 2015; Wright et al., 2006). Among these, the western Galápagos calderas have been extensively studied using InSAR data, improving our knowledge on these volcanoes and shallow magma transfer mechanisms (Bagnardi et al., 2013; Chadwick et al., 2011; Galetto et al., 2019; Jonsson, 2009; Xu et al., 2016). Here we investigate the 2007-2008 unrest of Cerro Azul volcano (western Galápagos), which culminated in two eruptive phases, from May 29th to June 11th 2008, using InSAR data and geodetic modelling. To overcome unwrapping errors, due to erroneous estimates of the phase integer ambiguities during the so-called unwrapping process (e.g., Hooper & Zebker, 2007) that can bias InSAR data inversion results, we propose a method to model the wrapped data directly, overcoming any unwrapping problem. We

adopt this method to interpret data from the ENVISAT satellite that are clearly affected by unwrapping errors. Results highlight how most of the deformation is related to the propagation of a radial dike, which triggered the two eruptive phases.

2 - Geological background

The Galápagos Archipelago, in the eastern Pacific Ocean, is a hot spot magmatic province. The islands lie above a broad and thick platform over young (<10 Ma) oceanic lithosphere (Figure 1a) (Feighner & Richards, 1994; Rychert et al., 2014). Most of the current volcanic activity focuses on the seven shield volcanoes forming the western Galápagos islands of Fernandina and Isabela, in the upwelling region of the hot spot (Hooft et al., 2003; Gibson & Geist, 2010; Villagomez et al., 2014). These volcanoes are large, flexurally-supported shields with summit calderas, forming a distinct volcanological, petrological, geochemical and structural group with respect to the eastern Galápagos volcanoes (White et al., 1993; Feighner & Richards, 1994; Harpp & Geist, 2018). Among the western Galápagos volcanoes is Cerro Azul, one of the six making up Isabela Island (Naumann & Geist, 2000). Cerro Azul has a maximum elevation of 1640 m above sea level (a.s.l.), with gently sloping lower flanks (generally <4°), steep upper flanks (generally ~25°) and a flat summit rim (~1 km wide) that surrounds a 450-meter-deep nested caldera (Naumann & Geist, 2000). This 4.2 km x 2.2 km wide caldera, with major axis oriented NW-SE, results from repeated cycles of collapse and is the smallest, both in volume (3.1 km^3) and area (9.5 km^2), among those of the western Galápagos (Naumann and Geist, 2000).

Cerro Azul has erupted some of the most primitive magmas of the western Galápagos and is the only western Galápagos volcano to have erupted both tholeiitic and alkali basalts (Naumann & Geist, 1999; Naumann et al. 2002). These characteristics have been related to its juvenile stage and relatively low magma supply rates (Naumann & Geist, 1999; Naumann et al. 2002). As a result, Cerro Azul is inferred to lack a well-developed shallow magmatic system, with probably only a hot and partially developed deep mushy system at 5 km below sea level (Geist et al., 2014: Harpp & Geist, 2018). A series of north- to northwest-trending landslide scarps suggests the collapse of the southwestern flank (Naumann and Geist, 2000). The failure of this flank, due to its position adjacent to the steep submarine escarpment (3 km height) (Figure 1b) (Geist et al., 2008), promotes the formation of northwest-southeast oriented eruptive fissures (Naumann & Geist, 2000; Naumann et al., 2002).

More in general, Cerro Azul shows the typical eruptive pattern of the western Galápagos volcanoes, with circumferential eruptive fissures just outside the caldera rim and radial fissures along the volcano's flanks (Chadwick and Howard, 1991). The stress field allowing the formation of both types of fissures seems to be mainly controlled by the gravitational unloading after caldera collapse and the

stresses from previous intrusions (Bagnardi et al, 2013; Corbi et al., 2015; 2016), with further contribution from the load of the edifice and the pressurization of a flat-topped magma chamber (Chadwick & Dieterich, 1995).

Before the last eruption in 2008, ten witnessed eruptions have occurred at Cerro Azul since 1932. During the previous two eruptions (1979 and 1998), radial eruptive fissures opened in the same area (eastern flank) as the 2008 eruption (Mouginis-Mark et al., 2000; Naumann & Geist, 2000; Rowland et al., 2003; Teasdale et al., 2005).

The 2008 eruption of Cerro Azul occurred in two phases (Global Volcanism Program, 2008). The first phase (from May 29th to June 1st) began with the effusion of a lava flow from an eruptive fissure immediately outside the eastern caldera rim (Figure 1c). Successively, further eruptive fissures opened on May 30th, parallel to the former, on the eastern upper flank (Figure 1c). All these fissures ceased their effusive activity by June 1st. The second eruptive phase (June 3rd to June 11th) was characterized by effusive activity from a new radial fissure located in a flatter area near the edge of the lower eastern flank of Cerro Azul (Figure 1).

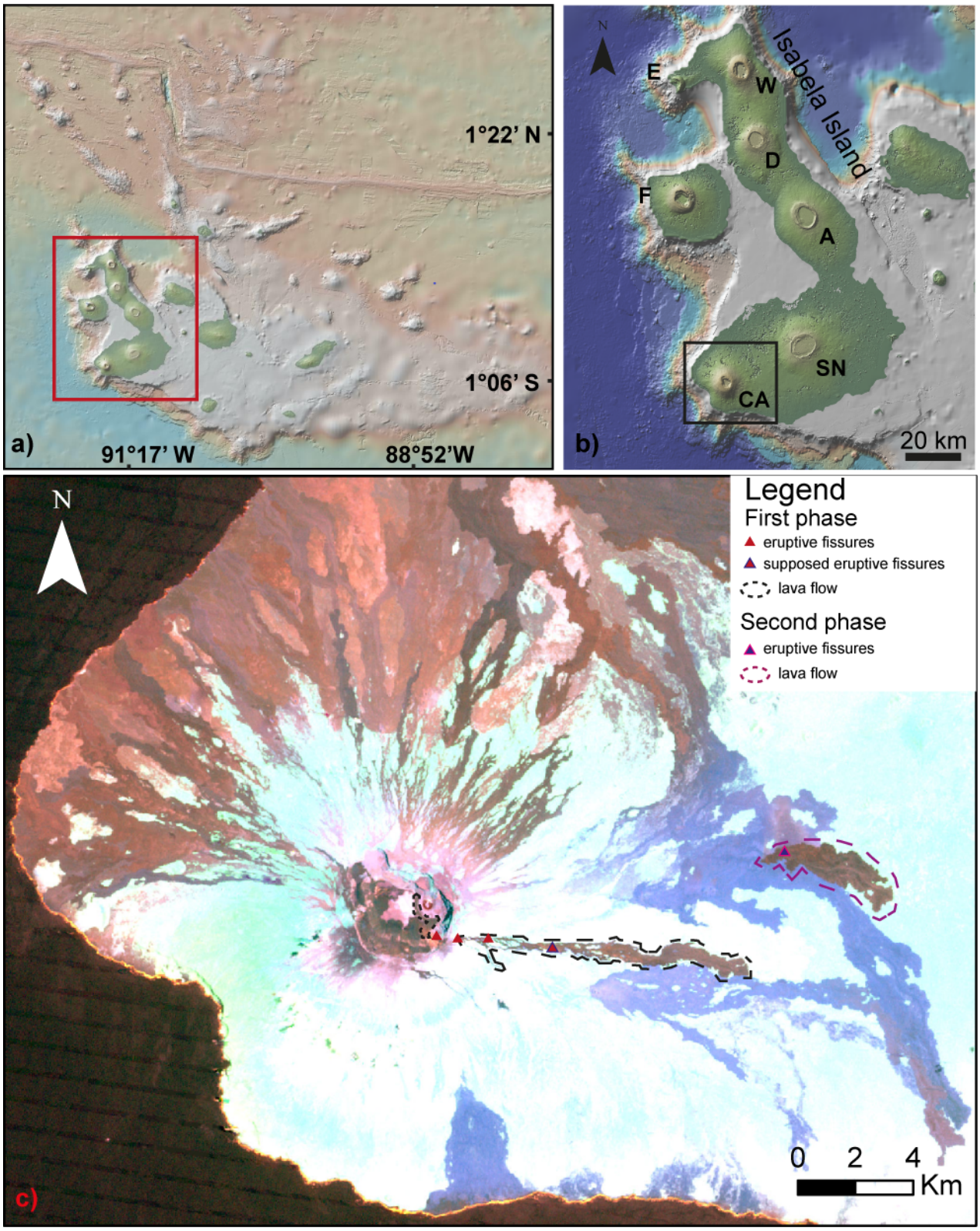

Figure 1 *a) Galápagos archipelago. The red square outlines the extent of panel b. b) The western Galápagos islands of Fernandina (F) and Isabela, on which lie the volcanoes Cerro Azul (CA) (the black square is the area in panel c), Sierra Negra (SN), Alcedo (A), Darwin (D), Wolf (W) and Ecuador (E) Digital elevation model and bathymetry in a) and b) from GeoMappApp. c) False colours (R=band 2; G=band 4; B=band 5) Landsat 7 image of Cerro Azul acquired on March 22nd,*

2009, showing the lava flows erupted in 2008. Triangles point areas where the eruptive fissures opened. The location of the lowest fissures of the first eruptive phase is poorly constrained. Image from https://earthexplorer.usgs.gov/ .

3 - Methods

3.1 InSAR data processing

To measure surface deformation before, during, and after the 2008 eruption at Cerro Azul, we used InSAR data. We formed 79 SAR images acquired by the European Space Agency's ENVISAT satellite (C-band, wavelength λ = 5.63 cm), 32 from an ascending track (T61) acquired between January 2006 and May 2010, and 47 from a descending track (T140) acquired between January 2003 to May 2010. We also formed 33 SAR images from the Japanese Space Agency's ALOS-1 satellite (L-band, wavelength λ=23.6 cm), 17 from an ascending track (T133) acquired between March 2007 and March 2011 and 16 from a descending track (T474) acquired between March 2007 and July 2010. We first generated interferograms with the InSAR Scientific Computing Environment (ISCE) software (Rosen et al., 2012). We removed topographic contributions to the interferometric phase using a 30 m-resolution DEM from the NASA Shuttle Radar Topography Mission (Farr et al., 2007). Then, to study the temporal evolution of surface displacements, we combined interferograms through a multi-temporal (MT) approach. In particular, we adopted the Small Baseline (SB) method using the StaMPS software (Hooper, 2008; Hooper et al., 2012) and selected the processing parameters that maximized the signal-to-noise ratio. In the supporting information Table S1 we report a list of the network of interferograms used for the SB analysis.

3.2 -Geodetic modelling

To interpret InSAR phase in terms of a geophysical model it is necessary to estimate the integer ambiguities in the phase (phase unwrapping). This is generally done prior to geophysical inversion, but any phase-unwrapping error will bias the resulting geophysical parameters. This would be the case for the ENVISAT data (Figure 2), where the 3-D unwrapping routine of StaMPS (Hooper, 2010a) cannot adequately unwrap data in the distal region where the radial eruptive fissures opened. This is evident when comparing displacements in the ENVISAT data near the eruptive fissures to those in the ALOS-1 interferogram in Figure 3d. To overcome this problem, we adopted a method to model the wrapped phase data directly, by estimating the integer ambiguities simultaneously with the geophysical parameters (Hooper, 2010b). We applied a Markov chain Monte Carlo method to build the posterior probability of the model, conditional on the data.

According to the Bayes' theorem the probability density function (PDF) of the vector of model parameters, **m**, given data vector, **d**, p(**m**|**d**), is (1)

$$p(\mathbf{m}|\mathbf{d}) = \frac{p(\boldsymbol{d}|\boldsymbol{m})p(\boldsymbol{m})}{\int_{-\infty}^{\infty} p(\boldsymbol{d}|\boldsymbol{m})p(\boldsymbol{m})\, d\boldsymbol{m}} \qquad (1)$$

Where p(**d**|**m**) is the likelihood function, p(**m**) is the prior distribution for the model parameters and the denominator is a normalising constant. For a given discrete inverse problem, data and model vectors are related by a function g plus error **e** (2):

$$\boldsymbol{d} = g(\boldsymbol{m}) + \boldsymbol{e} \qquad (2)$$

Thus, to calculate the likelihood function, the PDF of **e** is required. In the InSAR data, after the SB analysis with StaMPS, the errors are correlated, principally due to the contribution from variable atmospheric propagation delay (e.g. Hanssen et al., 1999). While the univariate PDF for a single wrapped phase value can be reasonably described by a wrapped normal distribution, the multivariate PDF for correlated wrapped data is difficult to calculate. We simplify the problem by calculating the wrapped phase differences for arcs between nearby coherent pixels. For coherent pixels, the contribution of uncorrelated noise to the arc phase is small (compared to a phase cycle) and reasonably approximated by a Gaussian distribution (Just & Bamler, 1994). As long as the pixels are nearby, the atmospheric contribution (and any other spatially-correlated error) to the arc phase is also small, and reasonably approximated by a Gaussian distribution. Thus, we approximate the joint PDF with a multivariate Gaussian distribution, with the likelihood function given by (3):

$$p(\boldsymbol{d}|\boldsymbol{m}) = (2\pi)^{-N/2}|\boldsymbol{Q}_d|^{-1/2} e^{-\frac{1}{2}\{W\{d-g(m)\}^T \boldsymbol{Q}_d^{-1} W\{d-g(m)\}\}} \qquad (3)$$

where W{.} is the wrapping operator, **d** now represents wrapped arc phase values, N is the dimension of **d**, and $\mathbf{Q}_d$ is the variance-covariance matrix for the errors in the arc phase values.

As InSAR data contain a large number of points, to reduce the computational time we subsample the data set prior to generating the network of arcs. For best results, it is essential to use an algorithm that maintains a good data point density in the deformed area. To this end, we use the adaptive quadtree sampling algorithm of GBIS (see Bagnardi & Hooper, 2018 and Decriem et al., 2010 for details) modified so that in each iteration, the mean wrapped phase for the all pixels in the polygon is found. If the wrapped difference between the mean and phase of any pixel is greater than a threshold value (default $\pi/2$), the polygon is subdivided into smaller polygons. This differs to the standard algorithm, which thresholds on standard deviation of phase values.

We generate the network of arcs using the Euclidean minimum spanning tree (EMST) method (Kruskal, 1956; Prim, 1957). This method minimises the total length of the arcs and avoids introducing unnecessary redundancy in the measurements; in other words, the model values for all arc phase values remain independent. The EMST leads to a network with every pixel connected to at

least one other and without isolated subsets (Figure 4c). We assume that the only correlation between arc phase errors is due to the contribution of spatially-uncorrelated noise to arcs connected by the same pixel. This means that we ignore any potential correlation due to the atmospheric contribution to the errors. This may not be negligible in areas of steep topography, where the hydrostatic tropospheric contribution to the arc phase errors could be significant and correlated between arcs, but is likely reasonable for our application to the gently sloping flanks of Cerro Azul.

We quantify the error structure of the data in the conventional way using the fitVariogram function of GBIS (Geodetic Bayesian Inversion Software; Bagnardi & Hooper, 2018) applied to an undeformed region of the interferogram, where phase unwrapping is typically not problematic. Once estimated using the fitVariogram function, we use the nugget, sill and range values to set up the variance-covariance matrix; we set the elements of the main diagonal (σ_{ii}^2) as: σ_{ii}^2=2*nugget+2*sill*[1-exp(-3*h/range)], where h is the length of the arc that connects each pair of pixels. We set the off-diagonal terms to the nugget value for arcs that share a pixel, and zero otherwise. Then we convert the variance and covariance values from m^2 to rad^2. In setting the variance-covariance matrix, we do not consider potential model errors, but they could be incorporated into the variance-covariance matrix using the approach of Duputel et al (2014).

Once we have defined the arcs and variance-covariance matrix for our quadtree-sampled data set, we estimate the posterior PDF of model parameters and uncertainties using the Bayesian approach implemented in the GBIS software (Bagnardi & Hooper, 2018), which uses a Markov chain Monte Carlo method, incorporating the Metropolis Hastings algorithm, and which we modified for working with the phase difference instead of unwrapped LOS displacements.

We tested this method on synthetic data. We modelled the sources using the rectangular dislocation (RD) model of Nikkhoo et al. (2017) and set the "plunge angle" $\theta = 0$ (see Nikkhoo et al., 2017 for further details), so that the two uppermost corners of the dike/inclined sill are at the same depth, as occurs in the Okada (1985) solution. For all modelling, we assumed an isotropic elastic half-space with Poisson's ratio of 0.25. To achieve convergence of the posterior PDF, we found it necessary to perform half a million iterations for the ENVISAT data and one million iterations for the ALOS-1 data.

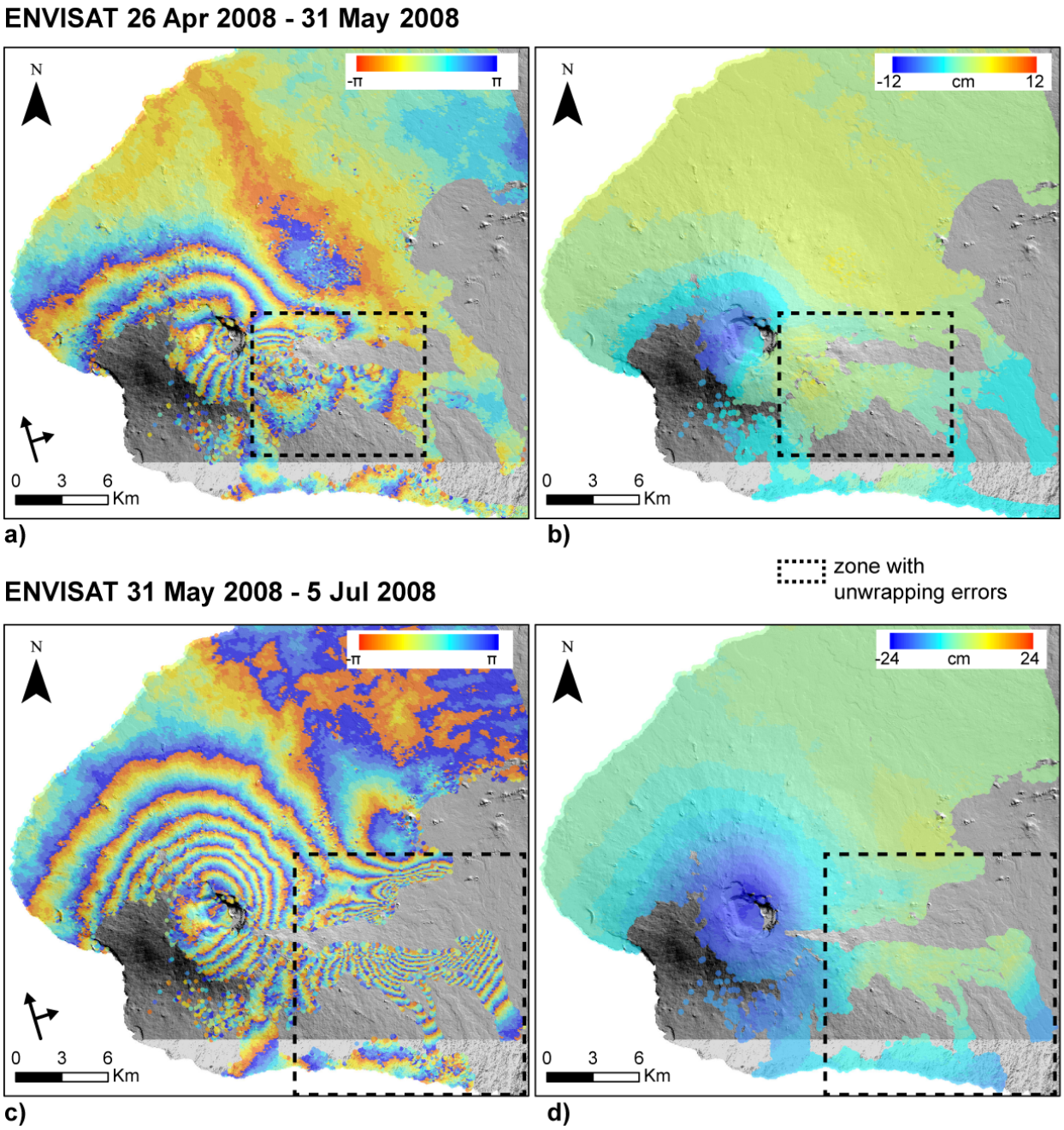

Figure 2 *Comparison between wrapped (a and c) and unwrapped (b and d) images from ENVISAT ascending track 61. Dashed rectangles highlight areas with an incorrect unwrapping, where the opening displacement across the eruptive fissure is not visible (compare to ALOS results in Fig. 4d). In a and c each fringe (full colour cycle) represents 2π radians of phase change corresponding to 2.8 cm of range change in the line-of-sight direction.*

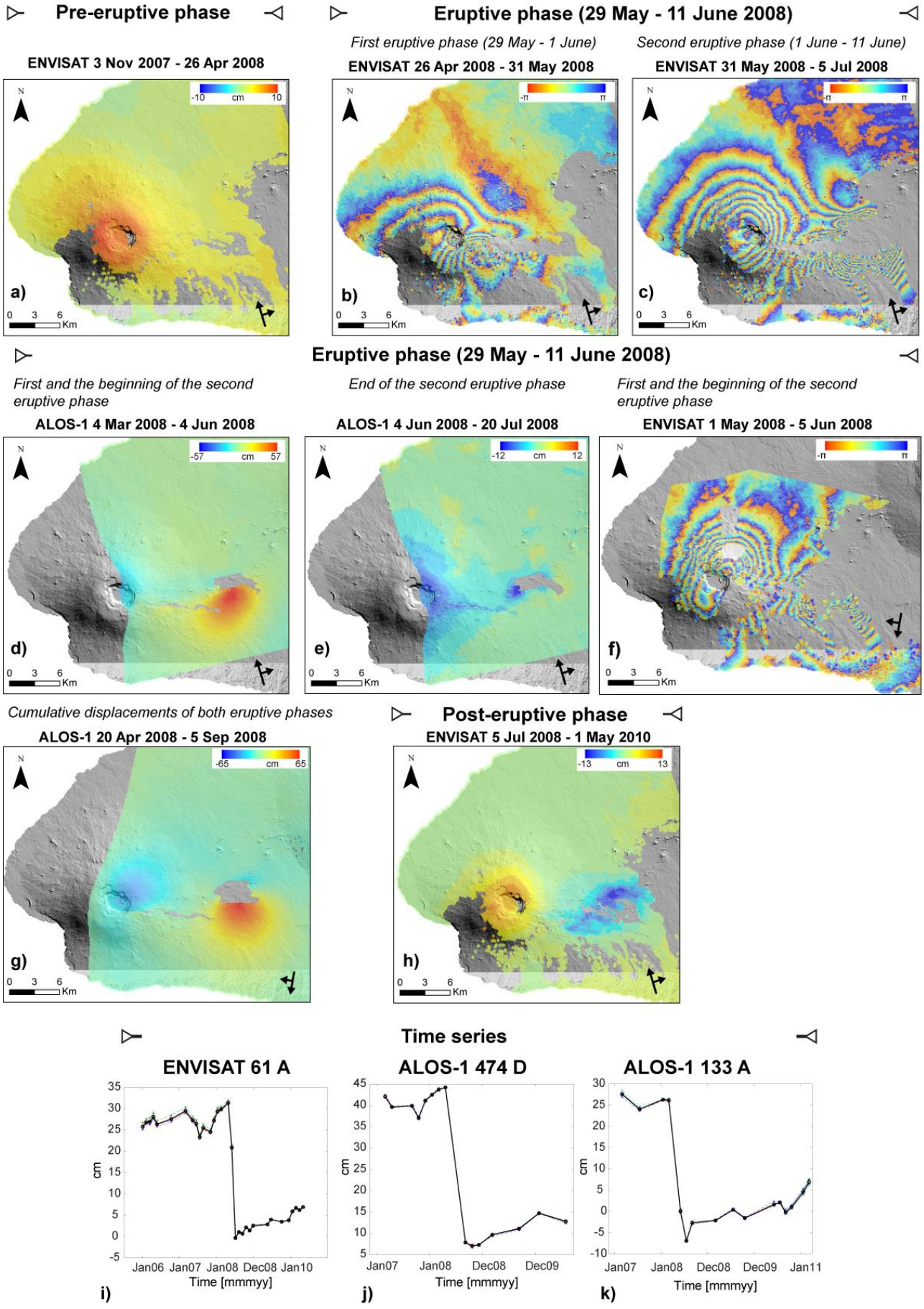
Pre-eruptive phase
Eruptive phase (29 May - 11 June 2008)
First eruptive phase (29 May - 1 June)
Second eruptive phase (1 June - 11 June)
ENVISAT 3 Nov 2007 - 26 Apr 2008
ENVISAT 26 Apr 2008 - 31 May 2008
ENVISAT 31 May 2008 - 5 Jul 2008
-10 cm 10
-π π
a)
b)
c)
0 3 6 Km
Eruptive phase (29 May - 11 June 2008)
First and the beginning of the second eruptive phase
End of the second eruptive phase
First and the beginning of the second eruptive phase
ALOS-1 4 Mar 2008 - 4 Jun 2008
ALOS-1 4 Jun 2008 - 20 Jul 2008
ENVISAT 1 May 2008 - 5 Jun 2008
-57 cm 57
-12 cm 12
d)
e)
f)
Cumulative displacements of both eruptive phases
Post-eruptive phase
ALOS-1 20 Apr 2008 - 5 Sep 2008
ENVISAT 5 Jul 2008 - 1 May 2010
-65 cm 65
-13 cm 13
g)
h)
Time series
ENVISAT 61 A
ALOS-1 474 D
ALOS-1 133 A
cm
Jan06 Jan07 Jan08 Dec08 Jan10
Jan07 Jan08 Dec08 Dec09
Jan07 Jan08 Dec08 Dec09 Jan11
Time [mmmyy]
i)
j)
k)

Figure 3 *Time-series results. a-c) ENVISAT LOS displacement map for ascending orbit 61 during a) pre-eruption (November 2007 – April 2008); b) first eruptive phase (April 2008 – May 2008); c) second eruptive phase (May 2008 – July 2008). d-e) ALOS-1 LOS displacement map for ascending orbit 133, during the eruption f) ENVISAT LOS displacement map for descending track 140. g) ALOS-1 LOS displacement map for descending track 474 (April-September, 2008). h) ENVISAT LOS displacement map for ascending track 61 during the post-eruptive period (July 2008 – May 2010.). i-k) Time series of the caldera area. In a, d-e and g-h data are unwrapped, and spatially-corrected look-angle errors (including orbital ramps) are removed. In b-c and f data are wrapped and each fringe (full colour cycle) represents 2π radians of phase change corresponding to 2.8 cm of range change in the line-of-sight direction. All the displacement maps are overlaid onto shaded relief map from WorldDEM data.*

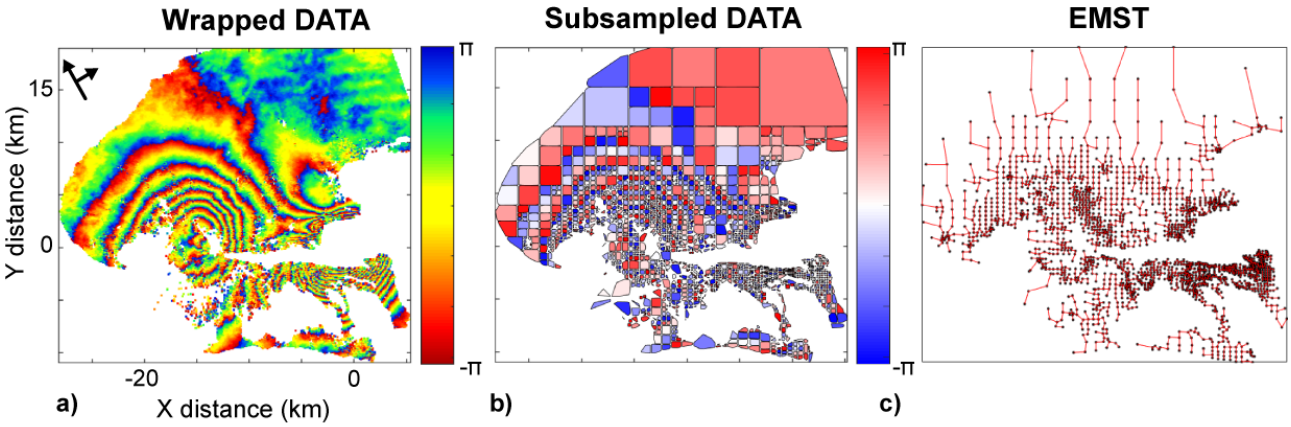

Figure 4 *a) Wrapped InSAR data from ENVISAT ascending track 61, acquired from May 31st to July 5th 2008. Each fringe (full colour cycle) represents 2π radians of phase change corresponding to 2.8 cm of range change in the line-of-sight direction. b) Downsampled data using our modified quadtree function. c) The arcs formed by the Euclidean minimum spanning tree (EMST).*

4 – Data description

4.1 - Pre-eruption

InSAR time series of ENVISAT ascending and ALOS-1 descending data record a pre-eruptive uplift of ~10-12 cm, peaking immediately outside the western portion of the caldera, and occurring from October 2007 to April 2008, before the eruption started on May 29th (Figure 3a, i-j). The inflation slows down in the months just before the eruption (Figure 3i-j). The temporal resolution of the InSAR data does not shed light on whether this uplift continued until just prior to the eruption or not.

4.2 - Eruption

ENVISAT ascending data allow us to separate the deformation of the two eruptive phases. Until May 31st (end of the pre-eruptive phase and the first eruptive phase), these data record a subsidence of ~12 cm in the western sector of the caldera and in the west and south-western sectors of the upper flank of the volcano, peaking in the same area of the maximum uplift of the pre-eruptive period (Figure 3b). A LOS displacemnts of about the same magnitude, but opposite in the sign, occurred near the active eruptive fissures, placed on the upper east flank (Figure 3b). After May 31st (second eruptive phase and the beginning of the post-eruptive phase; Figure 3 c-g), there is an eastward shift of the subsidence on the volcano summit, with another 24 cm of subsidence peaking in the caldera area (Figure 3c-e). At the same time, the deformation on the east flank migrated from the summit vents, which ceased their activity on June 1st, to the distal radial fissure at the base of the eastern flank, which started its activity on June 3rd. Most of this deformation (~60 cm) occurred by June 4th (Figure 3d-f), even if the eruptive fissure remained active until June 11th. Conversely to ENVISAT data, ALOS-1 descending data (Figure 3g) maintain good coherence on the southern flank of Cerro Azul, even though they are less well sampled temporally, and show a lower amount of subsidence (~15 cm) with respect to the proximal area (~38 cm).

4.3 - Post eruption

After the eruption, from July 2008 to March 2011 there was a new uplift of the caldera area, characterized by non-uniform rates (Figure 3h-k). The temporal resolution of our InSAR data does not allow us to better constrain the onset of uplift.

5 – Test on the synthetic and natural data.

To test the validity of the method described in section 3.2, we performed a test on synthetic data. We used a data coverage similar to that of ENVISAT data in the area of the dike (Figure 2c; 5). We calculated the phase due to displacements caused by a RD dike source (model parameters reported in Figure 6 and Table S2), assuming a wavelength of 0.0563 m, an incidence angle of 25.71° and a heading angle of 12.3992° (Figure 5a). We added a realistic atmospheric phase screen error using an isotropic two-dimensional fractal surface with a power law behaviour (Hanssen, 2001; Figure 5b) and a random noise (Figure 5c) to simulate non-correlated errors. Then, we inverted the synthetic data using both the method described in Section 3.2 and GBIS and we compered the results (Figure 6; S1; Table S2). In both cases the actual model parameters fall within the 95% bounds of the posterior PFDs (Figure 6), confirming the validity of the method. In Figure S2 and S3, we report the trace plot, obtained with the new method and with GBIS, in which is possible to evaluate the convergence of the Markov chain. In both cases, the number of early samples that strongly depend on the choice of the starting value (the so-called "burn-in" period) is similar. This is due also to the fact that the new method uses the same MCMC algorithm of GBIS, with the only difference of inverting for the wrapped phase differences among nearby pixels rather than the LOS displacements.

In addition, we performed also a test on natural data to compare results obtained with the new method to those of GBIS, in which we jointly inverted the deformations recorded by the ALOS-1 ascending and descending data on the east flank of Cerro Azul (Figure 3 d, g). Results obtained with the two methods are consistent each other (Figure S4, S5 and Table S3), supporting again the validity of the method proposed in section 3.2.

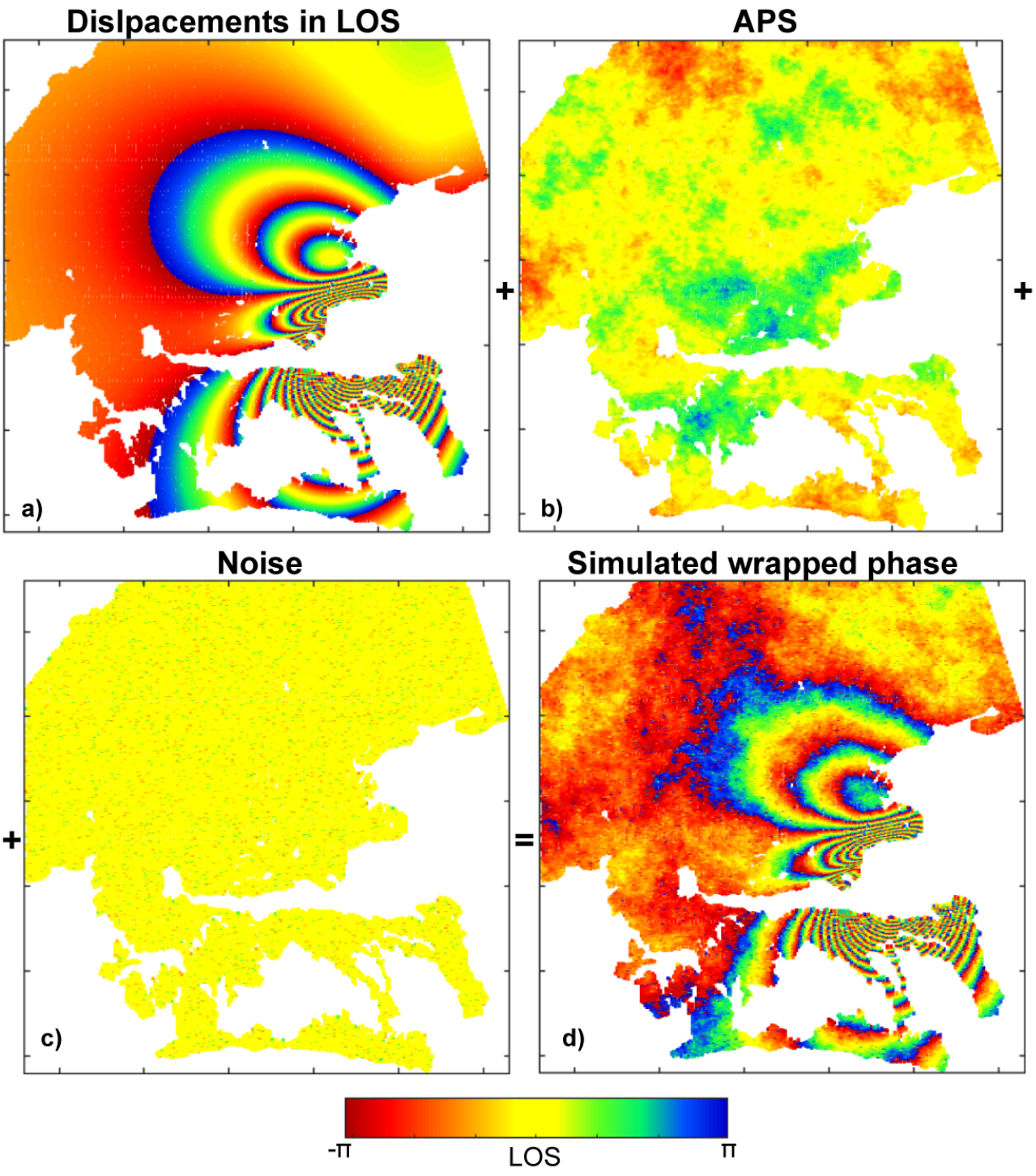

Figure 5*. a) Simulated InSAR LOS displacements. Each fringe (full colour cycle) represents 2π radians of phase change corresponding to 2.8 cm of range change in the LOS direction. b) Simulated atmospheric phase screen error (APS). c) Random error. d) Final synthetic data.*

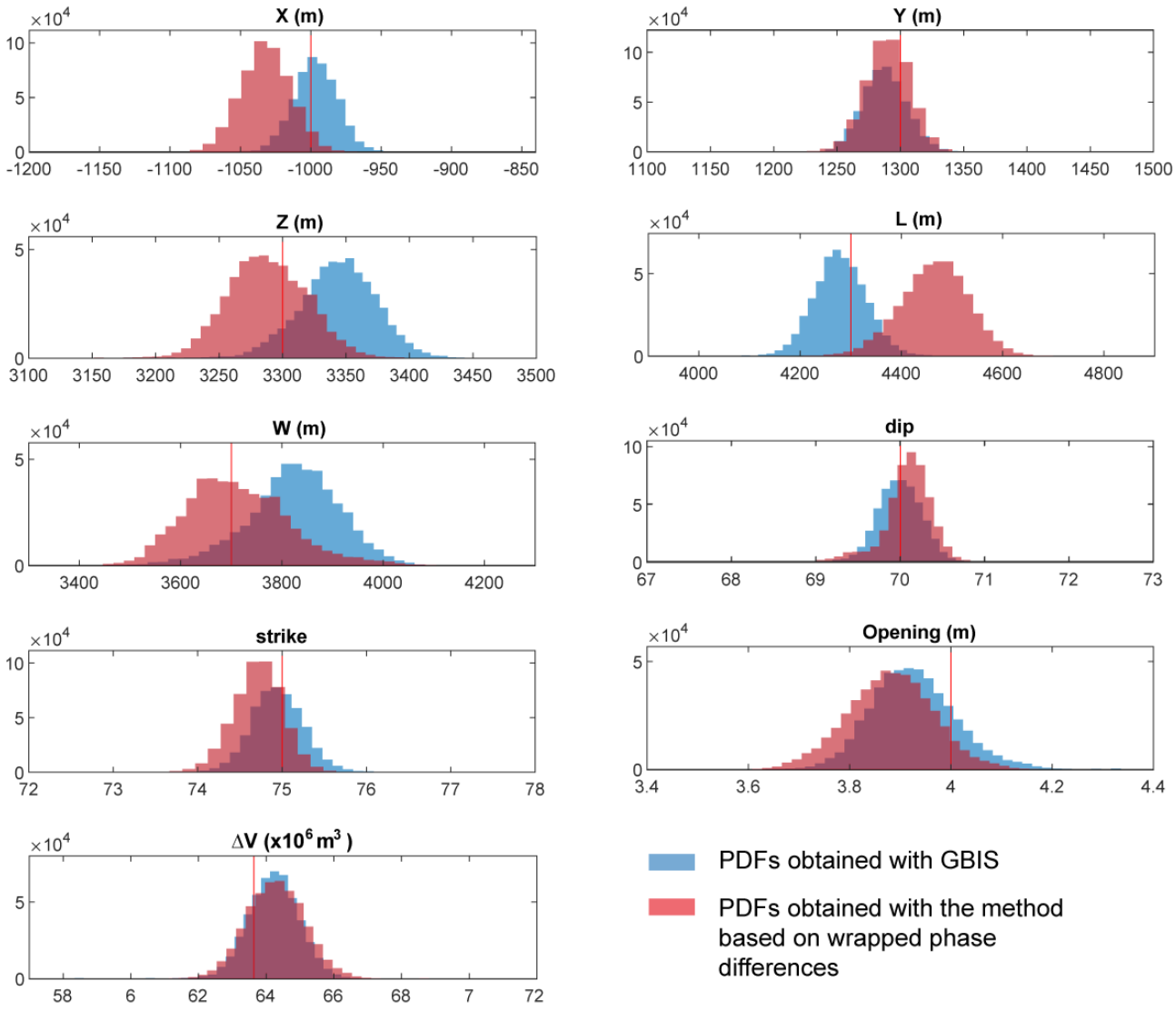

Figure 6 *Posterior probability density distribution (PDFs) for each individual model parameter from the inversion of the synthetic data usind both the new method and GBIS. The red lines representing the actual simulated values (see Table S2).*

6- Results of the geodetic modelling

6.1 - Pre eruptive phase

We modelled the pre-eruptive uplift occurred at Cerro Azul recorded by ALOS-1 descending track data (October 19th 2007 – April 20th 2008) for possible magmatic sources using the standard GBIS software applied to unwrapped interferogram. Best results were obtained using a Mogi source (Figure 7a-c, Table 1). The Bayesian analysis converged to an inflation point, placed at ~5 km below the north caldera rim, with a volume change (ΔV)= 12.6±3.7 x10^{-3} km^3 and a corresponding injection rate of 2.5±0.7 x10^{-2} km^3/year.

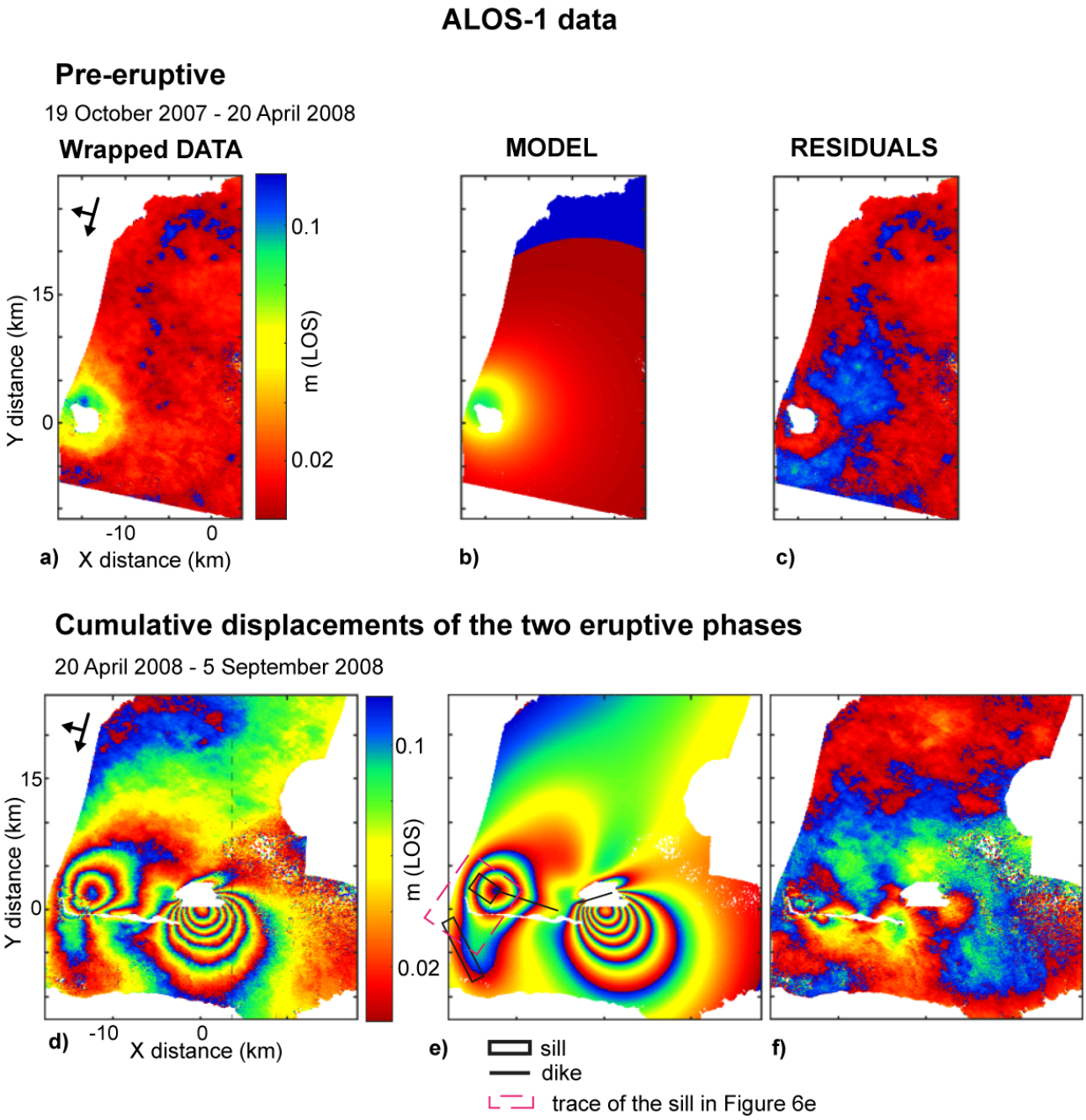

Figure 7 *a and d) Wrapped ALOS-1 LOS displacements for descending track 474. Each fringe (full colour cycle) represents 11.8 cm of LOS displacement. b) Predicted displacements for the Mogi model and e) for the four dislocation model using the maximum a posteriori probability solutions (MAP). c and f) Related residuals. The surface projections of the dislocations are shown on panels e). Dikes appear as lines as we drew only the projection of the line passing for the centre of the RD and parallel to the surface. The dotted grey lines in panel e delimits the area of the panels a to c. The local origin for all panels is 91°26'W and 0°93'S.*

Table 1 *Results of the Bayesian analysis for the ALOS-1 descending track data.*

ALOS-1 data (descending track 474)										
Pre-eruptive (19 October 2007- 20 April 2008)										
					Mogi source					
		X (m)	**Y (m)**	**Depth (m)**					**ΔV (x10^6 m^3)**	
Optimal		-16962	2202	4905					11.66	
	2.50%	-17472	1828	4364					8.94	
	97.50%	-16602	2560	5815					16.29	
Prior lower		-20000	-5000	4000					0.01	
Prior upper		-10000	5000	8000					1000	
Eruption (20 April-5 September 2008)										
					RD dike (first event)					
	X (m)[a]	**Y (m)[a]**	**Z (m)[a]**	**L (m)[a]**	**W (m)[a]**	**θ[a]**	**Dip[a]**	**Strike[a]**	**Op.[a] (m)**	**ΔV (x10^6 m^3)**
Optimal	-8747	880	3252	7570	1018	0	84	108	1.28	
2.5%	-8747	880	3252	7570	1018	0	84	108	1.28	
97.5%	-8747	880	3252	7570	1018	0	84	108	1.28	
Prior lower	-8747	880	3252	7570	1018	0	84	108	1.28	
Prior upper	-8747	880	3252	7570	1018	0	84	108	1.28	
					RD dike (second event)					
	X (m)	**Y (m)**	**Z (m)**	**L (m)**	**W (m)**	**θ[a]**	**Dip**	**Strike**	**Op. (m)**	**ΔV (x10^6 m^3)**
Optimal	-990	1205	3538	4051	4829	0	75	73	3.53	69.1
2.5%	-1051	1103	3268	3960	4091	0	73	72	3.33	61.2
97.5%	-945	1291	3674	4226	5103	0	76	74	3.79	73.2
Prior lower	-10000	-10000	2700	1000	1000	0	40	1	0	
Prior upper	10000	10000	4000	6000	5200	0	85	90	5	
					Northern RD deflated sill					
	X (m)	**Y (m)**	**Z (m)[a]**	**L (m)**	**W (m)**	**θ[a]**	**Dip[a]**	**Strike[a]**	**Op. (m)**	**ΔV (x10^6 m^3)**
Optimal	-13523	2304	5200	2025	3007	0	0	35	-4.47	-27.2
2.5%	-13679	2169	5200	2006	3004	0	0	35	-4.49	-29
97.5%	-13383	2454	5200	2757	3511	0	0	35	-3.15	-25.5
Prior lower	-20000	-10	5200	2000	3000	0	0	35	-5.5	
Prior upper	-10000	4000	5200	10000	8000	0	0	35	0	
					Southern RD deflated sill					
	X (m)	**Y (m)**	**Z (m)[a]**	**L (m)**	**W (m)**	**θ[a]**	**Dip[a]**	**Strike**	**Op. (m)**	**ΔV (x10^6 m^3)**
Optimal	-16041	-4611	5200	1433	7473	0	0	63	-0.97	-10.38
2.5%	-16487	-5737	5200	514	6295	0	0	47	-2.96	-13.3
97.5%	-15297	-3875	5200	2390	7786	0	0	77	-0.6	-7.8
Prior lower	-18000	-8000	5200	500	6000	0	0	10	-3.5	
Prior upper	-13500	-1000	5200	3000	7800	0	0	89	0	

*Notes. X and Y are the local coordinates of the Mogi source and of the centre of the RD source with respect to a local origin (see Figure 7) at 91° 26' W and 0° 93' S. Depth is referred to the centre of the RD and is with respect to the surface (positive downward). ΔV is the volume change (for the RD source it is calculated with the formula ΔV=L*W*Op). θ is the angle between the RD upper edge and the intersection of the RD plane with the free surface. L and W are the length and width of the RD source. Op. is the opening. (see Nikkhoo et al., 2017 for a better explanation of the RD parameters). Optimal is the maximum a posteriori probability (MAP) solution. 2.50% and 97.50% are the*

percentile values describing the credible interval. Prior Lower and Upper are the bounds of the prior distribution used for the inversion. [a] Fixed parameter.

6.2 - Eruptive phase

ENVISAT ascending data are the only that allow us to distinguish the deformation of the first eruptive phase from that of the second phase. Thus, we use these data to constrain the sources of deformation of the two phases. As we were not able to reliably unwrap these interferograms, we used the wrapped inversion method described in Methods.

6.2.1 - April 26th – May 31st (end of the pre-eruptive phase and first eruptive phase)

We modelled deformation during the first phase using a combination of two rectangular dislocation sources (Figure 8a-c; Table 2). The first dislocation converged to a 9 km x 1 km horizontal sill, with the major axis oriented northeast-southwest, placed at ~5.2 km below the western sector of the caldera and the flank of the volcano. The modelled sill shows a contraction of 1.1±0.2 m, with a corresponding volume change of $\Delta V = -11.2 \pm 0.6 \times 10^{-3}$ km^3. As for the second dislocation, the Bayesian analysis converged to an east-southeast oriented sub-vertical dike, whose top edge is placed at ~2.8 km below the eastern flank, with an opening of 1.1±0.3 m. The corresponding ΔV is $9.9 \pm 0.5 \times 10^{-3}$ km^3. This dike explains most of the deformation recorded on the east flank by the InSAR data in this period, but it is placed ~2 km to the north of the active eruptive fissures of the first phase and its geometry (southward dipping) and position do not seem compatible with the location and orientation of the eruptive fissures. There is no obvious geodetic signal associated with these eruptive fissures, and we infer that it is probably hidden by that of the radial dike, which dominates the deformation field. The small residuals near the summit eruptive vents, which cannot be explained by our model, may be the remains of the geodetic signal related to these eruptions.

6.2.2 - May 31st – July 5th (second eruptive phase and the beginning of the post-eruptive phase)

To model the second eruptive phase, we again used two rectangular dislocation sources (Figure 8d-f; Table 2). The Bayesian analysis results in a larger 9 x 7 km deflating sill, placed below the caldera. The corresponding volume loss is $25 \pm 2.2 \times 10^{-3}$ km^3. To reduce the number of variables and to better constrain the opening and the length and width of this sill, we fixed the sill depth using the depth of the sill obtained from the inversion of the data of the first eruptive phase. The opening of a N80° south-southeast-dipping dike (dip angle=68°), whose top edge is at ~0.9 km below the radial distal eruptive fissure, explains the distal deformation. The volume change of this dike is $57.4 \pm 2.6 \times 10^{-3}$ km^3. Most of this volume probably was emplaced by June 4th, as ALOS-1 ascending data (Figure 3d-

e) show how most of the related deformation occurred by June 4th. This radial dike lies on the continuation of the radial dike of the first phase, even though with an anticlockwise rotation of about 28° and a decrease in the dip angle (68° compared to 84°).

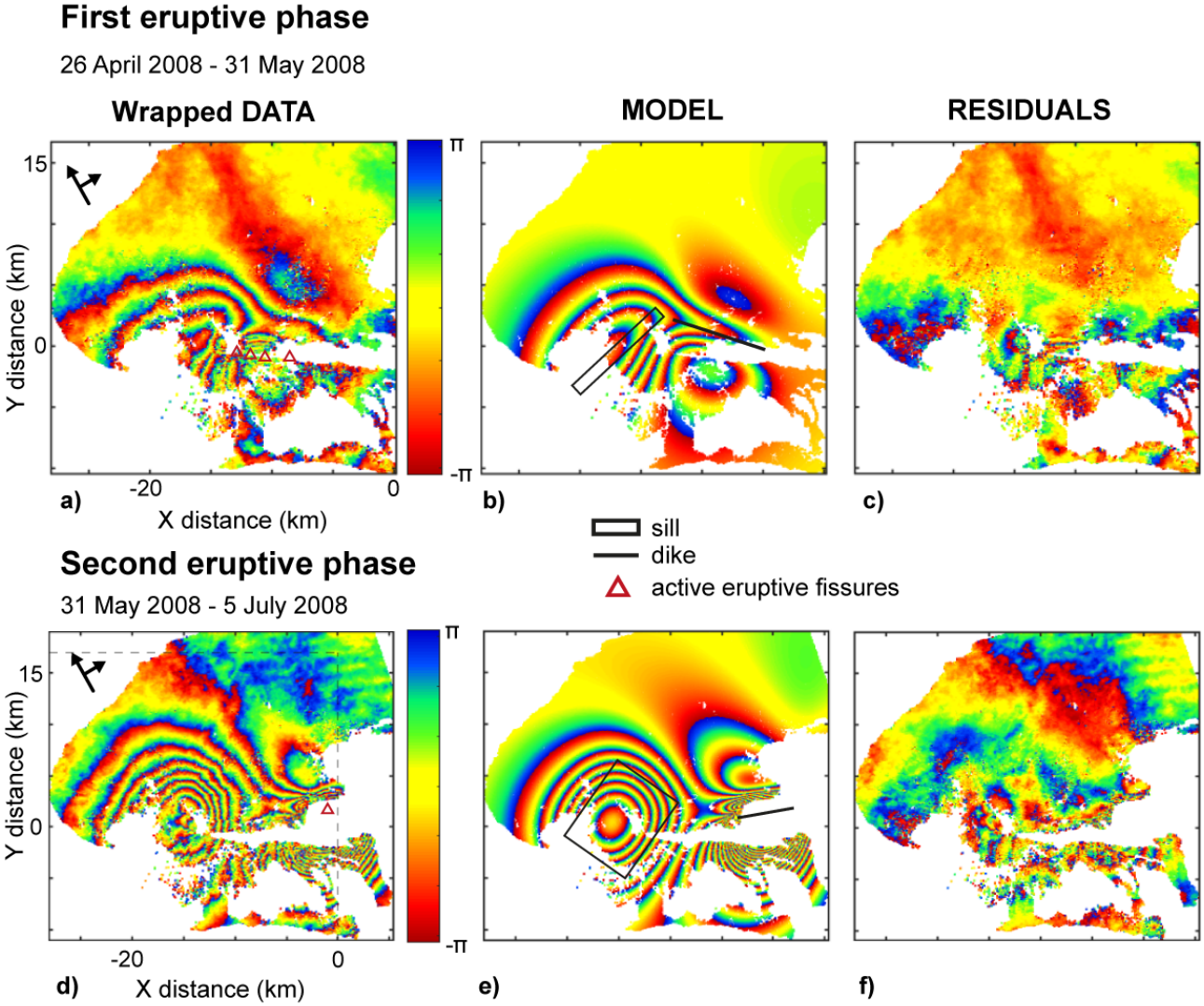

***Figure 8**. a) Wrapped ENVISAT phase for ascending track 61 for the first eruptive period and d) for the second eruptive period. Each fringe (full colour cycle) represents 2π radians of phase change corresponding to 2.8 cm of range change in the LOS direction. b and e) Predicted displacements for the respective two rectangular dislocation model using the MAP solutions. c and f) Related residuals. The surface projections of the dislocations are shown on panels b) and e). Dikes appear as lines as we drew only the projection of line passing for the centre of the RD and parallel to the surface. The local origin for all panels is 91°26'W, 0°93'S. The dotted grey lines in panel d delimits the area of the panels a to c.*

Table 2 *Results of the Bayesian analysis for the inversion of ENVISAT ascending track data.*

E61A April-May 2008 (first eruptive phase)

RD radial dike

	X (m)	Y (m)	Z (m)	L (m)	W (m)	θ[a]	Dip	Strike	Op. (m)	ΔV (x10^6 m^3)
Optimal	-8747	881	3252	7569	1019	0	84	108	1.29	9.9
2.50%	-8942	776	3182	7005	1001	0	83	108	0.79	9.4
97.50%	-8603	925	3325	7895	1683	0	85	110	1.41	10.4
Prior lower	-12500	100	2100	1000	1000	0	40	80	0	
Prior upper	-5000	5000	5000	10000	4000	0	89	270	5	

RD deflating sill

	X (m)	Y (m)	Z (m)	L (m)	W (m)	θ[a]	Dip	Strike	Op. (m)	ΔV (x10^6 m^3)
Optimal	-16964	-458	5188	9365	1001	0	0	43	-1.23	-11.5
2.50%	-17053	-517	5026	8695	1003	0	0	41	-1.24	-11.8
97.50%	-16864	-130	5319	9727	1415	0	2	49	-0.88	-10.6
Prior lower	-21000	-5000	3200	2000	1000	0	0	1	-5	
Prior upper	-10000	5000	6000	12000	12000	0	30	360	0	

E 61A May-July 2008 (second eruptive phase)

RD radial dike

	X (m)	Y (m)	Z (m)	L (m)	W (m)	θ[a]	Dip	Strike	Op. (m)	ΔV (x10^6 m^3)
Optimal	-593	1234	2985	5564	4529	0	68	80	2.25	56.7
2.50%	-632	1161	2915	5441	4349	0	68	79	2.17	54.8
97.50%	-512	1268	3139	5749	4878	0	69	81	2.31	61
Prior lower	-6000	-2000	2800	1000	1000	0	50	1	0	
Prior upper	5000	4000	5000	5800	5200	0	86	89	5	

RD deflating sill

	X (m)	Y (m)	Z (m)[a]	L (m)	W (m)	θ[a]	Dip	Strike	Op. (m)	ΔV (x10^6 m^3)
Optimal	-14889	603	5200	9009	7231	0	0	35	-0.39	-25.4
2.50%	-15069	395	5200	8271	6428	0	-3	24	-0.43	-27.2
97.50%	-14714	953	5200	9470	7813	0	5	48	-0.37	-22.8
Prior lower	-21000	-5000	5200	1000	1000	0	-30	1	-5	
Prior upper	-10000	5000	5200	14000	14000	0	30	90	0	

*Notes. X and Y are the local coordinates of the centre of the RD with respect to the local origin (see Figure 8a and d) at 91° 26' W and 0° 93' S. Z is the depth of the centre of the RD with respect to the surface (positive downward). θ is the angle between the RD upper edge and the intersection of the RD plane with the free surface. L and W are the length and width, respectively. Op. is the opening. ΔV is the volume change calculated with the formula ΔV=L*W*Op.*
Optimal is the MAP solution. 2.50% and 97.50% are the lower and upper bounds of the 95% confidence interval. Prior lower and upper are the bounds of the prior distribution used for the inversion. [a] *Parameter held fixed.*

6.2.3 - ALOS-1 data: April 20th – September 5th (cumulative displacements of the two eruptive phases)

ALOS-1 descending track data are less temporally constrained than the ENVISAT data, recording the cumulative deformation pattern of the 2008 eruption, but maintain good coherence on the southern

flank. Therefore, we inverted this data using GBIS software. To allow for multiple different sources as indicated by the ENVISAT results, we inverted for four rectangular dislocations (Figure 7d-f; Table 1).

We modelled the deformation at the base of the east flank of Cerro Azul with a dike. We set uninformative prior PDFs for each model parameter of this dike (Table 1). As deformation from the radial dike in the first eruptive phase is masked by the subsequent deformation, we fixed the parameters for it to the MAP solution from the ENVISAT results. We allowed for only one sill to fit the deformation beneath the caldera during both eruptive phases in the ENVISAT data, as the locations are the same within error. We also added a second sill beneath the south flank of Cerro Azul, an area not covered by the ENVISAT data, as there is deformation visible there in the ALOS data.

The results for the unconstrained dike converged to a south-southeast-dipping dike (dip angle ~75°), with a ΔV =67.2±6 x10^{-3} km^3, which is about 22% more than estimated from the ENVISAT data inversion. However, this discrepancy is explained by the fact that we inverted the only ALOS-1 descending track, which records in that area a higher magnitude of the LOS displacements than the ascending tracks of ALOS-1 and ENVISAT. Results from the jointly inversion of the ALOS-1 ascending and descending track (Figure S2; Table S3), in fact, are consistent with the volume estimated from the inversion of ENVISAT data.

The two sills largely overlap the sill resulting from the modelling of the second eruptive phase from the inversion of ENVISAT data (Figure 8e). However, the sill on the southern flank shows less contraction (-1.8±1.2 m) with respect to the sill below the caldera (-3.8±0.7 m). The total volume lost by the two sills is approximately equal to the sum of the volume loss from the inversion of ENVISAT data during the two eruptive phases (Table 1 and 2). (-37.8±4.5 x10^{-3} km^3 with respect to -36.2±2.8 x10^{-3} km^3 of ENVISAT data).

6.2.4 - Joint inversion of ALOS-1 and ENVISAT data

Finally, we jointly inverted the descending data of ALOS-1 and the total deformation recorded by ENVISAT ascending track, to better constrain the deformation source parameters, allowing for two dikes and two sills (Figure 9). In this inversion we combined the use of unwrapped data for ALOS-1 and wrapped data for ENVISAT. For the radial dike of the first eruptive phase, we again fixed the geometry using the MAP solution from the inversion of ENVISAT data for the first eruptive phase, but now inverting for the opening.

Results of the Bayesian analysis (Table 3) converge to solutions similar to the other models. As for the radial dike of the first event, we found an opening of 1.4±0.1 m with a ΔV of 10.7±0.8 x10^{-3} km^3,

similar to the values of 8.3±2.2 x10^{-3} from the inversion of ENVISAT ascending track data alone (Table 2). A south-southeast dipping dike, with ΔV= 57±2.1 x10^{-3} km^3, explains the deformation outside the eastern flank of Cerro Azul related to the second eruptive phase. This solution is similar to those obtained from the single-track inversion of ENVISAT and ALOS-1 data with two different method. Therefore, it suggests that the differences in the posterior marginal PDF of some parameters of this dike obtained from the single track inversion of ENVISAT and ALOS-1 data were related only to the different geometry of acquisition of the two satellites. Deflation beneath the caldera is fit by two sills, the northern one deflating by -29.5±1.6 x10^{-3} km^3 and the other deflating by -8.5±9.5 x10^{-3} km^3. The total volume lost by the system is comparable to the results from the inversions of the individual tracks. However, in the area near the caldera, residuals are larger than those from the single track inversions (Figure 9) due to the requirement to also fit the ALOS-1 data.

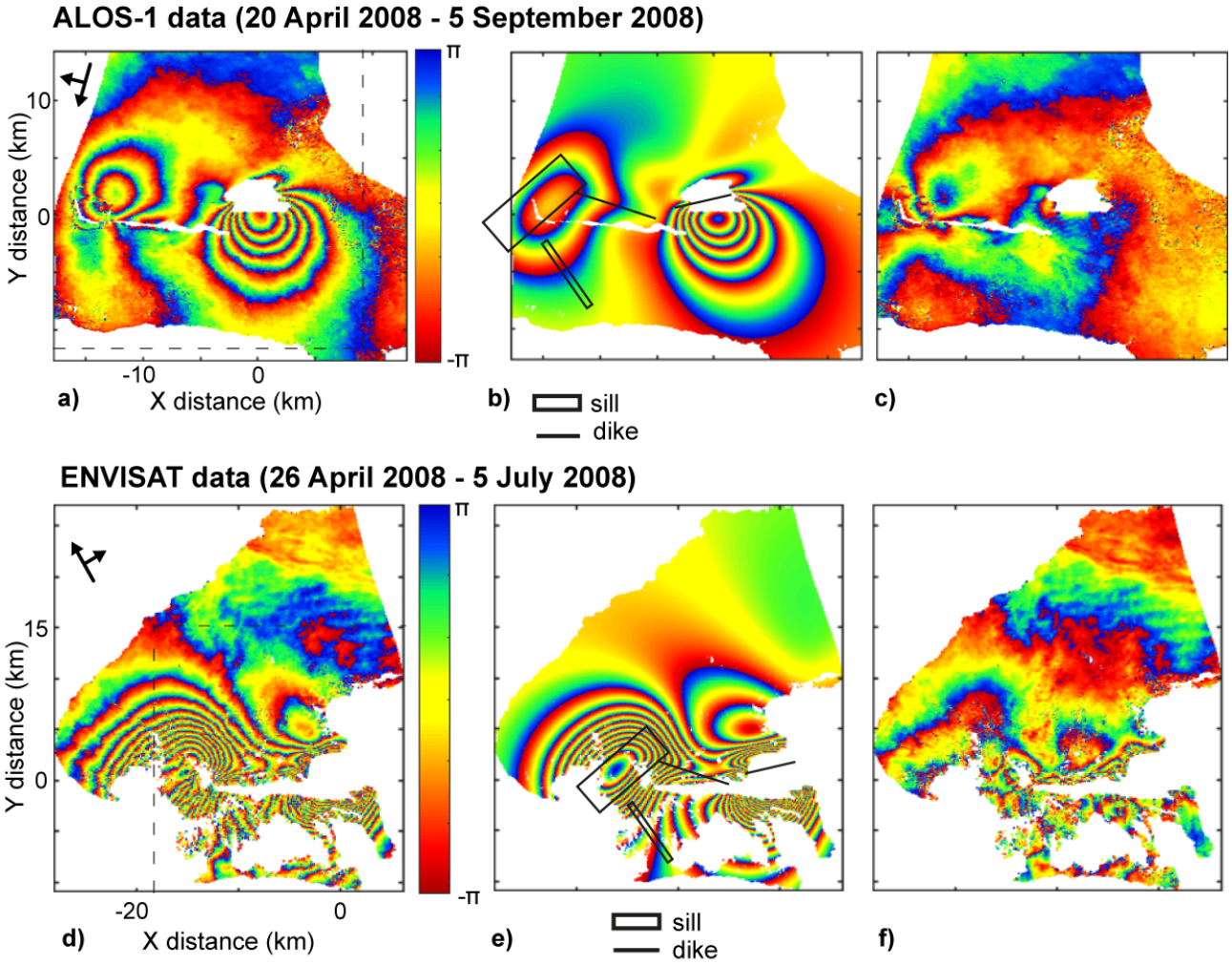

Figure 9*. a) Wrapped ALOS-1 phase for descending track 474. Each fringe (full colour cycle) represents 2π radians of phase change corresponding to 11.8 cm of range change in the LOS*

direction. d) Wrapped ENVISAT LOS displacements for ascending track 61. Each fringe (full colour cycle) represents 2π radians of phase change corresponding to 2.8 cm of range change in the LOS direction. b and e) Predicted displacements for the respective four rectangular dislocation model using the MAP solutions. c and f) Related residuals. The surface projections of the dislocations are shown on panels b) and e). Dikes appear as lines as we drew only the projection of the line passing for the centre of the RD and parallel to the free surface. The dotted grey lines in panels a) and d) delimit the same area. The local origin for all panels is 91°26'W and 0°93'S.

Table 3 *Results of the Bayesian analysis for the jointly inversion of ALOS-1 descending track and ENVISAT ascending track data.*

					RD dike (first event)					
	X (m)[a]	**Y (m)[a]**	**Z (m)[a]**	**L (m)[a]**	**W (m)[a]**	**θ[a]**	**Dip[a]**	**Strike[a]**	**Op. (m)**	**ΔV (x10^6 m^3)**
Optimal	-8750	880	3250	7500	1020	0	84	108	1.47	11.2
2.50%	-8750	880	3250	7500	1020	0	84	108	1.29	9.9
97.50%	-8750	880	3250	7500	1020	0	84	108	1.5	11.5
Lower	-8750	880	3250	7500	1020	0	84	108	0.5	
Upper	-8750	880	3250	7500	1020	0	84	108	1.5	
					RD dike (second event)					
	X (m)	**Y (m)**	**Z (m)**	**L (m)**	**W (m)**	**θ[a]**	**dip**	**strike**	**Op. (m)**	**ΔV (x10^6 m^3)**
Optimal	-891	1166	3158	5073	3540	0	69	77	3.19	57.3
2.50%	-929	1119	3093	4945	3336	0	68	76	3.01	55
97.50%	-848	1290	3231	5190	3751	0	70	78	3.58	59.1
Lower	-6000	-2000	2800	1000	1000	0	50	1	0	
Upper	5000	4000	5000	5750	5300	0	87	90	5	
					Northern **RD deflated sill**					
	X (m)	**Y (m)**	**Z (m)[a]**	**L (m)**	**W (m)**	**θ[a]**	**dip[a]**	**strike**	**Op. (m)**	**ΔV (x10^6 m^3)**
Optimal	-15533	1035	5200	9019	3371	0	0	49	-0.95	-28.9
2.50%	-15952	786	5200	8598	3030	0	0	47	-1.05	-31.1
97.50%	-15416	1140	5200	9962	3941	0	0	51	-0.81	-27.9
Lower	-20000	-100	5200	2000	3000	0	0	1	-5	
Upper	-11000	3000	5200	10000	10000	0	0	80	0	
					Southern RD deflated sill					
	X (m)	**Y (m)**	**Z (m)[a]**	**L (m)**	**W (m)**	**θ[a]**	**Dip[a]**	**strike**	**Op. (m)**	**ΔV (x10^6 m^3)**
Optimal	-12827	-5162	5200	557	6874	0	0	55	-0.27	-1.03
2.50%	-15536	-6868	5200	529	6035	0	0	23	-0.34	-1.8
97.50%	-12805	-3134	5200	2079	7723	0	0	84	-0.03	-0.1
Lower	-17900	-8000	5200	500	6000	0	0	1	-4	
Upper	-12800	-2000	5200	3000	7800	0	0	90	0	

Notes. X and Y are the local coordinates of the centre of the RD source with respect to the local origin (see Figure 9a and d) at 91° 26' W and 0° 93' S. Z is the depth of the centre of the RD with respect to the surface (positive downward). θ is the angle between the RD upper edge and the intersection of

*the RD plane with the free surface. L and W are the length and width, respectively. Op. is the opening (see Nikkhoo et al., 2017 for a better explanation of all these parameters). ΔV is the volume change calculated with the formula ΔV=L*W*Op.*
Optimal is the MAP solution. 2.50% and 97.50% are the lower and upper bounds of the 95% confidence intervals. Prior lower and upper are the bounds of the prior distribution used for the inversion. [a] *Parameter held fixed.*

7 - Discussion

The use of InSAR data and their geodetic modelling allow us to reconstruct the evolution of the 2008 eruption at Cerro Azul. Pre-eruptive uplift of the caldera area during the seven months before the eruption (Figure 7) seems related to the supply of new magma and is modelled with the inflation of a point source at ~5 km below the caldera. On May 29th, the first eruptive phase started. During this phase, the lateral propagation of a sub-vertical dike triggered the deformation on the eastern flank, while the observed subsidence is modelled with the deflation of a sill, placed below the western portion of the caldera and the upper western flank (Figure 8b). The depth of this sill (~5 km below the surface) is consistent with the depth of both the modelled pre-eruptive point source and the magmatic reservoir of Cerro Azul, deeper and less developed than the other western Galápagos calderas (Geist et al., 2014). Therefore, the pre-eruptive uplift and the co-eruptive subsidence are probably related to the inflation/deflation of the magmatic reservoir, modelled with different simple sources. This latter fact probably reflect the complexities of the magma reservoir, which may responds in not a uniform way during the different inflation/deflation events (Edmonds et al., 2019; Sparks et al., 2019). The modelled dike is placed ~2 km to the north of the eruptive fissures active during this phase and its geometry and position do not seem compatible with the location of these fissures. Rather, the position of this dike (Figure 9b), indicates it is the western, proximal portion of the radial dike responsible for the second eruptive phase, suggesting that the two segments form a single continuous intrusion. Thus, most of the deformation along the east flank of the first phase seems related to the incipient propagation of the radial dike of the second eruptive phase. During the first phase, the volume of the radial dike is similar to the volume lost by the sill and also to the volume of magma intruded in the previous seven months (Table 1). This suggests that the magma stored in the pre-eruptive period may have been remobilized during the first eruptive phase, promoting the subsidence of the magmatic reservoir and the emplacement of the radial dike. The volume of magma involved in the eruptions at the summit vents during the first eruptive phase was probably negligible compared to that of the radial dike. This proposed scenario is similar to that inferred for the 1998 eruption at Cerro Azul (Teasdale et al., 2005), and agrees with the typical eruptive pattern of Cerro Azul, where the volume of lava erupted at the summit vents is usually much lower than that erupted along the lower flanks (Neumann & Geist, 2000).

The lower portion of the modelled dike is ~1.5 km shallower than the sill. We speculate that, from the north-east edge of the sill, an upward propagation of magma first occurred below the north-east sector of the caldera, which became a radial dike at shallower levels. The temporal resolution of our data does not allow us to test this hypothesis, as only the deformation associated to the radial dike is

recorded. However, the inferred propagation pattern is similar to that observed in the last decades at Fernandina, where radial dikes generally initiate as sill-like intrusions that become progressively steeper below the caldera rim and twist around a radial horizontal axis (Bagnardi et al., 2013). The stress field imposed by the caldera unloading and the gravitational load of Cerro Azul may control this pattern of magma propagation, as at Fernandina (Corbi et al., 2015). The opening of the eruptive fissures of the first phase could have been related to a minor amount of magma that, during the initial steepening of the sill, propagated upward below the north-east caldera rim, reaching the surface. A limited lateral propagation of this dike may have fed the nearby fissures on the upper east flank.

On June 1st, the first eruptive phase ended and the second phase began. This latter phase is associated with the eastward propagation of the radial dike of the first phase, which erupted (on June 3rd) once it reached the topographic low coinciding with the plain between Cerro Azul and Sierra Negra. During this eruptive phase, the deflated area on the volcano summit became significantly larger, with the centre of the subsidence migrating south-eastward. We infer this to be due to the widening of the area of the magma reservoir from which the magma was withdrawn during this phase. The total volume lost by the magmatic system during this phase is about twice that lost during the first event. Our results highlight that the northern portion of the shallow magma reservoir, closer to the radial dike, lost a larger volume than the southern distal zone. Thus, the radial dike was fed mainly by the proximal area of the magmatic reservoir. During this second phase, the estimated amount of magma of the radial dike is, however, about twice the estimated volume lost by the magmatic reservoir and about five times greater than the volume that this dike had during the first phase. This may suggest that an important magma supply from greater depth occurred at Cerro Azul between the first and the second eruptive phase; this may have promoted the further propagation of the dike, triggering the eruption, and the partial replenishment of the volume lost by the magma reservoir. An alternative explanation is an increase in the compressibility of the magma, which can account the volume discrepancy (Rivalta & Segall, 2008). In this prospective, during the first eruptive phase the magma had to be nearly incompressible to explain the similarity in the volume lost by the reservoir and gained by the dike (Rivalta & Segall, 2008). Then the compressibility increased causing the apparent volume discrepancy (Rivalta & Segall, 2008). In any cases, from the first to the second eruptive phase, there is an increase in the volume of magma supplied from the reservoir to the dike, which could also have promoted the further propagation of the radial dike (Anderson & Poland, 2016).

From the first to the second eruptive phase, the radial dike rotated anticlockwise by 28-33°, pointing towards Sierra Negra volcano, and stopped erupting in the depressed area between the two volcanoes. A similar change in the strike and arrest of a dike, when propagating from below a topographic high

to a topographic low in front of a nearby volcanic edifice, was observed also during the 2014 Bardarbunga eruption (Sigmundsson et al., 2015). Topographic variation seems to be the main factor controlling this rotation and arrest between two nearby volcanoes (Walter, 2003; Walter et al., 2006; Heimsson et al., 2015; Sigmundsson et al., 2015; Urbani et al., 2017).

A new uplift within the caldera begun after the eruption; this continued in the following three years (Figure 3i-k), characterized by non-constant rates.

7.1 - Comparison between Cerro Azul and the other western Galápagos calderas

The deformation pattern of the caldera of Cerro Azul shows pre-eruptive uplift, co-eruptive subsidence and post-eruptive uplift (Figure 3i-k). This pattern is similar to that observed in other calderas of the western Galápagos, such as Fernandina in 2005 (Chadwick et al., 2011; Bagnardi and Amelung, 2012) and Sierra Negra in 2005 (Chadwick et al., 2006) and is typical of the mafic calderas (Dvorak and Dzurisin, 1997; Acocella et al., 2015).

Most of the deformation related to the 2008 eruption of Cerro Azul is caused by the propagation of a radial dike. This is typical of the western Galápagos volcanoes, where the eruptions along the flanks of these volcanoes are related to radial dikes (Chadwick & Dieterich, 1995). The propagation pattern of the radial dikes proposed for Fernandina (Bagnardi et al., 2013), where a sill-like intrusion progressively turns upward and twists around an horizontal radial axis, also seems applicable for the 2008 radial dike of Cerro Azul.

According to our results, the magma reservoir constantly fed the radial dike during the two eruptive phases, with an increase in the volume of magma transferred from the reservoir to the dike during the second eruptive phase. This situation is different to what happened at neighbouring Alcedo volcano during the 2010 unrest, where the lack of new magma supply during unrest stopped an incipient lateral propagation of a sill (Galetto et al., 2019), confirming the importance of a continuous supply of magma in the propagation of a dike/sill.

Finally, GPS data show a decrease in the uplift rate of Sierra Negra during the 2008 eruption of Cerro Azul (Poland, 2014). This suggests a possible connection between the two nearby volcanoes at deeper levels, similar to what is observed at the Aira-Kirishima system (SW Japan; Brothelande et al., 2018). This possibility is reinforced by petrological data, which suggest a common source in the lithospheric mantle for the magmas of Cerro Azul and Sierra Negra (Neumann & Geist, 2002). The anticorrelation of deformation between Cerro Azul and Sierra Negra can be tested only in 2008, as no deformation data are available for other periods, with the exception of the 2005 eruption of Sierra Negra, when

Cerro Azul apparently did not deform. Future studies should test this working hypothesis, to understand better the deep plumbing system of these two volcanoes and to try to correlate the dynamics of the deep plumbing system with that of the shallower plumbing systems of these two volcanoes.

8 - Conclusions

The unwrapping limitations affecting our ENVISAT data gave us the opportunity to test a new method, based on the wrapped phase differences among nearby pixels, to model the wrapped data directly, by estimating the integer ambiguities simultaneously with the geophysical parameters. Thanks to this method, we successfully inverted the deformation data of the two eruptive phases of Cerro Azul, recorded by the ascending track data of ENVISAT. Results show that after seven months of pre-eruptive uplift, an eruption, divided in two eruptive phases, occurred at Cerro Azul in 2008. During the first eruptive phase, the incipient propagation of a radial dike promoted uplift on the east flank of Cerro Azul and a coeval first episode of deflation below the caldera, related to its magma reservoir. Eruptions occurred in the upper east flank during the first eruptive phase. The further lateral propagation of the radial dike triggered the second eruptive phase. The radial dike changed its strike when it propagated from below the volcanic edifice to a topographic low, between Cerro Azul and Sierra Negra.

Acknowledgements

The Envisat data are distributed by the European Space Agency (ESA) via ESA's Virtual Archive (http://eo-virtual-archive4.esa.int/) in the framework of the Geohazard Supersites and Natural Laboratory initiative. The ALOS-PALSAR data are copyright JAXA/METI. Landsat 7 image in Figure 1 is freely distributed by the USGS from https://earthexplorer.usgs.gov/ .

The Supporting Information Table is available at https://osf.io/jxeqv/?view_only=bcd204c5082c4025af05ff378d316758

Chapter 4

Preliminary draft not submitted to any Journals yet.

Forecasting the fate of unrest at mafic calderas

Federico Galetto[1], Valerio Acocella[1], Marco Bagnardi[2,3] and Andrew Hooper[2]

[1] Università degli Studi di Roma Tre, Dipartimento di Scienze, Rome, Italy

[2] COMET, School of Earth and Environment, University of Leeds, Leeds, UK

[3] Now at NASA Goddard Space Flight Center, Greenbelt, MD, USA

Corresponding author: Federico Galetto (federico.galetto@uniroma3.it).

Abstract

Calderas are the most active and dangerous volcanic systems on Earth. They usually experience repeated crises (unrest), characterized by a deviation from baseline monitoring parameters, such as changes in seismicity, degassing, and ground deformation. Modern volcanology is still far from understanding whether unrest culminates in eruption or not. Mafic calderas usually experience more regular unrest, culminating in eruption more frequently than felsic calderas. Among mafic calderas, those of the western Galápagos have experienced repeated geodetically-captured eruptive and non-eruptive unrest in the last decades and thus represent an ideal site to investigate unrest at mafic calderas. Here we review these unrest episodes, mainly considering the estimated injected volumes of magma, the related intrusive rates and the unrest outcome. We show that, when intrusion rates are > (5±4) x10^{-2} km^3/year, unrest nucleates a dike from the reservoir in <1 year, eventually triggering eruption within ~1 year. When the intrusion rates are < (5±4) x10^{-2} km^3/year, unrest usually ends without any dike nucleation, especially if lasting <1 year. Injection rates of (5±4) x 10^{-2} km^3/year show a transitional behaviour. These behaviours are supported by available data from other mafic calderas, sharing similar features and suggesting a preliminary working hypothesis to try to forecast the fate of unrest, considering the injection rates of intruded magma during unrest in mafic calderas with shallow reservoirs.

1- Introduction

Calderas are broad sub-circular depressions formed by the withdrawal of magma from the magmatic system, as a consequence of an eruption or lateral propagation of magma (Cole et al., 2005; Stix & Kobayashi, 2008; Howard et al., 2018). All active calderas experience "crises", known as unrest, during which the baseline monitoring parameters, such as seismicity, ground deformation and degassing, change (Newhall & Dzurisin, 1988; Hill et al., 2003; Gottsmann et al., 2007; Acocella et al., 2015; Robertson & Kilburn, 2016). Unrest can culminate with an eruption or not, but almost all eruptions are preceded by unrest episodes, often lasting <1 year (Newhall & Dzurisin, 1988; Biggs et al., 2014; Acocella et al., 2015; Robertson & Kilburn, 2016; Sandri et al., 2017). Therefore, the study of unrest episodes has important implications for the assessment of volcanic hazard, and a better understanding of the related processes is one of the main challenges for modern volcanology (Acocella et al., 2015; Sandri et al., 2017). Felsic calderas erupt infrequently and show a dual behavior (Acocella et al., 2015): they are restless for decades or are characterized by isolated and short unrest episodes. Mafic calderas experience repeated and more regular unrest, often characterized by uplift with pre-eruptive seismicity, followed by eruption with contemporary deflation (Dvorak & Dzurisin, 1997; Nooner & Chadwick et al., 2016). Among mafic calderas, there are the six active calderas of the western Galápagos (Ecuador). These calderas (Fernandina, Cerro Azul, Sierra Negra, Alcedo, Darwin and Wolf), placed above the upwelling region of a hot spot (Villagomez et al., 2014), have in the last decades experienced repeated eruptive and non-eruptive unrest (see references in Table 1). Ground deformation is a constant feature of these unrest episodes. As the other parameters that characterize unrest, such as seismicity and degassing, are poorly or not monitored at Galápagos calderas, studies of unrest at Galápagos have focussed on measuring and modelling ground deformation, mainly measured using Synthetic Aperture Radar Interferometry (InSAR; see references in Table 1). Since these unrest episodes have been studied with similar approach and methods, they provide the opportunity to be directly compared and make the western Galápagos a key location to investigate unrest at mafic calderas.

Here we review all the geodetically monitored unrest episodes at the western Galápagos calderas, mainly considering the estimated injected volumes of magma and the related intrusive rates. To frame these data in a broader context, we also compare them with those from the other mafic calderas with shallow magma reservoirs (reservoir is used as defined by Sparks et al., 2019). Our results highlight a relationship between the rates at which magma is injected inside a shallow magmatic reservoir and the possibility to nucleate a dike from the reservoir, opening promising and exciting opportunities to forecast eruptions at mafic calderas.

2- Methods

We analysed all the available data on the intruded volumes and on the corresponding injection rates occurred during the geodetically constrained unrest episodes at the western Galápagos calderas between 1992 and 2011. Then, to place these data in a broader frame, we also included available geodetic data from other mafic calderas worldwide. In using these data (Table 1), we made the following assumptions:

1) Western Galápagos calderas in some cases have two connected magma reservoirs, a shallower and a deeper one (Chadwick et al., 2011; Bagnardi and Amelung, 2012; Stock et al., 2018). However, there are only few pre-eruptive geodetic data on the deeper reservoir, probably even affected by larger uncertainties. This is because the deeper system can often accommodate new magma without any associated surface deformation (Stock et al., 2018). Therefore, we focus our analysis only on the deformation data relative to the shallow reservoir. In the supplementary Figure S1 we present an attempt at including the limited available data for deeper systems.
2) We label "plain unrest" an unrest characterized by inflation of the shallow reservoir without any dike nucleation, neither during the unrest nor within 1.5 years after its end (see point 5).
3) We label "unrest-triggered sill" an unrest promoting the limited (within the radius of the caldera) propagation of a sill from the shallow reservoir, without eruption.
4) We label "unrest-triggered dike" an unrest that ends with the nucleation and propagation of a dike from the shallow magma reservoir, regardless of whether the dike reaches the surface, triggering an eruption, or not. In our analysis, we separated these unrest episodes lasting more than 1 year from those lasting less than 1 year.
5) Sometimes unrest ends without any dike nucleation, but then a dike develops after a period without displacement or with minor subsidence (e.g. Okmok; Lu et al., 2005). We label this as "unrest-triggered dike" only if the dike developed <1.5 years after the end of the uplift; without any dike nucleation, we classify the unrest as plain unrest.
6) The calderas considered here outside the Galápagos have a shallow magma reservoir comparable in depth (top shallower than 5-6 km) and size to those of the Western Galápagos. Their composition is mainly mafic, implying that they are fed by mafic magma injected into mafic or, eventually, intermediate shallow reservoirs, and their erupted products are also mostly mafic. Their deformation episodes have been detected using GPS or InSAR data, and the associated intruded volumes were estimated through the inversion of the latter. Calderas

with these characteristics were selected using the Smithsonian Global Volcanism Program database (Global Volcanism Program, 2013).

All the considered data (injected volumes and rates) were obtained using a consistent approach, through the inversion of geodetic data (InSAR and/or GPS data) using similar elastic models to retrieve the deformation sources (see references in Table 1). The sources used for the inversion are the point source (Mogi, 1958), the finite spherical cavity source (McTigue, 1987), the sill/dike source (Okada, 1985; Nikkhoo et al., 2017) and the ellipsoid source (Yang et al., 1988) (see references in Table 1). The use of a point source, rather than a sill source, could lead to an underestimation of the volume of about 15% (Nikkhoo et al., 2017), which has been included in the errors (Table 1).

3- Results

In Figure 1a-b we show the distribution of the injection rates (Q) associated with the unrest episodes concerning the shallow reservoirs of the western Galápagos calderas. The highest values of Q (>2 $x10^{-2}$ km^3/yr) are associated with pre-eruptive unrest episodes culminating in eruption in ≪1 year at Fernandina, Sierra Negra and Cerro Azul (unrest-triggered dike) (Figure 1a, b; Table 1). Conversely, the unrest episodes associated with lower Q usually last >1 year and culminate without any dike nucleation (plain unrest): more in detail, none of the unrest episodes lasting <1 year nucleated a dike; in a few cases, when unrest lasts >1 year, it can nucleate a sill or a dike after >2 years from the unrest onset (Figure 1a-b).

To better constrain these possible behaviours, we expanded our dataset by including data from other mafic calderas with shallow reservoirs (see Methods section) (Figure 1c-d, Table 1). Our results confirm the general relationships between the injected rates and the outcome of unrest. In all the analysed unrest episodes with Q > (5±4) x 10^{-2} km^3/yr, the nucleation of a dike, which may sometimes trigger eruptions, occurs in <1 year (unrest-triggered dike) (Figure 1c-d). Conversely, for rates < (5±4) $x10^{-2}$ km^3/yr unrest usually lasts >1 year, and ends as plain unrest. More in detail, unrest ends without any dike nucleation (plain unrest), if it lasts <1 year (Figure 1d). When it lasts >1 year, it usually ends as plain unrest, even if in few cases (Alcedo, Fernandina and Okmok) the nucleation of a sill (unrest-triggered sill) or of a dike (unrest-triggered dike) can occur, but only after >2 years from the unrest onset (Table 1; Figure 1c-d).

Therefore, rates of (5±4) x 10^{-2} km^3/yr represent a transition between the two behaviours, with lower values associated with plain unrest and higher values showing dike nucleation within 1 year (Figure 1c, d).

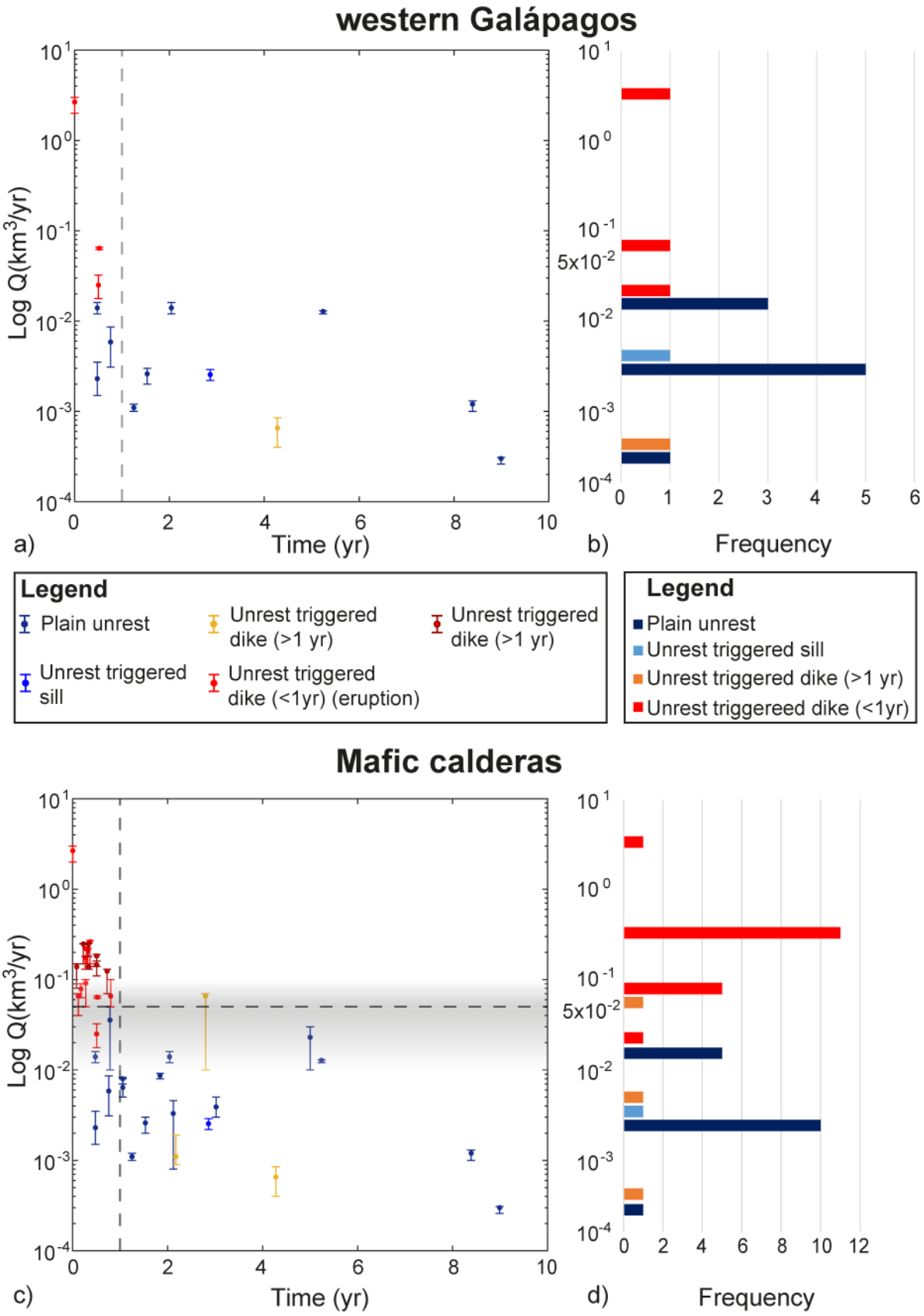

Figure 1 a) Duration of unrest and corresponding injection rates (Q). b) Histogram of frequency of the rates associated with the Galápagos unrest episodes. c) and d) are the same as a) and b), but also

include data from similar mafic calderas worldwide. In panel c) the grey area highlights the zone with transitional rates (5±4 x10^{-2} km^3/yr, with the horizontal dotted grey line placed at Q= 5 x10^{-2} km^3/yr), which separates the unrest triggered-dike (< 1 yr) from the plain unrest behaviours. The vertical dotted grey line separates the unrest episodes lasting <1 year from those lasting >1 year.

4- Discussion

4.1 – General considerations.

Our results highlight a relationship between the injection rates into the shallow magma reservoir, estimated from the geodetic inversion of the uplift, and the outcome of unrest in mafic calderas with shallow reservoirs. Our dataset shows that when the uplift is related to new magma supplies into the shallow reservoir at rates > (5±4) x10^{-2} km^3/yr (high rates), unrest nucleates a dike, which often triggers an eruption in <1 year (usually much less) (Figure 2). Conversely, when the uplift is related to new magma supplies into the shallow reservoir at rates < (5±4) x10^{-2} km^3/year (low rates), unrest usually lasts >1 year and terminates as plain unrest. In a few cases it can nucleate a dike, but only if the unrest lasts >1 year (more likely >2 years) (Figure 2). Rates of (5±4) 10^{-2} km^3/yr thus represent a transition between the two end members; in particular, for rates of 1-5 x10^{-2} km^3/yr plain unrest prevails, while rates of 5-9 x10^{-2} km^3/yr usually, but not always, nucleate a dike in <1 year (Figure 1c-d).

Conversely to previous studies that suggested that uplift may not represent a reliable precursor for an eruption (Biggs et al., 2014; Sandri et al., 2017), our analysis emphasize the importance of monitoring the deformation of the caldera floor to determine the injection rates and try to forecast the outcome of unrest (see Figure 2).

Moreover, our analysis highlights that pre-eruptive unrest can last >1 year (Figure 1), conversely to what stated by Sandri et al., (2017); this discrepancy is due to the fact that our database includes events that were not considered by Sandri et al., (2017).

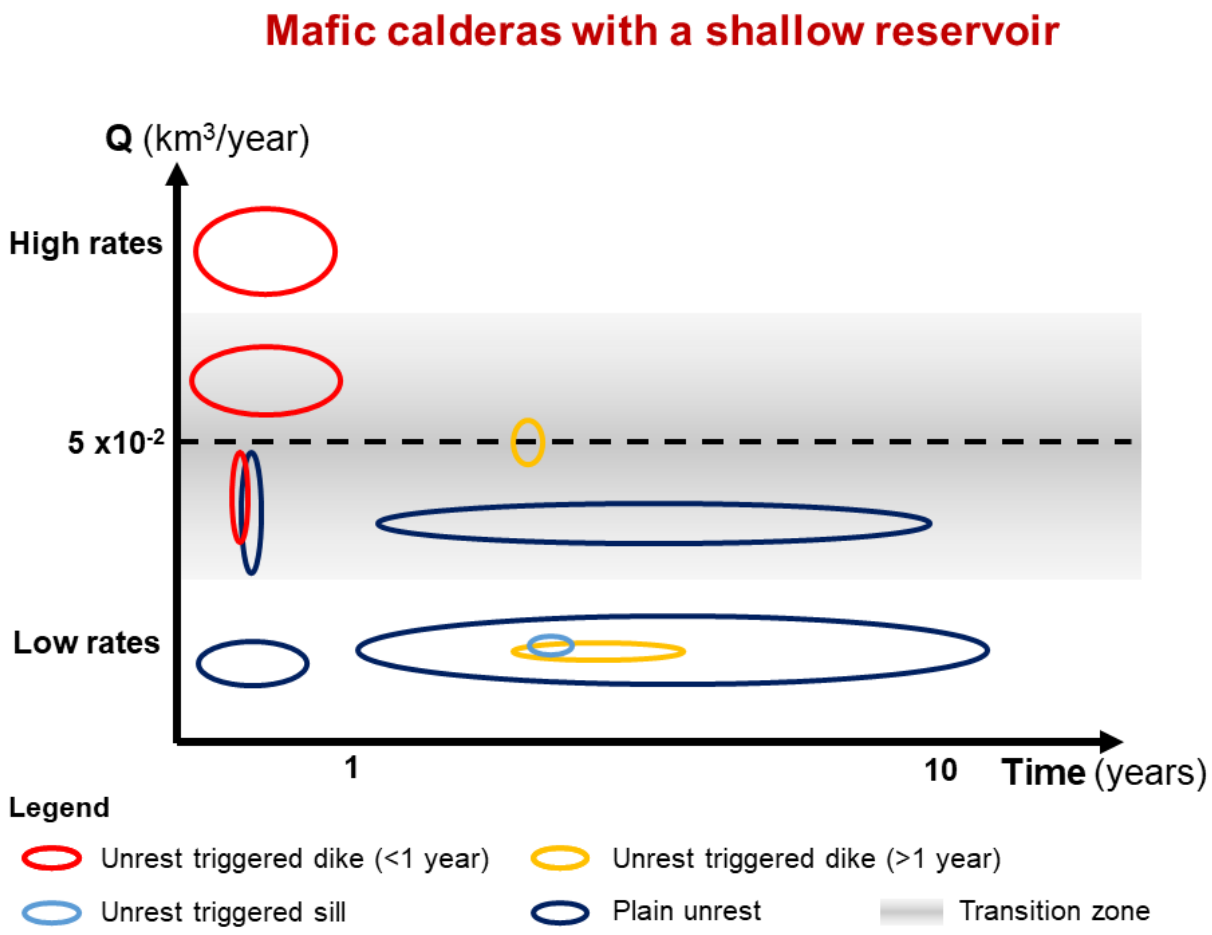

Figure 2. Schematic for mafic calderas with a shallow reservoir.

4.2 - Other factors affecting the fate of unrest.

The collected data suggest that the injection rate is a first-order parameter in determining the fate of unrest. However, other features may affect this behaviour and explain the variability in the transition zone defined by rates of 5±4 x 10^{-2} km^3/yr.

In a closed system, the overpressure (ΔP) generated by the volume change (ΔV) due to the inflow of new magma in the system is expressed by (Blake, 1981; Tramontano et al., 2017; Le Mével et al., 2016) (1):

$$\Delta P = \frac{\Delta V}{V_0\,(\beta_m + \beta_w)} \qquad (1)$$

Where V_0 is the initial volume of the magmatic system, β_m is the compressibility of the liquid and β_w is the compressibility of the host rock. According to Equation 1, larger and more compressible

systems can accommodate larger volumes of magma before reaching the critical overpressures for triggering a dike. Assuming an ideal spherical geometry of the magmatic system, the relationship between ΔP and Q is expressed by (Jellinek & De Paolo, 2003; Caricchi et al., 2014) (2):

$$\Delta P = \frac{2\eta Q}{3V_0} \qquad (2)$$

where η is viscosity of the host rock. Therefore, larger systems need a higher injection rate to reach the critical overpressures to nucleate a dike. Equations 1 and 2 show how the intrinsic characteristics of each caldera, such as the size and compressibility of the system and the viscosity of the host rock, influence the values of ΔV and Q necessary to reach the critical overpressures for triggering a dike. Therefore, the transition zone defining the different outcome of unrest also depends on the intrinsic properties of each reservoir, including its size, compressibility and viscosity of the host rock. In our analysis, we tried to minimize these differences by selecting calderas with similar characteristics (see Section 3). However, these parameters explain why it is not possible to extrapolate our results to calderas with different properties (Jellinek & De Paolo, 2003; Degruyter & Huber, 2014).

According to equation 1 and 2, the critical rates for triggering a dike are comparable only in calderas with comparable properties (V_0, β and η), as is the case for the calderas here analysed (see references in Table 1). This would explain the results in Figure 1, where the outcome of the unrest depends on the injection rates. Rates > (5±4) x10^{-2} km^3/yr would allow reaching the critical ΔP in < 1 year, explaining the occurrence of rapid unrest-triggered dike. Conversely, low rates would not allow reaching the critical ΔP in <1 year, as they would take longer to inject enough magma for the critical threshold. Longer times enhance both the possibility that the unrest could terminate before reaching the critical ΔP and the occurrence of other processes, such as the viscous relaxation, that prevent critical pressure being reached (Degruyter & Huber, 2013). In addition, it should be considered that low injection rates may not even be sufficient to maintain eruptible magma (<50% of crystallinity; Marsh, 1981) in the shallow reservoir, promoting plain unrest. This is for example the case of Wolf caldera, where petrologic data suggest that the very low injection rates (Q=3 x10^{-4} km^3/year) inferred from 2000 to 2009, were just sufficient to maintain the shallow reservoir in an ephemeral super-solidus condition (Stock et al., 2018).

We are also aware that high injection rates alone may be a necessary, but not always sufficient, condition to trigger a dike, especially for transitional rates in the order of 5±4 10^{-2} km^3/yr. For example, the injection rates of 6.4 x10^{-2} km^3/yr before the 2005 eruption at Sierra Negra may not have been sufficient to trigger the eruption, and the simultaneous occurrence of other processes (a

nearby earthquake occurring just before the eruption) should be considered to explain the eruption (Gregg et al., 2018).

Therefore, when an unrest associated with low injection rates ends after >1 year with the propagation of a dike, and in some cases with an eruption, the occurrence of other triggering processes may contribute (or be necessary) for the propagation of the dike. These processes may be:

1) External processes, such as the occurrence of a nearby earthquake (Gregg et al., 2018).
2) Internal processes, such as second boiling (Blake , 1984).
3) Sudden increase in the rates just before the eruption, not recorded because of poor temporal resolution of the geodetic data.

Finally, the long-term accumulation of magma can eventually lead to a critical level of magmatic pressure (equation 1) if the rates are sufficient to maintain eruptible magma in the shallow reservoir (e.g. transitional rates) (Nooner & Chadwick, 2016).

Therefore, future studies should better investigate the eruption associated to long-term unrest characterized by low rates.

4.3- Implications for volcanic hazard

As it is currently possible to access and invert space-geodetic data in relatively short time spans (e.g. see Bagnardi and Hooper, 2018), we can promptly evaluate if the uplift is related to the inflation of a shallow source, and the corresponding intrusion rates. Our study shows how the injection rates could allow determining the outcome of unrest accordingly to the scheme in Figure 2.

These data can be used as a starting point to try to further test and forecast the fate of unrest at mafic calderas with shallow magma reservoirs. When the uplift is related to new magma supplies in the shallow system at $Q > 5\pm4 \times10^{-2}$ km^3/yr (high rates), we can expect the propagation of a dike, which is a necessary condition for having an eruption (Rubin, 1995; Rivalta et al., 2015), in <1 year. Conversely, in cases where the inflow of new magma in the shallow system occurs at rates $< 5\pm4 \times10^{-2}$ km^3/yr (low rates), we can expect plain unrest lasting >1 year. We may expect the formation of a dike or a sill can occur only after >1 years (usually >2 year) from the unrest onset (Figure 2). Therefore, uplift related to these low injection rates seems to not be a diagnostic precursor of an imminent eruption, especially if lasting <1 year.

Acknowledgments

We thank Prof. Luca Caricchi for the constructive discussions.

Table 1

	Start	End	V(km^3)	Q (km^3/year)	Q_e (km^3/year)	Code	Depth	Time (yr)	References
Fernandina[a]	16/01/2001	26/04/2005	0.0028	0.00066	0.0004-0.00085	2[(b)]		4.27	(Geist et al., 2006) (Chadwick et al., 2011)
Fernandina	09/08/2005	07/11/2006	0.00136	0.0011	0.001-0.0012	0	1-2	1.25	(Chadwick et al., 2011)
Fernandina	27/01/2007	21/07/2007	0.0011	0.0023	0.0015-0.0035	0	1-2	0.48	(Bagnardi & Amelung, 2002)
Fernandina	28/09/2007	09/04/2009	0.004	0.0026	0.002-0.003	0	1-2	1.53	(Bagnardi, 2014)
Fernandina	10/04/2009	10/04/2009	0.00729	2.661	2-3	3[(b)]	1-2	0.0027	(Bagnardi et al., 2013)
Sierra Negra	26/09/1998	20/03/1999	0.0067	0.014	0.012-0.016	0	2	0.48	(Yun et al., 2006)
Sierra Negra	01/04/2003	15/04/2005	0.029	0.014	0.012-0.016	0	2	2.04	Chadwick et al., 2006)
Sierra Negra	16/04/2005	21/10/2005	0.033	0.064	0.062-0.066	3[(b)]	2	0.52	Chadwick et al., 2006)
Sierra Negra	01/11/2005	26/01/2011	0.067	0.0128	0.012-0.013	0	2	5.24	(Bagnardi, 2014)
Alcedo	Jan-2007	Jan-2010	0.0073	0.00255	0.0022-0.0029	1	2-3	2.86	(Galetto et al., 2019)
Alcedo[c]	10/06/2010	13/03/2011	0.0041	0.00585	0.0031-0.0086	0	2-4	0.76	(Galetto et al., 2019)
Cerro Azul	19/10/2007	20/04/2008	0.012	0.025	0.0177-0.0323	3[(b)]	5	0.50	Chapetr 3
Wolf[d]	01/01/2000	27/12/2008	0.0015	0.0003	0.00026-0.00031	0	1-1.5	8.99	(Stock et al., 2018)
Darwin	15/06/1992	01/11/2000	0.01	0.0012	0.001-0.0013	0	3-4	8.39	(Bagnardi, 2014)
Krafla	29/09/1976	30/10/1976	0.078	0.139	0.08-0.15	3	3	0.085	(Ewart et al., 1991)
Krafla	30/10/1976	20/01/1977	0.042	0.248	0.15-0.25	3	3-3.5	0.23	(Ewart et al., 1991)
Krafla	20/01/1977	27/04/1977	0.025	0.175	0.13-0.18	3[(b)]	3-3.5	0.27	(Ewart et al., 1991)
Krafla	27/04/1977	08/09/1977	0.07	0.26	0.15-0.27	3[(b)]	3.5-4	0.37	(Ewart et al., 1991)
Krafla	08/09/1977	06/01/1978	0.059	0.248	0.18-0.25	3	3.5-4	0.33	(Ewart et al., 1991)
Krafla	06/01/1978	10/07/1978	0.068	0.18	0.14-0.19	3	3-3.5	0.51	(Ewart et al., 1991)
Krafla	10/07/1978	10/11/1978	0.045	0.138	0.13-0.14	3	3-3.5	0.34	(Ewart et al., 1991)
Krafla	10/11/1978	13/05/1979	0.04	0.146	0.11-0.16	3	3-3.5	0.50	(Ewart et al., 1991)
Krafla	13/05/1979	02/02/1980	0.06	0.124	0.07-0.13	3	3-4	0.73	(Ewart et al., 1991)
Krafla	02/02/1980	16/03/1980		0.066	0.04-0.07	3[(b)]	3.5-4	0.12	(Ewart et al., 1991)
Krafla	16/03/1980	10/07/1980	0.04	0.21	0.15-0.22	3[(b)]	3-4	0.32	(Ewart et al., 1991)
Krafla	10/07/1980	18/10/1980	0.022	0.09	0.05-0.1	3[(b)]	2.5-3	0.27	(Ewart et al., 1991)
Krafla	18/10/1980	30/01/1981	0.02	0.22	0.15-0.23	3[(b)]	3	0.29	(Ewart et al., 1991)
Krafla	30/01/1981	18/11/1981	0.052	0.066	0.05-0.1	3[(b)]	4.5-5	0.80	(Ewart et al., 1991)
Krafla	18/11/1981	04/09/1984	0.072	0.066	0.01-0.07	2[(b)]	3.5-4.5	2.80	(Ewart et al., 1991)
Eyjafjallajokull	03/08/1993	06/06/1995	0.016	0.0087	0.008-0.0092	0	4.5	1.84	(Pedersen and Sigmundsson, 2004)
Eyjafjallajokull	19/07/1999	01/05/2000	0.028	0.036	0.01-0.05	0	6-6.5	0.79	(Pedersen and Sigmundsson, 2006)

Eyjafjallajokull	Dec. 2009	28/02/2010	0.013	0.079	0.063-0.09	3[(b)]	4-6	0.18	(Sigmundsson et al., 2010)
Hudson	1993	1998		0.023	0.01-0.03	0	5-6	6	(Pritchard e Simons, 2014)
Okmok	31/10/1992	20/11/1993	0.0076	0.0064	0.005-0.008	0	3-4	1.06	(Lu et al., 2005)
Okmok	07/08/1993	09/10/1995	0.0036	0.0011	0.0009-0.0019	2[(b)]	3-4	2.17	(Lu et al., 2005)
Okmok[e]	17/07/1997	25/07/2000	0.013	0.0039	0.003-0.005	0	3-4	3.02	(Lu et al., 2005)
Okmok[f]	26/08/2000	08/10/2002	0.00694	0.0033	0.0008-0.0046	0	3-4	2.12	(Lu et al., 2005)
Okmok	14/08/2002	02/09/2003	0.0076	0.008	0.007-0.0083	0	3-4	1.05	(Lu et al., 2005)

Start and end are the dates of the onset and the end of the unrest. Time is the duration of the unrest. V and Q are respectively the volume and the rates estimated from the inversion of geodetic data. Q_e is the interval of confidence of the rates. Code is referred to the outcome of the unrest (0=non-eruptive; 1=Unrest-triggered sill; 2= unrest-triggered dike >1 year; 3=unrest-triggered dike <1 year). Depth is the depth of the modelled source (with respect to the surface).

[a] Geist et al., (2006) inverted data from 16/01/2001 to 13/06/2002 (V=0.0012 km^3; Q= 0.00085 km^3/year), while Chadwick et al., (2011) inverted data from 18/01/2003 to 26/04/2005 (V= 0.00075 km^3, Q=0.0004 km^3/year). Bagnardi, (2014) showed that the unrest continued in between at similar rates.

[b] The dike fed an eruption.

[c] InSAR data do not allow to determine if the uplift continued or not after 13 March 2011.

[d] It is possible that the unrest started in 1992. Data from 2004 are better temporally constrained (Stock et al., 2018).

[e] Lu et al., 2005 inverted separately data from 17/07/1997 to 29/09/1998 (V=0.0057 km^3; Q=0.0041 km^3/year), from 10/09/1998 to 30/09/1999 (V=0.0041 km^3; Q=0.0039 km^3/year) and from 14/09/1999 to 25/07/2000 (V=0.0032 km^3; Q=0.0037 km^3/year).

[f] Lu et al., 2005 inverted separately data from 26/08/2000 to 15/09/2001 (V=0.0019 km^3; Q=0.0008 km^3/year) and from 10/07/2001 to 08/10/2002 (V=0.005 km^3; Q=0.0035 km^3/year).

Chapter 5

Conclusions

To better understand unrest at the western Galápagos calderas, I have analysed some unrest episodes at Alcedo (non-eruptive unrest from 2007 to 2011) and Cerro Azul (eruptive unrest in 2008) and then tried to provide a general synthesis on unrest at mafic calderas, considering also previously published data.

In particular, Alcedo and Cerro Azul provided the opportunity to investigate unrest episodes with opposite outcome, which are essential for analysing the problem of caldera unrest from a broader perspective, as it is equally important to understand both processes leading to the eruption and those that do not. Results on the non-eruptive unrest episodes occurred at Alcedo highlight two episodes of uplift, from January 2007 to January 2010 and from June 2010 to March 2011, triggered by the emplacement of sills inside the shallow magmatic reservoir. These two events were separated by an episode, from January 2010 to June 2010, with limited lateral propagation of magma from the magma reservoir, which possibly ended for the lack of magma supply. My results have better constrained the current position of the shallow reservoir of Alcedo, and suggest that the intra-caldera fault is active during the unrest episodes, explaining the asymmetrical deformation pattern of the unrest episodes in the last decades. These shorter-term unrest episodes match in location (southern part of the caldera) and shape (asymmetry) with the longer-term process of resurgence. This consistency suggests that Alcedo has been experiencing incremental and discontinuous episodes of growth of its resurgent block, related to the emplacement of multiple sills, providing the unusual opportunity to witness the short-term stages of growth of a rare minor resurgence in a basaltic caldera.

The analysis of the unrest at Cerro Azul was complicated by the presence of unwrapping errors in some of the InSAR data. However, these errors provided the opportunity to test a new method, based on the wrapped phase differences among nearby pixels, to model the wrapped data directly, by estimating the integer ambiguities simultaneously with the geophysical parameters. Therefore, the deformation data of Cerro Azul have been successfully inverted. Results highlight that, after seven months of pre-eruptive uplift of the caldera floor, two eruptive phases occurred at Cerro Azul from May 29th to June 11th 2008. These two phases are mainly related to the propagation of a radial dike towards a topographic low between Cerro Azul and Sierra Negra. The propagation of the radial dike and the second eruptive phase were likely triggered by a new magma supply from depth.

The analysis of the unrest episodes at Alcedo and Cerro Azul highlights the important role of a continuous magma supply in promoting the propagation of a sill/dike and triggering eruptions. At Alcedo the lack of new magma supplies probably halted the incipient lateral propagation of a sill in 2010, and the unrest ended as non-eruptive. On the contrary, at Cerro Azul a new supply of magma occurred between the first and second eruptive phase, probably triggering the further lateral propagation of the dike and the second eruptive phase.

Moreover, the studied non-eruptive unrest episodes at Alcedo showed lower injection rates than those occurred during the pre-eruptive period at Cerro Azul. This underlines the importance of the magmatic injection rates in determining the fate of unrest. Therefore, in the last part of this thesis, I investigated the possible role of the injection rates in determining the outcome of the unrest. With this aim, I reviewed all the geodetically monitored unrest episodes at the western Galápagos calderas, mainly considering the estimated injected volumes of magma and the related intrusive rates. These data have been further compared to those from other mafic calderas with similar characteristics. Results highlight a general relationship between the injection rates inside the shallow magma reservoir, estimated from the geodetic inversion of the uplift, and the outcome of unrest. When the uplift is related to new magma supplies in the shallow reservoir at rates > (5±4) $x10^{-2}$ km^3/yr, unrest nucleates a dike, which often triggers an eruption, in <1 year. Conversely, when the uplift is related to new magma supplies in the shallow reservoir at rates < (5±4) $x10^{-2}$ km^3/year, unrest usually lasts >1 year and terminates without any propagation of magma from the magmatic reservoir (plain unrest). In a few cases this may nucleate a dike, but only if the unrest lasts >1 year (usually >2 years). Rates of (5±4) 10^{-2} km^3/yr represent a transition between the two end members; in particular, for rates of 1-5 $x10^{-2}$ km^3/yr plain unrest prevails, while rates of 5-9 $x10^{-2}$ km^3/yr usually, but not systematically, nucleate a dike in <1 year.

The results of this thesis highlight the importance of the injection rates as a first-order parameter in determining the outcome of the unrest, according to previous studies (Woods & Koyaguchi, 1994; Caricchi et al., 2014; Degruyter & Huber, 2014). The most reliable way to estimate the magmatic injection rates during unrest is to use ground deformation. Therefore, conversely to previous studies, which associated a limited importance to geodetic studies in determining the fate of unrest (Sandri et al., 2017), it is here proposed that geodetic monitoring may be a crucial tool to determine the fate of unrest, thus opening new perspectives on forecasting eruptions.

The extent of applicability of the results obtained here should be considered valid only for the mafic calderas showing similar features to those analysed here. These features are: a shallow (<5-6 km)

reservoir, a mafic composition, size of the reservoir comparable to those of the calderas here analysed (Blake, 1981; Jellinek & De Paolo, 2003; Tramontano et al., 2017).

The conclusions of this thesis thus cannot be extrapolated in a straightforward way to mafic calderas with different properties from the ones listed above, especially in terms of the absolute value of the rates promoting the different outcome of the unrest. Therefore, even though a similar behaviour as the one proposed here may be observed in any other mafic caldera, variations, also significant, may be expected.

In this thesis, I investigated the unrest at mafic calderas, as these latter usually experience repeated and more regular unrest with respect to felsic calderas. The substantial differences in the composition, size, amount of gas and compressibility existing between felsic calderas and the mafic calderas here analyzed do not allow to extent the results of this thesis to any felsic caldera, as these latter usually required much higher overpressures to trigger a dike (Jellinek & De Paolo, 2003; Degruyter & Huber, 2014). However, some non-eruptive unrest episodes at felsic calderas (e.g. Campi Flegrei in 1981-1983 and in 2012-2013 and Laguna del Maule in 2007-2014) are characterized by rates comparable to those that can promote plain unrest in the calderas here analyzed (Le Mevel et al., 2016; Amoruso et al., 2014; D'Aiura et al., 2015).

This thesis has proposed an original and innovative approach to forecast the propagation of a dike at mafic calderas experiencing unrest characterized by an uplift of the caldera floor related to the inflation of the shallow reservoir.

As it is currently possible to access and invert space-geodetic data in relatively short time spans (a very few days; e.g. see Bagnardi and Hooper, 2018), it has now become feasible to promptly evaluate if the uplift is related to the inflation of a shallow source, and determine the corresponding intrusion rates. This opens promising opportunities to quickly predict the outcome of the unrest.

Clearly, our forecast capability on this type of calderas depends on the quality and temporal resolution of the geodetic monitoring data. For example, it is possible that some of the unrest associated with low injection rates ending after >1 year with the propagation of a dike may be related to a sudden increase in the rates just before the eruption, not detected for poor temporal resolution of the geodetic data. The much higher temporal resolution of the modern InSAR satellites could allow better investigating this eventuality in the next unrest episodes at the analysed calderas. However, the propagation of a dike, associated to low and transitional rates, may be due to other triggering factors, such as the seismicity (Gregg et al., 2018). Therefore, the simultaneous monitoring of other parameters, such as the seismicity, is equally important for forecasting an eruption.

Final acknowledgments

I would like to thank Prof. Valerio Acocella for the opportunity of this Ph. D. and for the help and the useful suggestions that he gave me. I would like to thank my co-supervisors Dr. Marco Bagnardi and Prof. Andy Hooper for teaching me the InSAR technique and for the useful suggestions.
Finally, I would like to thank my friends Marco Bonnat, Simone Racano, Costanza Rossi, Simone Bernardini, Angela Stallone, Giovanni Diaferia, Andrea Sembrioni, Ileana Garozzo, Dario and Azzurra.

Reference

Acocella, V. (2007). Understanding caldera structure and development: An overview of analogue models compared to natural calderas. *Earth-Science Reviews*, 85, 125-160. https://doi.org/10.1016/j.earscirev.2007.08.004

Acocella, V., Di Lorenzo, R., Newhall, C., & Scandone, R. (2015). An overview of recent (1988 to 2014) caldera unrest: Knowledge and perspectives. *Reviews of Geophysics*, 53, 896-955. https://doi.org/10.1002/2015RG000492

Amelung, F., Jónsson, S., Zebker, H., & Segall, P. (2000). Widespread uplift and 'trapdoor' faulting on Galápagos volcanoes observed with radar interferometry. *Nature*, 407, 993-996. https://doi.org/10.1038/35039604

Amelung, F., Yun, S. H., Walter, T. R., Segall, P., & Kim, S. W. (2007). Stress control of deep rift intrusion at Mauna Loa Volcano, Hawaii. *Science*, 316, 1026-1030. https://doi.org/10.1126/science.1140035

Amoruso, A., Crescentini, L., & Sabbetta, I. (2014). Paired deformation sources of the Campi Flegrei caldera (Italy) required by recent (1980–2010) deformation history. *Journal of Geophysical Research: Solid Earth*, 119, 858-879. https://doi.org/10.1002/2013JB010392

Amoruso, A., Crescentini, L., D'Antonio, M., & Acocella, V. (2017). Thermally-assisted magma emplacement explains restless calderas. *Scientific Reports*, 7, 7948. https://doi.org/10.1038/s41598-017-08638-y

Bagnardi, M. (2014). Dynamics of magma supply, storage and migration at basaltic volcanoes: Geophysical studies of the Galápagos and Hawaiian volcanoes. (PhD thesis). Miami, FL: University of Miami.

Bagnardi, M., & Amelung, F. (2012). Space-geodetic evidence for multiple magma reservoirs and subvolcanic lateral intrusions at Fernandina Volcano, Galápagos Islands. *Journal of Geophysical Research: Solid Earth*, 117. https://doi.org/10.1029/2012JB009465

Bagnardi, M., & Hooper, A. (2018) Inversion of surface deformation data for rapid estimates of source parameters and uncertainties: A Bayesian approach. *Geochemistry, Geophysics, Geosystems, 19*. https://doi.org/10.1029/2018GC007585

Bagnardi, M., Amelung, F., & Poland, M. P. (2013). A new model for the growth of basaltic shields based on deformation of Fernandina volcano, Galápagos Islands. *Earth and Planetary Science Letters*, 377, 358-366. http://dx.doi.org/10.1016/j.epsl.2013.07.016

Baker, S., & Amelung, F. (2012). Top-down inflation and deflation at the summit of Kīlauea Volcano, Hawai'i observed with InSAR. *Journal of Geophysical Research: Solid Earth*, 117. https://doi.org/10.1029/2011JB009123

Biggs, J., Ebmeier, S. K., Aspinall, W. P., Lu, Z., Pritchard, M. E., Sparks, R. S. J., & Mather, T. A. (2014). Global link between deformation and volcanic eruption quantified by satellite imagery. *Nature Communications*, 5, 3471. https://doi.org/10.1038/ncomms4471

Biggs, J., Robertson, E., & Cashman, K. (2016). The lateral extent of volcanic interactions during unrest and eruption. *Nature Geoscience*, 9, 308. https://doi.org/10.1038/ngeo2658

Biggs, J., & Pritchard, M. E. (2017). Global volcano monitoring: what does it mean when volcanoes deform? *Elements*, 13, 17-22. https://doi.org/10.2113/gselements.13.1.17

Blake, S. (1981). Volcanism and the dynamics of open magma chambers. *Nature*, 289, 783. https://doi.org/10.1038/289783a0

Blake, S. (1984)Magma mixing and hybridization processes at the alkalic, silicic, Torfajokull central volcano triggered by tholeiitic Veidivotn fissuring, south Iceland. *Journal of Volcanology and Geothermal Research*, 22, 1-31, https://doi.org/10.1016/0377-0273(84)90033-7

Brothelande, E., Amelung, F., Yunjun, Z., & Wdowinski, S. (2018). Geodetic evidence for interconnectivity between Aira and Kirishima magmatic systems, Japan. *Scientific reports*, 8, 9811. https://doi.org/10.1038/s41598-018-28026-4

Bürgmann, R., Rosen, P. A., & Fielding, E. J. (2000). Synthetic aperture radar interferometry to measure Earth's surface topography and its deformation. *Annual review of earth and planetary sciences*, 28, 169-209.

Canales, J. P., Dañobeitia, J. J., Detrick, R. S., Hooft, E. E., Bartolomé, R., & Naar, D. F. (1997). Variations in axial morphology along the Galápagos spreading center and the influence of the Galápagos hotspot. *Journal of Geophysical Research: Solid Earth*, 102, 27341-27354. https://doi.org/10.1029/97JB01633

Canales, J. P., Ito, G., Detrick, R. S., & Sinton, J. (2002). Crustal thickness along the western Galápagos Spreading Center and the compensation of the Galápagos hotspot swell. *Earth and Planetary Science Letters*, 203, 311-327. https://doi.org/10.1016/S0012-821X(02)00843-9

Caricchi, L., Annen, C., Blundy, J., Simpson, G., & Pinel, V. (2014). Frequency and magnitude of volcanic eruptions controlled by magma injection and buoyancy. *Nature Geoscience*, 7, 126. https://doi.org/10.1038/ngeo2041

Caricchi, L., Biggs, J., Annen, C., & Ebmeier, S. (2014). The influence of cooling, crystallisation and re-melting on the interpretation of geodetic signals in volcanic systems. *Earth and Planetary Science Letters*, 388, 166-174. https://doi.org/10.1016/j.epsl.2013.12.002

Chadwick, W. W., & Howard, K. A. (1991). The pattern of circumferential and radial eruptive fissures on the volcanoes of Fernandina and Isabela islands, Galapagos. *Bulletin of Volcanology*, 53, 259-275. https://doi.org/10.1007/BF00414523

Chadwick Jr, W. W., & Dieterich, J. H. (1995). Mechanical modeling of circumferential and radial dike intrusion on Galápagos volcanoes. *Journal of Volcanology and Geothermal Research*, 66, 37-52. https://doi.org/10.1016/0377-0273(94)00060-T

Chadwick Jr, W. W., Geist, D. J., Jónsson, S., Poland, M., Johnson, D. J., & Meertens, C. M. (2006). A volcano bursting at the seams: Inflation, faulting, and eruption at Sierra Negra volcano, Galápagos. *Geology*, 34, 1025-1028. https://doi.org/10.1130/G22826A.1

Chadwick Jr, W. W., Nooner, S. L., Zumberge, M. A., Embley, R. W., & Fox, C. G. (2006). Vertical deformation monitoring at Axial Seamount since its 1998 eruption using deep-sea pressure sensors. *Journal of Volcanology and Geothermal Research*, 150, 313-327. https://doi.org/10.1016/j.jvolgeores.2005.07.006

Chadwick, W. W., Jónsson, S., Geist, D. J., Poland, M., Johnson, D. J., Batt, S., et al. (2011). The May 2005 eruption of Fernandina volcano, Galápagos: The first circumferential dike intrusion observed by GPS and InSAR. *Bulletin of Volcanology*, 73, 679-697. https://doi.org/10.1007/s00445-010-0433-0

Chiodini, G., & Frondini, F. (2001). Carbon dioxide degassing from the Albani Hills volcanic region, Central Italy. *Chemical Geology*, 177, 67-83. https://doi.org/10.1016/S0009-2541(00)00382-X

Cole, J. W., Milner, D. M., & Spinks, K. D. (2005). Calderas and caldera structures: a review. *Earth-Science Reviews*, 69, 1-26. https://doi.org/10.1016/j.earscirev.2004.06.004

Corbi, F., Rivalta, E., Pinel, V., Maccaferri, F., Bagnardi, M., & Acocella, V. (2015). How caldera collapse shapes the shallow emplacement and transfer of magma in active volcanoes. *Earth and Planetary Science Letters*, 431, 287-293. http://dx.doi.org/10.1016/j.epsl.2015.09.028

Corbi, F., Rivalta, E., Pinel, V., Maccaferri, F., & Acocella, V. (2016). Understanding the link between circumferential dikes and eruptive fissures around calderas based on numerical and analog models. *Geophysical Research Letters*, 43, 6212-6219. https://doi.org/10.1002/2016GL068721

Currier, R. M., Forsythe, P., Grossmeier, C., Laliberte, M., & Yagle, B. (2017). Experiments on the evolution of laccolith morphology in plan-view. *Journal of Volcanology and Geothermal Research*, 336, 155-167. https://doi.org/10.1016/j.jvolgeores.2017.02.017

D'Auria, L., Pepe, S., Castaldo, R., Giudicepietro, F., Macedonio, G., Ricciolino, P., et al. (2015). Magma injection beneath the urban area of Naples: a new mechanism for the 2012–2013 volcanic unrest at Campi Flegrei caldera. *Scientific reports*, 5, 13100. https://doi.org/10.1038/srep13100

Decriem, J., Árnadóttir, T., Hooper, A., Geirsson, H., Sigmundsson, F., Keiding, M. et al. (2010). The 2008 May 29 earthquake doublet in SW Iceland. *Geophysical Journal International*, 181, 1128-1146. https://doi.org/10.1111/j.1365-246X.2010.04565.x

Delgado, F., Pritchard, M., Lohman, R., & Naranjo, J. A. (2014). The 2011 Hudson volcano eruption (Southern Andes, Chile): pre-eruptive inflation and hotspots observed with InSAR and thermal imagery. *Bulletin of Volcanology*, 76, 815. https://doi.org/10.1007/s00445-014-0815-9

Degruyter, W., & Huber, C. (2014) A model for eruption frequency of upper crustal silicic magma chambers. *Earth Planet. Sci. Lett.* 403, 117-130. https://doi.org/10.1016/j.epsl.2014.06.047

Di Vito, M. A., Acocella, V., Aiello, G., Barra, D., Battaglia, M., Carandente, A., Del Gaudio, C. et al. (2016). Magma transfer at Campi Flegrei caldera (Italy) before the 1538 AD eruption. *Scientific Reports*, 6, 32245. https://doi.org/10.1038/srep32245

Duputel, Z., Agram, P.S., Simons, M., Minson, S.E. & Beck, J.L., (2014). Accounting for prediction uncertainty when inferring subsurface fault slip. *Geophysical Journal International*, 197, 464-482. https://doi.org/10.1093/gji/ggt517

Dvorak, J. J., & Dzurisin, D. (1997). Volcano geodesy: The search for magma reservoirs and the formation of eruptive vents. *Reviews of Geophysics*, 35, 343-384. https://doi.org/10.1029/97RG00070

Dzurisin, D. (2007) *Volcano deformation: new geodetic monitoring techniques*. Springer, Berlin, Heidelberg. https://doi.org/10.1007/978-3-540-49302-0

Ebmeier, S. K., Biggs, J., Mather, T. A., & Amelung, F. (2013). Applicability of InSAR to tropical volcanoes: insights from Central America. *Geological Society, London, Special Publications*, 380, 15-37. https://doi.org/10.1144/SP380.2

Ewart, J. A., Voight, B., & Björnsson, A. (1991). Elastic deformation models of Krafla Volcano, Iceland, for the decade 1975 through 1985. *Bulletin of Volcanology*, 53, 436-459. https://doi.org/10.1007/BF00258184

Farr, T. G., Rosen, P. A., Caro, E., Crippen, R., Duren, R., Hensley, S., et al. (2007). The shuttle radar topography mission. *Reviews of Geophysics*, 45. RG2004. https://doi.org/10.1029/2005RG000183

Feighner, M. A., & Richards, M. A. (1994). Lithospheric structure and compensation mechanisms of the Galápagos Archipelago. *Journal of Geophysical Research: Solid Earth*, 99, 6711-6729. https://doi.org/10.1029/93JB03360

Galetto, F., Acocella, V., & Caricchi, L., (2017) Caldera resurgence driven by magma viscosity contrasts. *Nature Communications*, 8, 1750. https://doi.org/10.1038/s41467-017-01632-y

Galetto, F., Bagnardi, M., Acocella, V., & Hooper, A. (2019) Noneruptive Unrest at the Caldera of Alcedo Volcano (Galápagos Islands) Revealed by InSAR Data and Geodetic Modeling. *Journal of Geophysical Research: Solid Earth*, 124, 3365-3381. https://doi.org/10.1029/2018JB017103

Geist, D., Howard, K. A., Jellinek, A. M., & Rayder, S. (1994). The volcanic history of Volcán Alcedo, Galápagos Archipelago: A case study of rhyolitic oceanic volcanism. *Bulletin of Volcanology*, 56, 243-260. https://doi.org/10.1007/BF00302078

Geist, D., Howard, K. A., & Larson, P. (1995). The generation of oceanic rhyolites by crystal fractionation: the basalt-rhyolite association at Volcán Alcedo, Galápagos Archipelago. *Journal of Petrology*, 36, 965-982. https://doi.org/10.1093/petrology/36.4.965

Geist, D., Chadwick, W., & Johnson, D. (2006). Results from new GPS and gravity monitoring networks at Fernandina and Sierra Negra Volcanoes, Galápagos, 2000–2002. *Journal of Volcanology and Geothermal Research*, 150, 79-97. https://doi.org/10.1016/j.jvolgeores.2005.07.003

Geist, D., Diefenbach, B. A., Fornari, D. J., Kurz, M. D., Harpp, K., & Blusztajn, J. (2008). Construction of the Galápagos platform by large submarine volcanic terraces. *Geochemistry, Geophysics, Geosystems*, 9. https://doi.org/10.1029/2007GC001795

Geist, D. J., Harpp, K. S., Naumann, T. R., Poland, M., Chadwick, W. W., Hall, M., & Rader, E. (2008). The 2005 eruption of Sierra Negra volcano, Galápagos, Ecuador. *Bulletin of Volcanology*, 70, 655-673. https://doi.org/10.1007/s00445-007-0160-3

Geist, D. J., Bergantz, G., Chadwick, W. W. Jr. (2014). Galápagos Magma Chambers. In Harpp, K. S., Mittelstaedt, E., d'Ozouville, N., & Graham, D. W. (Eds.). *The Galápagos: A Natural Laboratory for the Earth Sciences* (Vol. 204, pp 55-70). John Wiley & Sons.

Geshi, N., Shimano, T., Chiba, T., & Nakada, S. (2002). Caldera collapse during the 2000 eruption of Miyakejima Volcano, Japan. *Bulletin of Volcanology*, 64, 55-68. https://doi.org/10.1007/s00445-001-0184-z

Gibson, S. A., & Geist, D. (2010). Geochemical and geophysical estimates of lithospheric thickness variation beneath Galápagos. *Earth and Planetary Science Letters*, 300, 275-286. https://doi.org/10.1016/j.epsl.2010.10.002

Global Volcanism Program (2008). Report on Cerro Azul (Ecuador). In: Wunderman, R (ed.), Bulletin of the Global Volcanism Network, 33:5. Smithsonian Institution. https://doi.org/10.5479/si.GVP.BGVN200805-353060.

Global Volcanism Program, 2013. Volcanoes of the World, v. 4.8.3. Venzke, E (ed.). Smithsonian Institution. Downloaded 27 Sep 2019. https://doi.org/10.5479/si.GVP.VOTW4-2013

Global Volcanism Program, (2017). Report on Fernandina (Ecuador). In: Sennert, S K (ed.), Weekly Volcanic Activity Report, 6 September-12 September 2017. Smithsonian Institution and US Geological Survey.

Global Volcanism Program, (2018). Report on Fernandina (Ecuador). In: Sennert, S K (ed.), Weekly Volcanic Activity Report, 13 June-19 June 2018. Smithsonian Institution and US Geological Survey.

Goff, F., McMurtry, G. M., Counce, D., Simac, J. A., Roldán-Manzo, A. R., & Hilton, D. R. (2000). Contrasting hydrothermal activity at Sierra Negra and Alcedo volcanoes, Galápagos Archipelago, Ecuador. *Bulletin of Volcanology*, 62, 34-52. https://doi.org/10.1007/s004450050289

González, P. J., Bagnardi, M., Hooper, A. J., Larsen, Y., Marinkovic, P., Samsonov, S. V., & Wright, T. J. (2015). The 2014–2015 eruption of Fogo volcano: Geodetic modeling of Sentinel-1 TOPS interferometry. *Geophysical Research Letters*, 42, 9239-9246. https://doi.org/10.1002/2015GL066003

Gottsmann, J., Carniel, R., Coppo, N., Wooller, L., Hautmann, S., & Rymer, H. (2007). Oscillations in hydrothermal systems as a source of periodic unrest at caldera volcanoes: Multiparameter insights from Nisyros, Greece. *Geophysical Research Letters*, 34. https://doi.org/10.1029/2007GL029594

Green, J. R. (1994). Recent activity in Alcedo volcano, Isabela island. *Noticias de Galápagos*, 54, 11-12.

Gregg, P. M., Le Mével, H., Zhan, Y., Dufek, J., Geist, D., & Chadwick Jr, W. W. (2018). Stress triggering of the 2005 eruption of Sierra Negra volcano, Galápagos. *Geophysical Research Letters*, 45, 13-288. https://doi.org/10.1029/2018GL080393

Gudmundsson, M. T., Jónsdóttir, K., Hooper, A., Holohan, E. P., Halldórsson, S. A., Ófeigsson, B. G., et al. (2016). Gradual caldera collapse at Bárdarbunga volcano, Iceland, regulated by lateral magma outflow. *Science*, 353, aaf8988. http://doi.org/10.1126/science.aaf8988

Hanssen, R. F., Weckwerth, T. M., Zebker, H. A., & Klees, R. (1999). High-resolution water vapor mapping from interferometric radar measurements. *Science*, 283, 1297-1299. https://doi.org/10.1126/science.283.5406.1297

Harpp, K., & Geist, D. (2002). Wolf–Darwin lineament and plume–ridge interaction in northern Galápagos. *Geochemistry, Geophysics, Geosystems*, 3, 1-19. https://doi.org/10.1029/2002GC000370

Harpp, K., S. & Geist, D. J. (2018) The Evolution of Galápagos Volcanoes: An Alternative Prospective. *Frontiers in Earth Science*, 6:50. https://doi.org/10.3389/feart.2018.00050

Heiken, G., & McCoy Jr, F. (1984). Caldera development during the Minoan eruption, Thira, Cyclades, Greece. *Journal of Geophysical Research: Solid Earth*, 89, 8441-8462. https://doi.org/10.1029/JB089iB10p08441

Heimisson, E. R., Hooper, A., & Sigmundsson, F. (2015). Forecasting the path of a laterally propagating dike. *Journal of Geophysical Research: Solid Earth*, 120, 8774-8792. https://doi.org/10.1002/2015JB012402

Hill, D. P., Pollitz, F., & Newhall, C. (2002). Earthquake-volcano interactions. *Physics Today*, 55, 41-47. http://dx.doi.org/10.1063/1.1535006

Hill, D. P., Langbein, J. O., & Prejean, S. (2003). Relations between seismicity and deformation during unrest in Long Valley Caldera, California, from 1995 through 1999. *Journal of Volcanology and Geothermal Research*, 127, 175-193. https://doi.org/10.1016/S0377-0273(03)00169-0

Hooft, E. E., Toomey, D. R., & Solomon, S. C. (2003). Anomalously thin transition zone beneath the Galápagos hotspot. *Earth and Planetary Science Letters*, 216, 55-64. https://doi.org/10.1016/S0012-821X(03)00517-X

Hooper, A. (2008) A multi-temporal InSAR method incorporating both persistent scatterer and small baseline approaches. *Geophysical Research Letters* 35. L16302. https://doi.org/10.1029/2008GL034654

Hooper, A. (2010a). A statistical-cost approach to unwrapping the phase of InSAR time series. In *Proceedings of the International Workshop on ERS SAR Interferometry, Frascati, Italy* (Vol. 30).

Hooper, A. (2010b). Bayesian inversion of wrapped InSAR data for geophysical parameter estimation. In *ESA Living Planet Symposium* (Vol. 686).

Hooper, A., & Zebker, H. A. (2007). Phase unwrapping in three dimensions with application to InSAR time series. *J. Opt. Soc. Am. A*, 24, 2737-2747. https://doi.org/10.1364/JOSAA.24.002737

Hooper, A., Segall, P., & Zebker, H. (2007) Persistent scatterer interferometric synthetic aperture radar for crustal deformation analysis, with application to Volcán Alcedo, Galápagos. *Journal of Geophysical Research*, 112, B07407. https://doi.org/10.1029/2006JB004763

Hooper, A., Bekaert, D., Spaans, K., & Ankan, M. (2012) Recent advances in SAR interferometry time series analysis for measuring crustal deformations. *Tectonophysics* 514, 1-13. https://doi.org/10.1016/j.tecto.2011.10.013

Howard, K. A., Simkin, T., Geist, D. J., Merlen, G., & Nolf, B. (2018). Large hydromagmatic eruption related to Fernandina Volcano's 1968 caldera collapse—Deposits, landforms, and ecosystem recovery. 385-408. In Poland, M., Garcia, M. O., Camp, V. E. & Grunder, A. (Eds.) *Field*

volcanology: A tribute to the distinguished career of Don Swanson (Vol. 538, pp 385-408). Geological Society of America.

Huppert, H. E., Woods, A. W. (2002) The role of volatiles in magma chamber dynamics. *Nature* 420, 493-495. https://doi.org/10.1038/nature01211

Hurwitz, S., Christiansen, L. B. & Hsieh, P. A. (2007) Hydrothermal fluid flow and deformation in large calderas: inferences from numerical simulations. *Journal of Geophysical Research* 112, B02206. https://doi.org/10.1029/2006JB004689

Jellinek, A. M., De Paolo, D. J. (2003) A model for the origin of large silicic magma chambers: precursors of caldera-forming eruptions. *Bulletin of Volcanology* 65, 363-381. https://doi.org/10.1007/s00445-003-0277-y

Jónsson, S. (2009). Stress interaction between magma accumulation and trapdoor faulting on Sierra Negra volcano, Galápagos. *Tectonophysics*, 471, 36-44. https://doi.org/10.1016/j.tecto.2008.08.005

Jónsson, S., Zebker, H., Cervelli, P., Segall, P., Garbeil, H., Mouginis-Mark, P., & Rowland, S. (1999). A shallow-dipping dike fed the 1995 flank eruption at Fernandina Volcano, Galápagos, observed by satellite radar interferometry. *Geophysical Research Letters*, 26, 1077-1080. https://doi.org/10.1029/1999GL900108

Jónsson, S., Zebker, H., & Amelung, F. (2005). On trapdoor faulting at Sierra Negra volcano, Galapagos. *Journal of Volcanology and Geothermal Research*, 144, 59-71. https://doi.org/10.1016/j.jvolgeores.2004.11.029

Just, D., & Bamler, R. (1994). Phase statistics of interferograms with applications to synthetic aperture radar. *Applied Optics*, 33, 4361-4368. https://doi.org/10.1364/AO.33.004361

Kruskal, J. B. (1956). On the shortest spanning subtree of a graph and the traveling salesman problem. *Proceedings of the American Mathematical society*, 7, 48-50. https://www.jstor.org/stable/2033241

Le Mével, H., Gregg, P. M., & Feigl, K. L. (2016). Magma injection into a long-lived reservoir to explain geodetically measured uplift: Application to the 2007–2014 unrest episode at Laguna del Maule volcanic field, Chile. *Journal of Geophysical Research: Solid Earth*, 121, 6092-6108. https://doi.org/10.1002/2016JB013066

Leonard, M. (2010). Earthquake fault scaling: Self-consistent relating of rupture length, width, average displacement, and moment release. *Bulletin of the Seismological Society of America*, 100, 1971-1988. https://doi.org/10.1785/0120090189

Leuthold, J., Müntener, O., Baumgartner, L. P., Putlitz, B., Ovtcharova, M., & Schaltegger, U. (2012). Time resolved construction of a bimodal laccolith (Torres del Paine, Patagonia). *Earth and Planetary Science Letters*, 325, 85-92. https://doi.org/10.1016/j.epsl.2012.01.032

Lipman, P. W. (1984). The roots of ash flow calderas in western North America: windows into the tops of granitic batholiths. *Journal of Geophysical Research: Solid Earth*, 89, 8801-8841. https://doi.org/10.1029/JB089iB10p08801

Lisowski, M. (2007). Analytical volcano deformation source models. In Dzurisin, D. *Volcano deformation* (pp. 279-304). Springer, Berlin, Heidelberg. https://doi.org/10.1007/978-3-540-49302-0_8

Lu, Z., & Dzurisin, D. (2014). *InSAR Imaging of Aleutian Volcanoes: Monitoring a Volcanic Arc from Space*. Springer, Berlin, Heidelberg. https://doi.org/10.1007/978-3-642-00348-6

Lu, Z., Masterlark, T., & Dzurisin, D. (2005). Interferometric synthetic aperture radar study of Okmok volcano, Alaska, 1992–2003: Magma supply dynamics and postemplacement lava flow deformation. *Journal of Geophysical Research: Solid Earth*, 110. https://doi.org/10.1029/2004JB003148

Marsh, B. D. (1981). On the crystallinity, probability of occurrence, and rheology of lava and magma. *Contributions to Mineralogy and Petrology*, 78, 85-98. https://doi.org/10.1007/BF00371146

Massonnet, D., & Feigl, K. L. (1998). Radar interferometry and its application to changes in the Earth's surface. *Reviews of geophysics*, 36, 441-500. https://doi.org/10.1029/97RG03139

McTigue, D. F. (1987). Elastic stress and deformation near a finite spherical magma body: Resolution of the point source paradox. *Journal of Geophysical Research*, 92, 12931. https://doi.org/10.1029/JB092iB12p12931

Miller, C. F., Furbish, D. J., Walker, B. A., Claiborne, L. L., Koteas, G. C., Bleick, H. A., & Miller, J. S. (2011). Growth of plutons by incremental emplacement of sheets in crystal-rich host: Evidence from Miocene intrusions of the Colorado River region, Nevada, USA. *Tectonophysics*, 500, 65-77. https://doi.org/10.1016/j.tecto.2009.07.011

Mittal, T., & Richards, M. A. (2017). Plume-ridge interaction via melt channelization at Galápagos and other near-ridge hotspot provinces. *Geochemistry, Geophysics, Geosystems*, 18, 1711-1738. https://doi.org/10.1002/2016GC006454

Mittelstaedt, E., Soule, S., Harpp, K., Fornari, D., McKee, C., Tivey, M., et al. (2012). Multiple expressions of plume-ridge interaction in the Galápagos: Volcanic lineaments and ridge jumps. *Geochemistry, Geophysics, Geosystems*, 13. https://doi.org/10.1029/2012GC004093

Mogi, K. (1958) Relations between the eruptions of various volcanoes and the deformations of the ground surfaces around them. *Bulletin of the Earthquake Research Institute* 36, 99-134.

Moran, S. C., Newhall, C., & Roman, D. C. (2011). Failed magmatic eruptions: late-stage cessation of magma ascent. *Bulletin of Volcanology*, 73, 115-122. https://doi.org/10.1007/s00445-010-0444-x

Mouginis-Mark, P. J., Rowland, S. K., & Garbeil, H. (1996). Slopes of western Galápagos volcanoes from airborne interferometric radar. *Geophysical Research Letters*, 23, 3767-3770. https://doi.org/10.1029/96GL03280

Mouginis-Mark, P. J., Snell, H., & Ellisor, R. (2000). GOES satellite and field observations of the 1998 eruption of Volcan Cerro Azul, Galapagos Islands. *Bulletin of Volcanology*, 62, 188-198. https://doi.org/10.1007/s004450000078

Munro, D. C., & Rowland, S. K. (1996). Caldera morphology in the western Galápagos and implications for volcano eruptive behavior and mechanisms of caldera formation. *Journal of Volcanology and Geothermal Research*, 72, 85-100. https://doi.org/10.1016/0377-0273(95)00076-3

Naumann, T. R., & Geist, D. J. (1999). Generation of alkalic basalt by crystal fractionation of tholeiitic magma. *Geology*, 27, 423-426. https://doi.org/10.1130/0091-7613(1999)027<0423:GOABBC>2.3.CO;2

Naumann, T., & Geist, D. (2000). Physical volcanology and structural development of Cerro Azul Volcano, Isabela Island, Galápagos: implications for the development of Galápagos-type shield volcanoes. *Bulletin of Volcanology*, 61, 497-514. https://doi.org/10.1007/s004450050001

Naumann, T., Geist, D., & Kurz, M. (2002). Petrology and geochemistry of Volcán Cerro Azul: Petrologic diversity among the western Galapagos volcanoes. *Journal of Petrology*, 43, 859-883. https://doi.org/10.1093/petrology/43.5.859

Newhall, C. G., Dzurisin, D. (1988) *Historical unrest at large calderas of the world*. (Vol. 2). U.S. Geol. Surv. Bull., 1855, 1108.

Newman, A. V., Dixon, T. H., & Gourmelen, N. (2006). A four-dimensional viscoelastic deformation model for Long Valley Caldera, California, between 1995 and 2000. *Journal of Volcanology and Geothermal Research*, 150, 244-269. https://doi.org/10.1016/j.jvolgeores.2005.07.017

Nikkhoo, M., Walter, T. R., Lundgren, P. R. & Prats-Iraola, P. (2017). Compound dislocation models (CDMs) for volcano deformation analyses. *Geophysical Journal International* 208, 877 - 894. https://doi.org/10.1093/gji/ggw427

Nooner, S. L., & Chadwick Jr, W. W. (2009). Volcanic inflation measured in the caldera of Axial Seamount: Implications for magma supply and future eruptions. *Geochemistry, Geophysics, Geosystems*, 10. https://doi.org/10.1029/2008GC002315

Nooner, S. L., & Chadwick, W. W. (2016). Inflation-predictable behavior and co-eruption deformation at Axial Seamount. *Science*, 354, 1399-1403. https://doi.org/10.1126/science.aah4666

Nordlie, B. E. (1973). Morphology and structure of the western Galápagos volcanoes and a model for their origin. *Geological Society of America Bulletin*, 84, 2931-2956. https://doi.org/10.1130/0016-7606(1973)84<2931:MASOTW>2.0.CO;2

Okada, Y. (1985). Surface deformation due to shear and tensile faults in a half-space. *Bulletin of the seismological society of America*, 75, 1135-1154.

Pedersen, R., & Sigmundsson, F. (2004). InSAR based sill model links spatially offset areas of deformation and seismicity for the 1994 unrest episode at Eyjafjallajökull volcano, Iceland. *Geophysical Research Letters*, 31. https://doi.org/10.1029/2004GL020368

Pedersen, R., & Sigmundsson, F. (2006). Temporal development of the 1999 intrusive episode in the Eyjafjallajökull volcano, Iceland, derived from InSAR images. *Bulletin of Volcanology*, 68, 377-393. https://doi.org/10.1007/s00445-005-0020-y

Pinel, V., Poland, M. P., & Hooper, A. (2014). Volcanology: Lessons learned from synthetic aperture radar imagery. *Journal of Volcanology and Geothermal Research*, 289, 81-113. https://doi.org/10.1016/j.jvolgeores.2014.10.010

Poland, M. P. (2014) Contrasting volcanism in Hawaiʻi and the Galápagos. In Harpp, K. S., Mittelstaedt, E., d'Ozouville, N., & Graham, D. W. (Eds.). *The Galápagos: A Natural Laboratory for the Earth Sciences* (Vol. 204, pp 5-26). John Wiley & Sons.

Poland, M. P., Miklius, A., & Montgomery-Brown, E. K. (2014). Magma supply, storage, and transport at shield-stage. In Poland, M. P., Takahashi, T. J., & Landowski, C. M. *Characteristics of Hawaiian Volcanoes*, (pp.179-234). USGS Professional Paper 1801. https://doi.org/10.3133/pp18015

Poland, M. P., Lisowski, M., Dzurisin, D., Kramer, R., McLay, M., & Pauk, B. (2017). Volcano geodesy in the Cascade arc, USA. *Bulletin of Volcanology*, 79, 59. https://doi.org/10.1007/s00445-017-1140-x

Prim, R. C. (1957). Shortest connection networks and some generalizations. *The Bell System Technical Journal*, 36(6), 1389-1401. https://doi.org/10.1002/j.1538-7305.1957.tb01515.x

Pritchard, M. E., & Simons, M. (2004). An InSAR-based survey of volcanic deformation in the southern Andes. *Geophysical Research Letters*, 31. https://doi.org/10.1029/2004GL020545

Rivalta, E. (2010). Evidence that coupling to magma chambers controls the volume history and velocity of laterally propagating intrusions. *Journal of Geophysical Research: Solid Earth*, 115, B07203. https://doi.org/10.1029/2009JB006922

Rivalta, E., & Segall, P. (2008). Magma compressibility and the missing source for some dike intrusions. *Geophysical Research Letters*, 35. https://doi.org/10.1029/2007GL032521

Rivalta, E., Taisne, B., Bunger, A. P., & Katz, R. F. (2015). A review of mechanical models of dike propagation: Schools of thought, results and future directions. *Tectonophysics*, 638, 1-42. https://doi.org/10.1016/j.tecto.2014.10.003

Robertson, R. M., & Kilburn, C. R. (2016). Deformation regime and long-term precursors to eruption at large calderas: Rabaul, Papua New Guinea. *Earth and Planetary Science Letters*, 438, 86-94. https://doi.org/10.1016/j.epsl.2016.01.003

Rosen, P. A., Gurrola, E., Sacco, G. F., & Zebker, H. (2012). The InSAR scientific computing environment. In *Synthetic Aperture Radar, 2012. EUSAR. 9th European Conference on*, pp. 730-733. VDE.

Rowland, S. K., Harris, A. J., Wooster, M. J., Amelung, F., Garbeil, H., Wilson, L., & Mouginis-Mark, P. J. (2003). Volumetric characteristics of lava flows from interferometric radar and

multispectral satellite data: the 1995 Fernandina and 1998 Cerro Azul eruptions in the western Galapagos. *Bulletin of Volcanology*, 65, 311-330. https://doi.org/10.1007/s00445-002-0262-x

Rubin, A. M. (1995). Propagation of magma-filled cracks. *Annual Review of Earth and Planetary Sciences*, 23, 287-336. https://doi.org/10.1146/annurev.ea.23.050195.001443

Rychert, C. A., Harmon, N., & Ebinger, C. (2014). Receiver function imaging of lithospheric structure and the onset of melting beneath the Galápagos Archipelago. *Earth and Planetary Science Letters*, 388, 156-165. http://dx.doi.org/10.1016/j.epsl.2013.11.027

Sandri, L., Acocella, V., & Newhall, C. (2017). Searching for patterns in caldera unrest. Geochemistry, Geophysics, Geosystems, 18, 2748‐2768. https://doi.org/10.1002/2017GC006870

Sigmundsson, F., Hooper, A., Hreinsdóttir, S., Vogfjörd, K. S., Ófeigsson, B. G., Heimisson, E. R., et al. (2015). Segmented lateral dyke growth in a rifting event at Bárðarbunga volcanic system, Iceland. *Nature*, 517, 191. https://doi.org/10.1038/nature14111

Sigmundsson, F., Hreinsdóttir, S., Hooper, A., Árnadóttir, T., Pedersen, R., Roberts, M. J., et al. (2010). Intrusion triggering of the 2010 Eyjafjallajökull explosive eruption. *Nature*, 468, 426. https://doi.org/10.1038/nature09558

Sparks, R. S. J., Annen, C., Blundy, J. D., Cashman, K. V., Rust, A. C., & Jackson, M. D. (2019). Formation and dynamics of magma reservoirs. *Philosophical Transactions of the Royal Society A*, 377, 20180019. https://doi.org/10.1098/rsta.2018.0019

Stephens, T. L., Walker, R. J., Healy, D., Bubeck, A., England, R. W., & McCaffrey, K. J. (2017). Igneous sills record far-field and near-field stress interactions during volcano construction: Isle of Mull, Scotland. *Earth and Planetary Science Letters*, 478, 159-174. https://doi.org/10.1016/j.epsl.2017.09.003

Stix, J., & Kobayashi, T. (2008). Magma dynamics and collapse mechanisms during four historic caldera-forming events. *Journal of Geophysical Research: Solid Earth*, 113. https://doi.org/10.1029/2007JB005073

Stock, M. J., Bagnardi, M., Neave, D. A., Maclennan, J., Bernard, B., Buisman, I., et al. (2018). Integrated petrological and geophysical constraints on magma system architecture in the western Galápagos Archipelago: insights from Wolf volcano. *Geochemistry, Geophysics, Geosystems*. 19. https://doi.org/10.1029/2018GC007936

Teasdale, R., Geist, D., Kurz, M., & Harpp, K. (2005). 1998 Eruption at Volcán Cerro Azul, Galápagos Islands: I. Syn-Eruptive Petrogenesis. *Bulletin of Volcanology*, 67, 170-185. https://doi.org/10.1007/s00445-004-0371-9

Thomson, K., & Hutton, D. (2004). Geometry and growth of sill complexes: insights using 3D seismic from the North Rockall Trough. *Bulletin of Volcanology*, 66, 364-375. https://doi.org/10.1007/s00445-003-0320-z

Tramontano, S., Gualda, G. A., & Ghiorso, M. S. (2017). Internal triggering of volcanic eruptions: Tracking overpressure regimes for giant magma bodies. *Earth and Planetary Science Letters*, 472, 142-151. https://doi.org/10.1016/j.epsl.2017.05.014

Urbani, S., Acocella, V., Rivalta, E., & Corbi, F. (2017). Propagation and arrest of dikes under topography: Models applied to the 2014 Bardarbunga (Iceland) rifting event. *Geophysical Research Letters*, 44, 6692-6701. https://doi.org/10.1002/2017GL073130

Villagómez, D. R., Toomey, D. R., Geist, D. J., Hooft, E. E., & Solomon, S. C. (2014). Mantle flow and multistage melting beneath the Galápagos hotspot revealed by seismic imaging. *Nature Geoscience*, 7, 151-156. https://doi.org/10.1038/NGEO2062

Voight, B., Widiwijayanti, C., Mattioli, G., Elsworth, D., Hidayat, D., Strutt, M. (2010). Magma-sponge hypothesis and stratovolcanoes: Case for a compressible reservoir and quasi-steady deep influx at Soufrière Hills Volcano, Montserrat. *Geophysical Research Letters* 37, L00E05, https://doi.org/10.1029/2009GL041732

Walter, T. R. (2003). Buttressing and fractional spreading of Tenerife, an experimental approach on the formation of rift zones. *Geophysical Research Letters*, 30. https://doi.org/10.1029/2002GL016610

Walter, T. R., Klügel, A., & Münn, S. (2006). Gravitational spreading and formation of new rift zones on overlapping volcanoes. *Terra Nova*, 18, 26-33. https://doi.org/10.1111/j.1365-3121.2005.00656.x

Werner, R., Hoernle, K., Barckhausen, U., & Hauff, F. (2003). Geodynamic evolution of the Galápagos hot spot system (Central East Pacific) over the past 20 my: Constraints from morphology, geochemistry, and magnetic anomalies. *Geochemistry, Geophysics, Geosystems*, 4. https://doi.org/10.1029/2003GC000576

White, W. M., McBirney, A. R., & Duncan, R. A. (1993). Petrology and geochemistry of the Galápagos Islands: Portrait of a pathological mantle plume. *Journal of Geophysical Research: Solid Earth*, 98, 19533-19563. https://doi.org/10.1029/93JB02018

Wilson, D. S., & Hey, R. N. (1995). History of rift propagation and magnetization intensity for the Cocos-Nazca spreading Center. *Journal of Geophysical Research: Solid Earth*, 100, 10041-10056. https://doi.org/10.1029/95JB00762

Woods, A. W., & Koyaguchi, T. (1994). Transitions between explosive and effusive eruptions of silicic magmas. *Nature*, 370, 641. https://doi.org/10.1038/370641a0

Wright, T. J., Parsons, B. E., Lu, Z. (2004). Toward mapping surface deformation in three dimensions using InSAR. *Geophysical Research Letters* 31, L01607, https://doi.org/10.1029/2003GL018827

Wright, T. J., Ebinger, C., Biggs, J., Ayele, A., Yirgu, G., Keir, D., & Stork, A. (2006). Magma-maintained rift segmentation at continental rupture in the 2005 Afar dyking episode. *Nature*, 442, 291. https://doi.org/10.1038/nature04978

Yang, X. M., Davis, P. M., & Dieterich, J. H. (1988). Deformation from inflation of a dipping finite prolate spheroid in an elastic half - space as a model for volcanic stressing. *Journal of Geophysical Research: Solid Earth*, 93, 4249-4257. https://doi.org/10.1029/JB093iB05p04249

Yun, S., Segall, P., & Zebker, H. (2006). Constraints on magma chamber geometry at Sierra Negra Volcano, Galápagos Islands, based on InSAR observations. *Journal of Volcanology and Geothermal Research*, 150, 232-243. https://doi.org/10.1016/j.jvolgeores.2005.07.009

Xu, W., Jónsson, S., Ruch, J., & Aoki, Y. (2016). The 2015 Wolf volcano (Galápagos) eruption studied using Sentinel-1 and ALOS-2 data. *Geophysical Research Letters*, 43, 9573-9580. https://doi.org/10.1002/2016GL069820

Supporting information file for Chapter 2

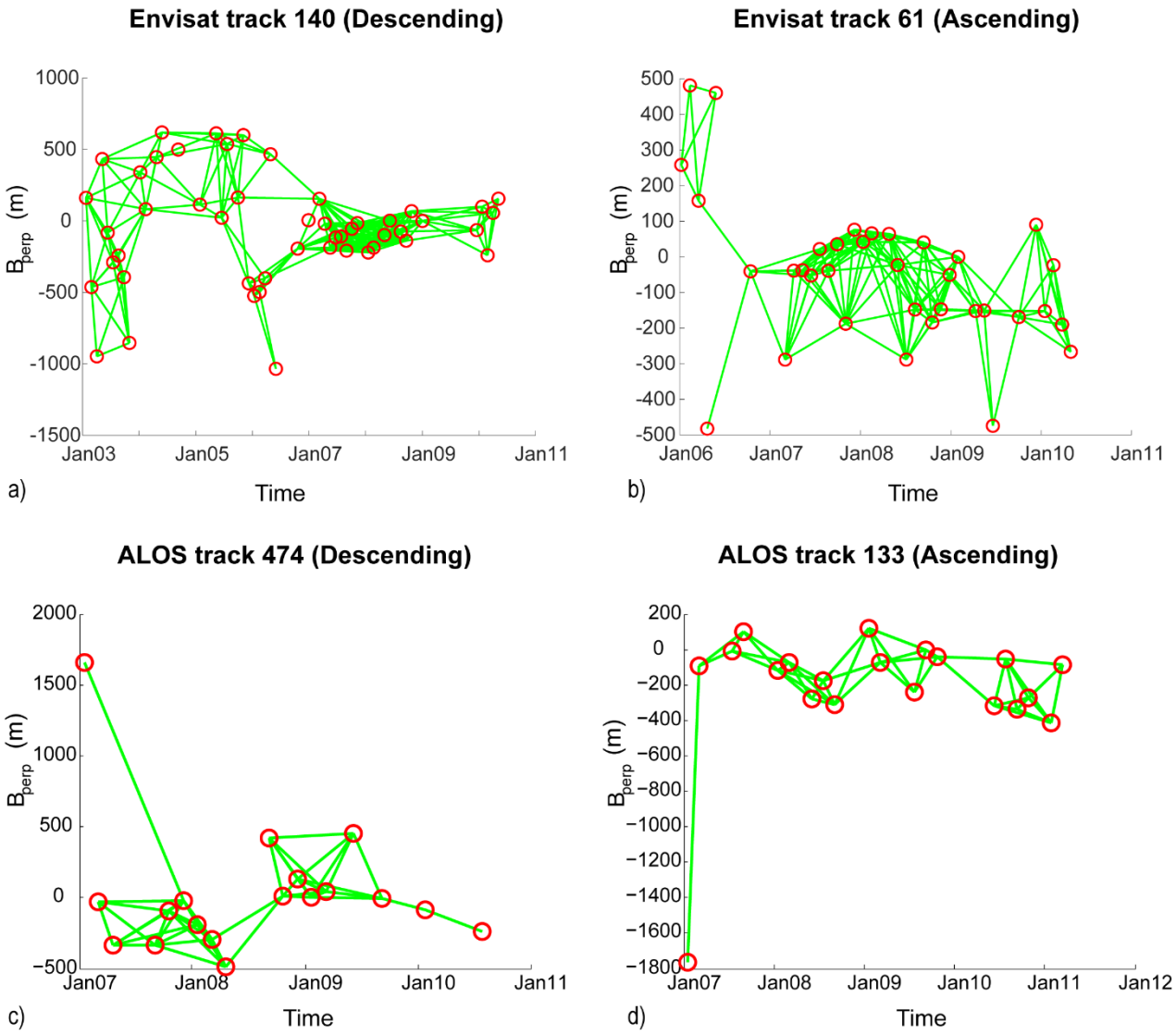

Figure S1. Networks of interferograms generated for the Small Baselines analysis plotted as function of acquisition date and perpendicular baseline. Red circles represent SAR images, while the green lines are the SB interferograms. a) The 221 SB interferograms created from the 48 T140 ENVISAT SAR images. b) The 154 SB interferograms created from the 35 T61 ENVISAT SAR images. **c)** The 46 SB interferograms created from the 18 T474 ALOS SAR images. **d)** The 47 SB interferograms created from the 20 T133 SAR images.

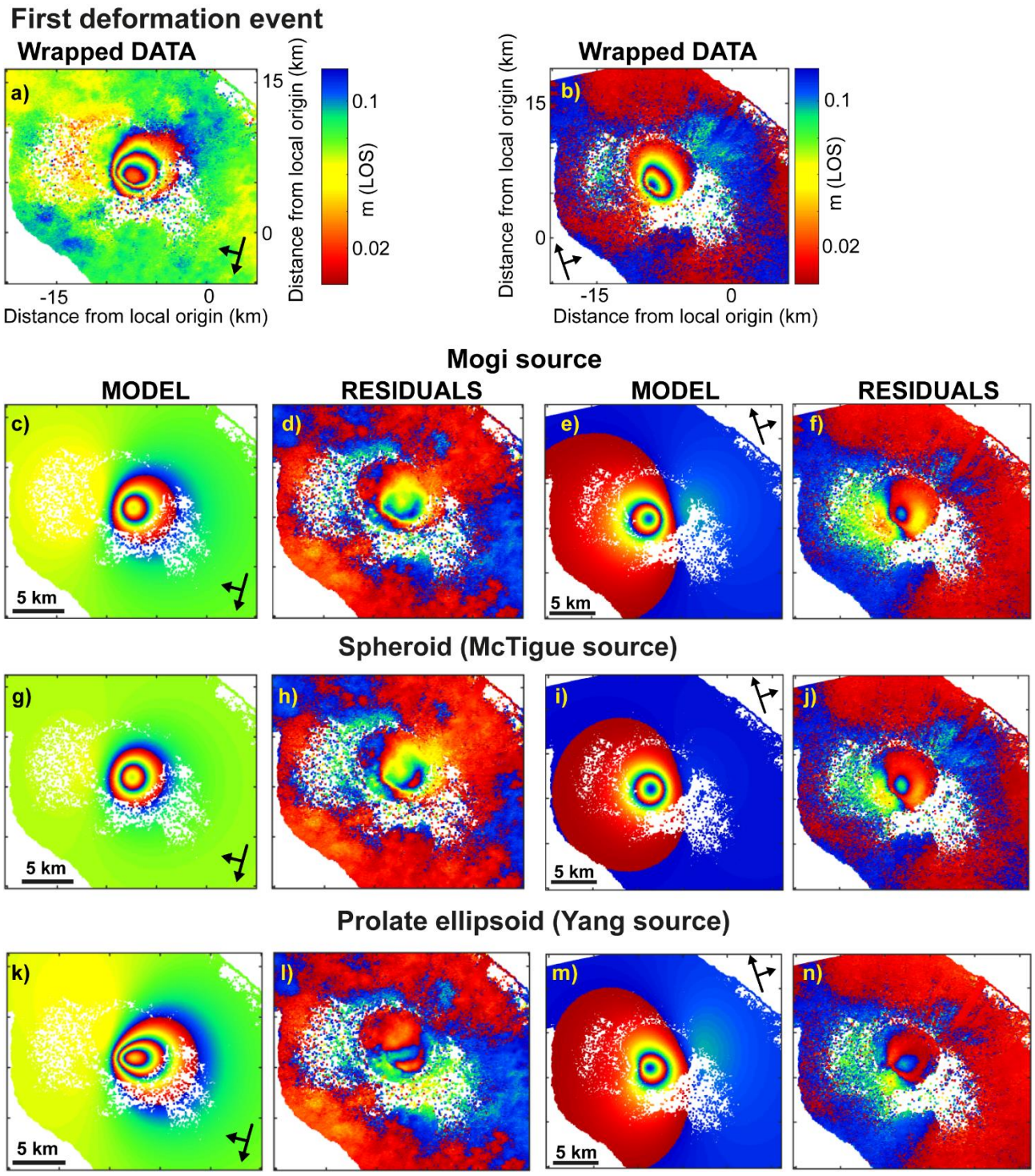

Figure S2 a) Wrapped ALOS-1 LOS displacements for descending track 474 (January 2007 - January 2010), and b) for ascending track 133 (January 2007 - October 2009). Local origin coordinates: Lon 91°05'W and Lat 0°49'S. c,e) Predicted displacements for the point source model, using the maximum a posteriori probability solution, and d,f) the related residuals. g,i) Predicted displacements for the spheroid model using the maximum a posteriori probability solution, and h,j) the related residuals. k,m) Predicted displacements for the prolate ellipsoid model using the maximum a

posteriori probability, and l-n) the related residuals. In all figures, each fringe (full colour cycle) represents 11.8 cm of LOS displacement.

Table S1. Results from the Bayesian analyses of the first event using different sources.

Point source (Mogi source)								
	X (m)	**Y (m)**	**Depth (m)**	**ΔV x10^6 (m^3)**				
Optimal	-8076	6044	2251	6.04				
2.50%	-8114	6005	2189	5.63				
97.50%	-8030	6082	2312	6.48				
Lower	-10000	1000	1500	0.1				
Upper	3000	9000	6000	200				
Finite sphere (McTigue source)								
	X (m)	**Y (m)**	**Depth (m)**	**Radius (m)**	**DP/mu**			
Optimal	-8086	6033	2938	4997	4.57 x10^{-6}			
2.50%	-8123	5995	2867	4455	4.35 x10^{-6}			
97.50%	-8041	6068	3006	4997	8.33 x10^{-6}			
Lower	-10000	3000	1600	2000	0			
Upper	-4000	8000	4000	5000	1 x 10^{-3}			
Prolate ellipsoid (Yang source)								
	X (m)	**Y (m)**	**Depth (m)**	**Ax (m)**	**a/r**	**strike**	**Plunge**	**DP/mu**
Optimal	-7531	6111	2354	2802	0.06	87	34	0.03
2.50%	-7607	6065	2251	2675	0.01	85	32	0.04
97.50%	-7436	6149	2419	2915	0.05	90	35	0.6
Lower	-10000	2000	2000	500	0.01	1	0.1	0
Upper	-5000	9000	4000	5000	0.99	359	89	2

Optimal solutions are from the maximum a posteriori probability solutions (Figure S2). 2.50% and 97.50% are the lower and upper bounds of the 95% credible intervals. Lower and Upper bounds define the prior distribution used for the inversion. X and Y are the local coordinates of the centroid of each source. Local origin coordinates: Lon 91°05'W and Lat 0°49'S. Depths are with respect to the caldera floor (positive downward). ΔV is the volume change. DP/mu is dimensionless excess pressure (pressure change/shear modulus). Ax is the length of the major semi-axis of the ellipsoid. a/r is the dimensionless aspect ratio between semi-axes (minor/major). Strike is the strike angle of Ax. Plunge is the inclination angle of Ax.

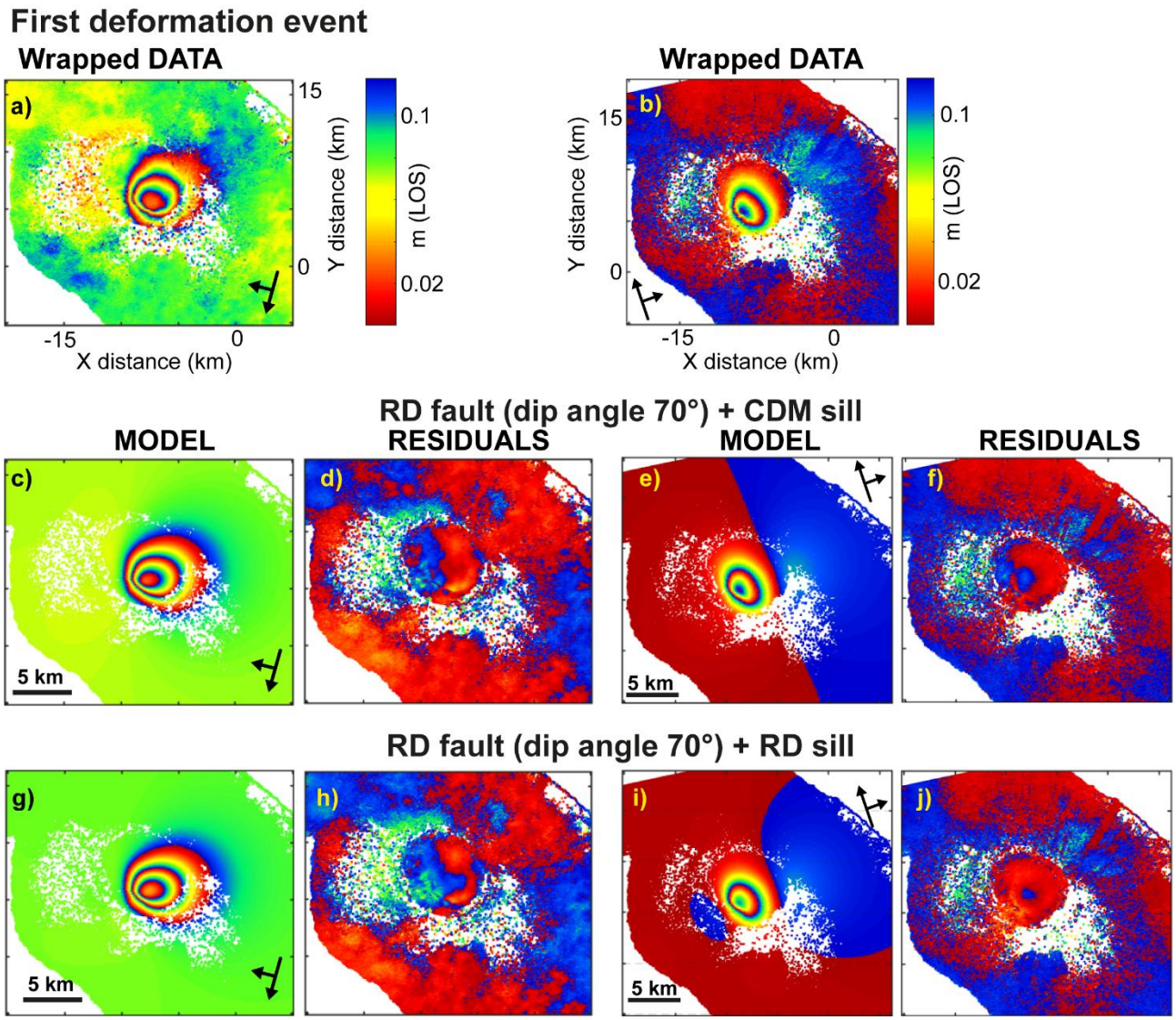

Figure S3. a) Wrapped ALOS-1 LOS displacements for descending track 474 (January 2007 - January 2010), and b) for ascending track 133 (January 2007 - October 2009). Local origin coordinates: Lon 91°05'W and Lat 0°49'S. c,e) Predicted displacements for the RD fault (dip angle 70°)+ CDM sill model, using the maximum a posteriori probability solution, and d,f) the related residuals. g,i) Predicted displacements for the RD fault (dip angle 70°) + RD sill model using the maximum a posteriori probability solution, and h,j) the related residuals.

Table S2. Optimal = maximum a posteriori probability solution. 2.50% and 97.50% are the lower and upper boundaries of the 95% credible intervals.

First event (RD fault + CDM sill)											
						Fault (Dip angle 70°)					
	X (m)	**Y (m)**	**Z (m)**	**L (m)**	**W (m)**	**Dip[a]**	**Strike**	**Rake[a]**	**Slip (m)**		
Optimal	-8954	5165	992	1577	839	70	121	-90	0.45		
2.50%	-9000	5089	857	1393	446	70	117	-90	0.33		
97.50%	-8861	5238	1062	1747	986	70	125	-90	0.75		
Lower	-10000	4000	700	800	400	70	90	-90	0.1		
Upper	-5000	6000	1600	2900	1000	70	180	-90	2		
						CDM sill					
	X (m)	**Y (m)**	**Z (m)**	**ω X**	**ω Y**	**ω Z**	**ax (m)**	**ay (m)**	**az (m)**	**Op. (m)**	**ΔV (x10^6 m^3)**
Optimal	-7832	5917	2100	-21	-17	272	1559	1914	199	0.58	8.6
2.50%	-7887	5842	2011	-23	-20	268	1439	1850	145	0.54	7.8
97.50%	-7743	5973	2243	-19	-14	275	1625	2018	273	0.66	9.7
Lower	-10000	3000	2000	-50	-40	180	800	800	4	0	
Upper	-5000	8000	4000	0	0	360	4000	4000	500	10	
First event (RD fault + RD sill)											
						Fault (Dip angle70°)					
	X (m)	**Y (m)**	**Z (m)**	**L (m)**	**W (m)**	**Dip[a]**	**Strike**	**Rake[a]**	**Slip (m)**		
Optimal	-8916	5128	865	1542	591	70	120	-90	0.49		
2.50%	-8968	5054	786	1394	411	70	118	-90	0.31		
97.50%	-8854	5175	965	1706	926	70	124	-90	0.69		
Lower	-10000	4000	710	800	400	70	90	-90	0.1		
Upper	-5000	6000	1600	2900	950	70	180	-90	2		
						RD sill					
	X (m)	**Y (m)**	**Z (m)**	**L (m)**	**W (m)**	**θ**	**Dip**	**Strike**	**Op. (m)**	**ΔV (x10^6 m^3)**	
Optimal	-7852	5875	2117	3082	3953	32	27	331	0.59	7.3	
2.50%	-7934	5808	2037	2935	3782	28	25	326	0.56	6.8	
97.50%	-7801	5917	2281	3217	4074	38	30	334	0.68	8.1	
Lower	-11000	2000	2000	800	800	0	0	240	0		
Upper	-5000	8000	4000	4400	4500	50	50	360	2		

X and Y are the local coordinates of the centre of CDM and the centre of the RD fault. Lower and Upper define the bounds of the prior distribution used for the inversion. Local coordinates origin (see Fig. 4a and b): Lon 91° 05' W and Lat 0° 49' S. Z is the depth (with respect to the caldera floor) (positive downward). ωZ is the strike angle, ω X and ω Y are respectively the rotational angle along the X and Y direction. ax, ay and az are the lengths of the semi-axes of the CDM along the x, y, and z axes, respectively (see Nikkhoo et al., 2017 for details). Op. is the opening. L is the length, while W is its width. Rake is the rake of the fault and strike is its strike angle. Dip is the dip angle of the fault. Volume change (ΔV) has been calculated with the formula ΔV=4*(opening)*[(ax*ay)+(ay*az)+(ax*az)] (Nikkhoo et al., 2017).

[a] Parameter held fixed.

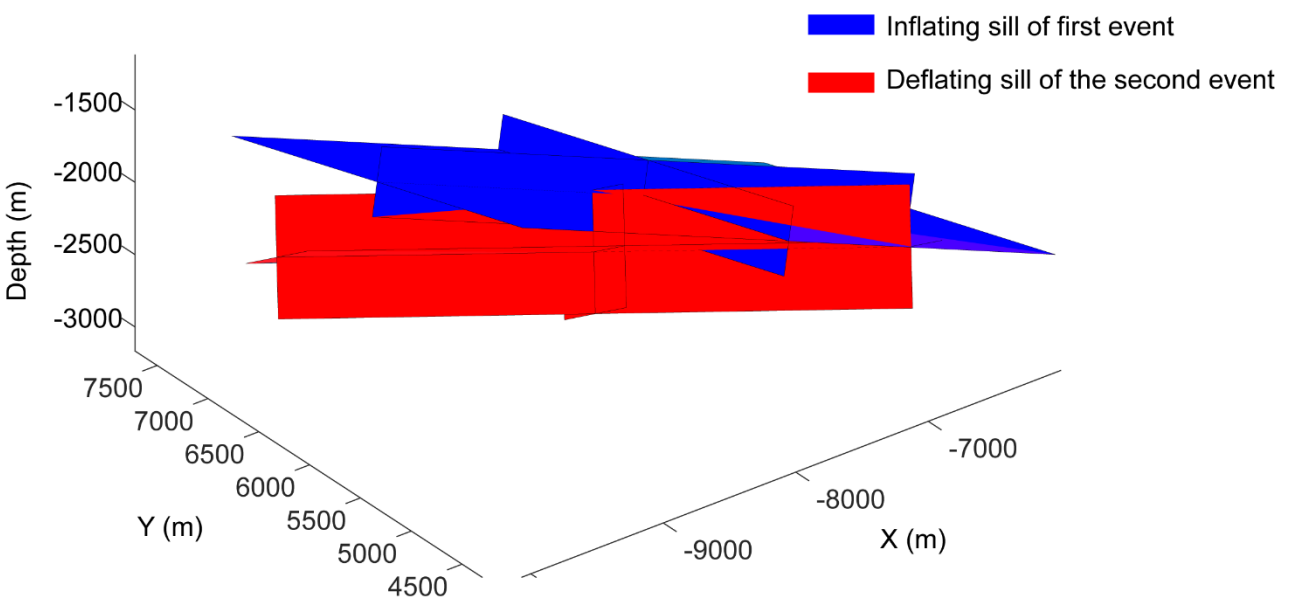

Figure S4. Three-dimensional representation of the sub-caldera CDM sources. The blue CDM is the source inflated during the first deformation event and the red one is the CDM deflated during the second event. Source parameters are from the maximum a posteriori probability solution (for the first deformation event we used the CDM of the CDM + fault solution). X and Y are the distance (in meters) with respect to the local reference point (Lon. 91°05'W and Lat. 0°49'S, see Fig. 4). Depth is with respect to the caldera floor.

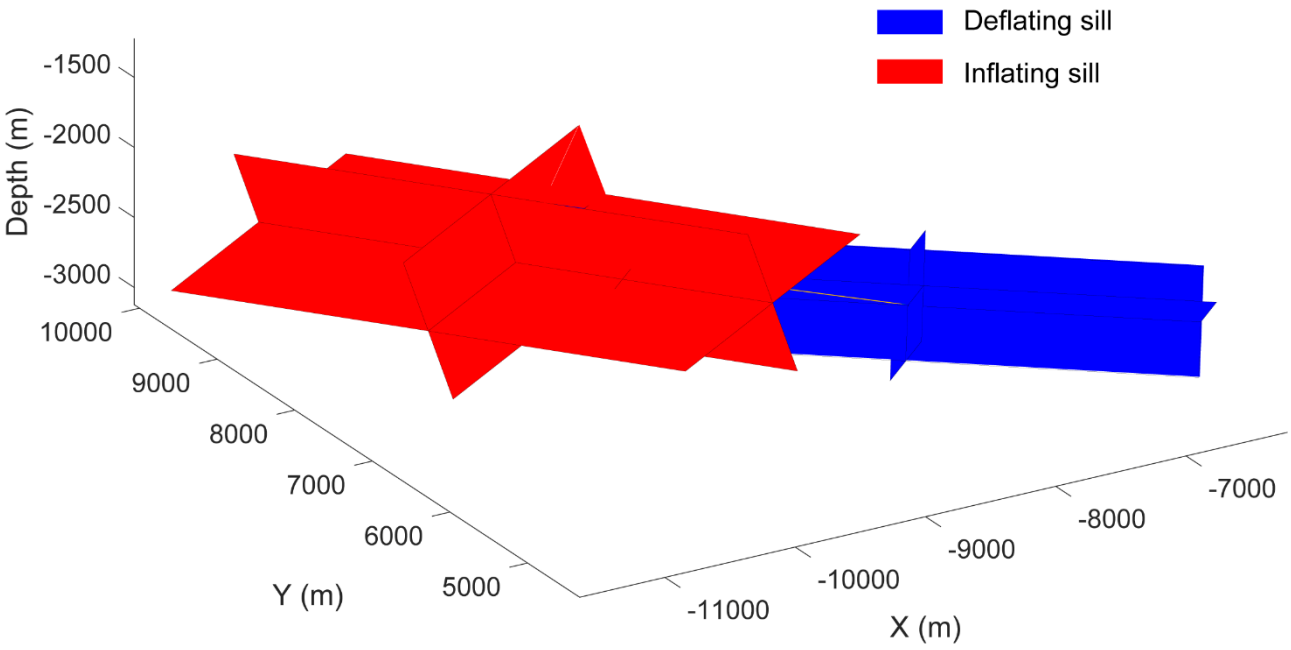

Figure S5. Three-dimensional representation of the two CDM sills that caused the second deformation event. Source parameters are from the maximum a posteriori probability solution. X and Y are the distance (in meters) with respect to the local reference point (Lon 91°05'W and Lat 0°49'S, see Fig. 5). Depth is with respect to the caldera floor.

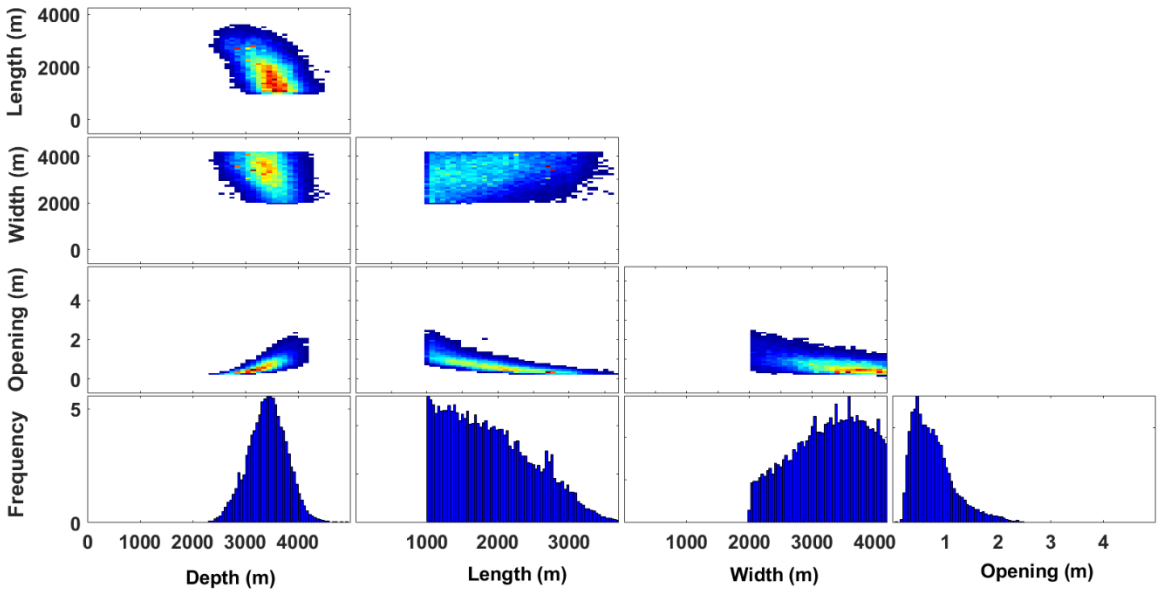

Figure S6 Marginal posterior probability distributions of the three parameters on which the ΔV depends (length, width and opening) and the depth of the RD source used for modelling the third deformation event (Fig. 6, Tab. 3).

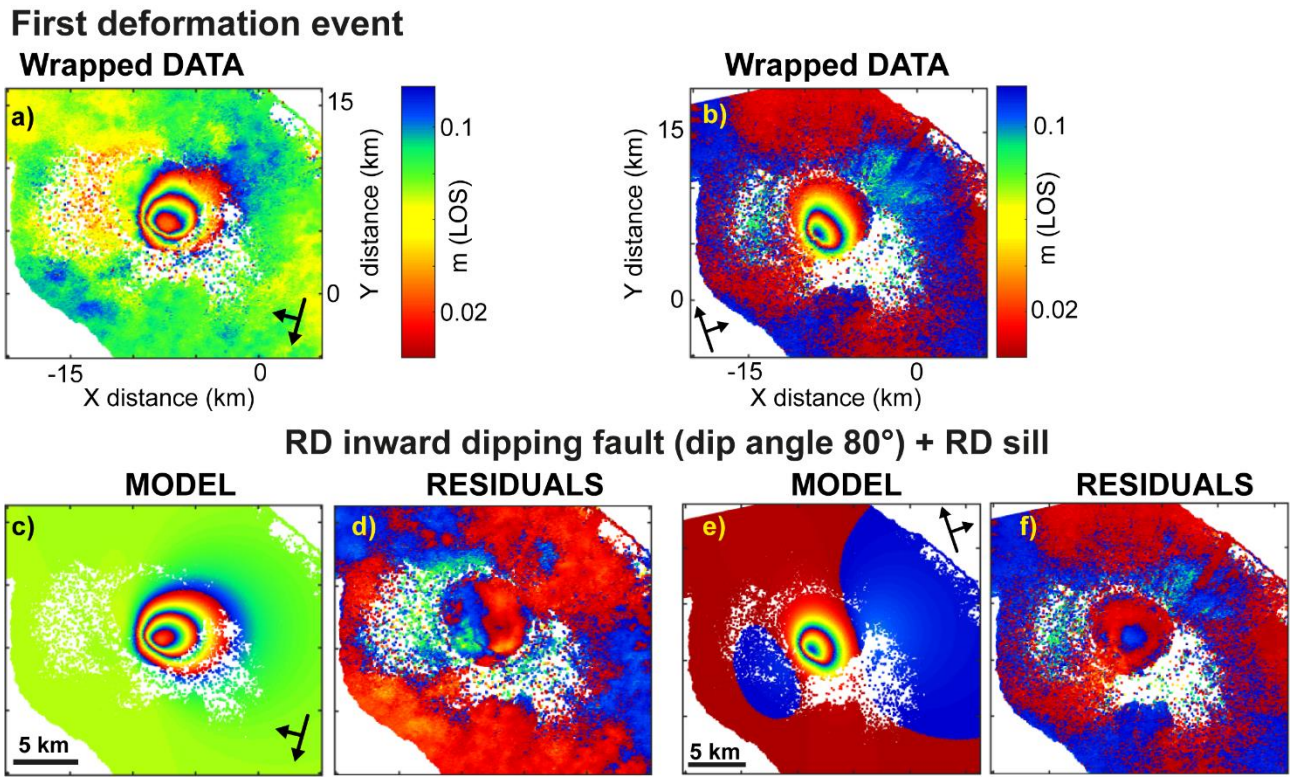

Figure S7. a) Wrapped ALOS-1 LOS displacements for descending track 474 (January 2007 - January 2010), and b) for ascending track 133 (January 2007 - October 2009). Local origin coordinates: Lon 91°05'W and Lat 0°49'S. c,e) Predicted displacements for the RD fault + RD sill model, using the maximum a posteriori probability solution, and d,f) the related residuals.

RD sill										
	X (m)	**Y (m)**	**Z (m)**	**L (m)**	**W (m)**	**θ**	**Dip**	**Strike**	**Op. (m)**	**ΔV (x10^6 m^3)**
Optimal	-7844	5938	2335	3062	3982	33	25	338	0.62	7.5
2.50%	-8021	5795	2215	2598	3760	26	24	332	0.56	6.8
97.50%	-7799	5980	2596	3222	4101	42	33	343	0.86	8.7
Lower	-11000	2000	2000	800	800	-50	0	240	0	
Upper	-5000	8000	4000	4400	4400	50	50	360	10	

RD fault									
	X (m)	**Y (m)**	**Z (m)**	**L (m)**	**W (m)**	**Dip[a]**	**Strike**	**Rake[a]**	**Slip (m)**
Optimal	-8733	5407	881	2169	502	80	307	90	0.45
2.50%	-8788	5347	748	1998	409	80	304	90	0.23
97.50%	-8644	5474	988	2373	856	80	310	90	0.56
Lower	-10000	4000	700	800	400	80	270	90	0.1
Upper	-5000	6000	1600	2800	950	80	360	90	2

Table S3. Optimal = maximum a posteriori probability solution. 2.50% and 97.50% are the lower and upper boundaries of the 95% credible intervals. Lower and Upper are the bounds of the prior distribution used for the inversion. X and Y are the local coordinates of the centre of RD. Local origin coordinates (see Fig. 4a and b): Lon 91° 05’ W and Lat 0° 49’ S. Z is the depth (with respect to the caldera floor) (positive downward). θ is the angle between the RD upper edge and the intersection of the RD plane with the free surface. L and W are respectively the length and the width. Rake is the rake of the fault. Op. is the opening. Dip is the dip angle. Strike is the strike angle (see Nikkhoo et al., 2017 for a better explanation of all these parameters). ΔV is the volume change calculated with the formula ΔV=L*W*Op.

[a] Parameter held fixed.

Supplementary information table for Chapter 3

Table S1 *List of the network of interferograms used for the Small Baselines analysis.*

ENVISAT ascending track 61	**ENVISAT ascending track 61**	**ENVISAT descending track 140**	**ENVISAT descending track 140**	**ALOS-1 ascending track 133**	**ALOS-1 ascending track 133**	**ALOS-1 descending track 474**	**ALOS-1 descending track 474**
Small baseline interferogrmas	*Perpendicular baseline*	*Small baseline interferograms*	*Perpendicular baseline*	*Small baseline interferograms*	*Perpendicular baseline*	*Small baseline interferograms*	*Perpendicular baseline*
07-Jan-2006 to 11-Feb-2006	223 m	23-Jan-2003 to 27-Feb-2003	-625 m	02-Mar-2007 to 18-Jul-2007	87 m	03-Mar-2007 to 18-Apr-2007	-300 m
07-Jan-2006 to 18-Mar-2006	-101 m	23-Jan-2003 to 08-May-2003	272 m	18-Jul-2007 to 18-Jan-2008	-109 m	03-Mar-2007 to 03-Sep-2007	-303 m
07-Jan-2006 to 27-May-2006	202 m	23-Jan-2003 to 12-Jun-2003	-243 m	18-Jul-2007 to 04-Mar-2008	-65 m	03-Mar-2007 to 19-Oct-2007	-62 m
11-Feb-2006 to 18-Mar-2006	-324 m	23-Jan-2003 to 17-Jul-2003	-451 m	18-Jan-2008 to 04-Mar-2008	45 m	03-Mar-2007 to 04-Dec-2007	12 m
11-Feb-2006 to 27-May-2006	-21 m	23-Jan-2003 to 21-Aug-2003	-404 m	18-Jan-2008 to 04-Jun-2008	-165 m	18-Apr-2007 to 03-Sep-2007	-3 m
18-Mar-2006 to 27-May-2006	303 m	23-Jan-2003 to 08-Jan-2004	179 m	18-Jan-2008 to 20-Jul-2008	-62 m	18-Apr-2007 to 19-Oct-2007	238 m
18-Mar-2006 to 14-Oct-2006	-198 m	23-Jan-2003 to 12-Feb-2004	-79 m	18-Jan-2008 to 04-Sep-2008	-193 m	18-Apr-2007 to 04-Dec-2007	313 m
22-Apr-2006 to 14-Oct-2006	442 m	27-Feb-2003 to 03-Apr-2003	-484 m	04-Mar-2008 to 04-Jun-2008	-210 m	18-Apr-2007 to 19-Jan-2008	142 m
14-Oct-2006 to 03-Mar-2007	-248 m	27-Feb-2003 to 12-Jun-2003	381 m	04-Mar-2008 to 20-Jul-2008	-106 m	03-Sep-2007 to 19-Oct-2007	241 m
14-Oct-2006 to 12-May-2007	3 m	27-Feb-2003 to 17-Jul-2003	173 m	04-Mar-2008 to 04-Sep-2008	-238 m	03-Sep-2007 to 04-Dec-2007	315 m
14-Oct-2006 to 16-Jun-2007	-12 m	27-Feb-2003 to 21-Aug-2003	221 m	04-Jun-2008 to 20-Jul-2008	104 m	03-Sep-2007 to 19-Jan-2008	145 m
14-Oct-2006 to 21-Jul-2007	63 m	27-Feb-2003 to 25-Sep-2003	69 m	04-Jun-2008 to 04-Sep-2008	-28 m	03-Sep-2007 to 05-Mar-2008	39 m
03-Mar-2007 to 12-May-2007	251 m	27-Feb-2003 to 30-Oct-2003	-390 m	20-Jul-2008 to 04-Sep-2008	-131 m	03-Sep-2007 to 20-Apr-2008	-152 m
03-Mar-2007 to 16-Jun-2007	236 m	03-Apr-2003 to 30-Oct-2003	94 m	20-Jul-2008 to 07-Mar-2009	107 m	19-Oct-2007 to 04-Dec-2007	75 m
03-Mar-2007 to 21-Jul-2007	311 m	08-May-2003 to 12-Jun-2003	-515 m	04-Sep-2008 to 07-Mar-2009	238 m	19-Oct-2007 to 19-Jan-2008	-96 m
03-Mar-2007 to 25-Aug-2007	249 m	08-May-2003 to 08-Jan-2004	-93 m	07-Mar-2009 to 23-Jul-2009	-167 m	19-Oct-2007 to 05-Mar-2008	-201 m
ENVISAT ascending track 61	**ENVISAT ascending track 61**	**ENVISAT descending track 140**	**ENVISAT descending track 140**	**ALOS-1 ascending track 133**	**ALOS-1 ascending track 133**	**ALOS-1 descending track 474**	**ALOS-1 descending track 474**

Small baseline interferogrmas	*Perpendicular baseline*	*Small baseline interferograms*	*Perpendicular baseline*	*Small baseline interferograms*	*Perpendicular baseline*	*Small baseline interferograms*	*Perpendicular baseline*
03-Mar-2007 to 03-Nov-2007	101 m	08-May-2003 to 12-Feb-2004	-351 m	07-Mar-2009 to 07-Sep-2009	71 m	19-Oct-2007 to 20-Apr-2008	-393 m
12-May-2007 to 16-Jun-2007	-15 m	08-May-2003 to 22-Apr-2004	14 m	07-Mar-2009 to 23-Oct-2009	30 m	04-Dec-2007 to 19-Jan-2008	-170 m
12-May-2007 to 21-Jul-2007	59 m	12-Jun-2003 to 17-Jul-2003	-208 m	23-Jul-2009 to 07-Sep-2009	238 m	04-Dec-2007 to 05-Mar-2008	-276 m
12-May-2007 to 25-Aug-2007	-2 m	12-Jun-2003 to 21-Aug-2003	-161 m	23-Jul-2009 to 23-Oct-2009	196 m	04-Dec-2007 to 20-Apr-2008	-467 m
12-May-2007 to 03-Nov-2007	-150 m	12-Jun-2003 to 25-Sep-2003	-312 m	07-Sep-2009 to 23-Oct-2009	-42 m	19-Jan-2008 to 05-Mar-2008	-106 m
12-May-2007 to 08-Dec-2007	114 m	12-Jun-2003 to 08-Jan-2004	422 m	23-Oct-2009 to 10-Jun-2010	-278 m	19-Jan-2008 to 20-Apr-2008	-297 m
12-May-2007 to 12-Jan-2008	79 m	12-Jun-2003 to 12-Feb-2004	164 m	23-Oct-2009 to 26-Jul-2010	-10 m	05-Mar-2008 to 20-Apr-2008	-191 m
16-Jun-2007 to 21-Jul-2007	74 m	17-Jul-2003 to 21-Aug-2003	48 m	10-Jun-2010 to 26-Jul-2010	268 m	05-Mar-2008 to 21-Oct-2008	310 m
16-Jun-2007 to 25-Aug-2007	13 m	17-Jul-2003 to 25-Sep-2003	-104 m	10-Jun-2010 to 10-Sep-2010	-20 m	20-Apr-2008 to 21-Oct-2008	502 m
16-Jun-2007 to 03-Nov-2007	-135 m	17-Jul-2003 to 30-Oct-2003	-563 m	10-Jun-2010 to 26-Oct-2010	47 m	05-Sep-2008 to 21-Oct-2008	-408 m
16-Jun-2007 to 08-Dec-2007	129 m	17-Jul-2003 to 12-Feb-2004	372 m	10-Jun-2010 to 26-Jan-2011	-97 m	05-Sep-2008 to 06-Dec-2008	-292 m
16-Jun-2007 to 12-Jan-2008	94 m	21-Aug-2003 to 25-Sep-2003	-151 m	26-Jul-2010 to 10-Sep-2010	-287 m	05-Sep-2008 to 21-Jan-2009	-422 m
16-Jun-2007 to 16-Feb-2008	119 m	21-Aug-2003 to 30-Oct-2003	-611 m	26-Jul-2010 to 26-Oct-2010	-221 m	05-Sep-2008 to 08-Mar-2009	-376 m
21-Jul-2007 to 25-Aug-2007	-61 m	21-Aug-2003 to 12-Feb-2004	324 m	26-Jul-2010 to 26-Jan-2011	-364 m	21-Oct-2008 to 06-Dec-2008	116 m
21-Jul-2007 to 03-Nov-2007	-210 m	25-Sep-2003 to 30-Oct-2003	-460 m	26-Jul-2010 to 13-Mar-2011	-33 m	21-Oct-2008 to 21-Jan-2009	-14 m
21-Jul-2007 to 08-Dec-2007	54 m	25-Sep-2003 to 12-Feb-2004	476 m	10-Sep-2010 to 26-Oct-2010	66 m	21-Oct-2008 to 08-Mar-2009	32 m
21-Jul-2007 to 12-Jan-2008	20 m	08-Jan-2004 to 12-Feb-2004	-258 m	10-Sep-2010 to 26-Jan-2011	-77 m	06-Dec-2008 to 21-Jan-2009	-130 m
21-Jul-2007 to 16-Feb-2008	44 m	08-Jan-2004 to 22-Apr-2004	106 m	10-Sep-2010 to 13-Mar-2011	254 m	06-Dec-2008 to 08-Mar-2009	-84 m
21-Jul-2007 to 26-Apr-2008	42 m	08-Jan-2004 to 27-May-2004	279 m	26-Oct-2010 to 26-Jan-2011	-143 m	06-Dec-2008 to 08-Sep-2009	-134 m
ENVISAT ascending track 61	**ENVISAT ascending track 61**	**ENVISAT descending track 140**	**ENVISAT descending track 140**	**ALOS-1 ascending track 133**	**ALOS-1 ascending track 133**	**ALOS-1 descending track 474**	**ALOS-1 descending track 474**
Small baseline interferogrmas	*Perpendicular baseline*	*Small baseline interferograms*	*Perpendicular baseline*	*Small baseline interferograms*	*Perpendicular baseline*	*Small baseline interferograms*	*Perpendicular baseline*

25-Aug-2007 to 03-Nov-2007	-149 m	12-Feb-2004 to 22-Apr-2004	364 m	26-Oct-2010 to 13-Mar-2011	188 m	21-Jan-2009 to 08-Mar-2009	46 m
25-Aug-2007 to 08-Dec-2007	115 m	12-Feb-2004 to 27-May-2004	537 m	26-Jan-2011 to 13-Mar-2011	331 m	21-Jan-2009 to 08-Sep-2009	-4 m
25-Aug-2007 to 12-Jan-2008	81 m	12-Feb-2004 to 27-Jan-2005	32 m			08-Mar-2009 to 08-Sep-2009	-49 m
25-Aug-2007 to 16-Feb-2008	105 m	22-Apr-2004 to 27-May-2004	173 m			08-Sep-2009 to 24-Jan-2010	-80 m
25-Aug-2007 to 26-Apr-2008	104 m	22-Apr-2004 to 27-Jan-2005	-332 m			24-Jan-2010 to 27-Jul-2010	-154 m
25-Aug-2007 to 31-May-2008	16 m	22-Apr-2004 to 12-May-2005	166 m				
03-Nov-2007 to 08-Dec-2007	264 m	27-May-2004 to 12-May-2005	-6 m				
03-Nov-2007 to 12-Jan-2008	230 m	27-Jan-2005 to 12-May-2005	499 m				
03-Nov-2007 to 16-Feb-2008	254 m	27-Jan-2005 to 16-Jun-2005	-92 m				
03-Nov-2007 to 26-Apr-2008	252 m	27-Jan-2005 to 21-Jul-2005	424 m				
03-Nov-2007 to 31-May-2008	165 m	27-Jan-2005 to 29-Sep-2005	50 m				
03-Nov-2007 to 05-Jul-2008	-101 m	12-May-2005 to 16-Jun-2005	-591 m				
03-Nov-2007 to 09-Aug-2008	40 m	12-May-2005 to 21-Jul-2005	-75 m				
08-Dec-2007 to 12-Jan-2008	-34 m	12-May-2005 to 29-Sep-2005	-449 m				
08-Dec-2007 to 16-Feb-2008	-10 m	12-May-2005 to 03-Nov-2005	-12 m				
08-Dec-2007 to 26-Apr-2008	-12 m	12-May-2005 to 27-Apr-2006	-146 m				
08-Dec-2007 to 31-May-2008	-99 m	16-Jun-2005 to 21-Jul-2005	516 m				
08-Dec-2007 to 13-Sep-2008	-36 m	16-Jun-2005 to 29-Sep-2005	142 m				
12-Jan-2008 to 16-Feb-2008	24 m	16-Jun-2005 to 08-Dec-2005	-459 m				

ENVISAT ascending track 61	**ENVISAT ascending track 61**	**ENVISAT descending track 140**	**ENVISAT descending track 140**	**ALOS-1 ascending track 133**	**ALOS-1 ascending track 133**	**ALOS-1 descending track 474**	**ALOS-1 descending track 474**
Small baseline interferogrmas	*Perpendicular baseline*	*Small baseline interferograms*	*Perpendicular baseline*	*Small baseline interferograms*	*Perpendicular baseline*	*Small baseline interferograms*	*Perpendicular baseline*
12-Jan-2008 to 26-Apr-2008	22 m	21-Jul-2005 to 29-Sep-2005	-375 m				

12-Jan-2008 to 31-May-2008	-65 m	21-Jul-2005 to 03-Nov-2005	62 m				
12-Jan-2008 to 05-Jul-2008	-330 m	21-Jul-2005 to 27-Apr-2006	-72 m				
12-Jan-2008 to 09-Aug-2008	-190 m	29-Sep-2005 to 03-Nov-2005	437 m				
12-Jan-2008 to 13-Sep-2008	-1 m	29-Sep-2005 to 08-Dec-2005	-600 m				
16-Feb-2008 to 26-Apr-2008	-2 m	29-Sep-2005 to 27-Apr-2006	303 m				
16-Feb-2008 to 31-May-2008	-89 m	03-Nov-2005 to 27-Apr-2006	-134 m				
16-Feb-2008 to 05-Jul-2008	-355 m	08-Dec-2005 to 12-Jan-2006	-88 m				
16-Feb-2008 to 09-Aug-2008	-214 m	08-Dec-2005 to 16-Feb-2006	-61 m				
16-Feb-2008 to 13-Sep-2008	-26 m	08-Dec-2005 to 23-Mar-2006	35 m				
26-Apr-2008 to 31-May-2008	-87 m	08-Dec-2005 to 19-Oct-2006	243 m				
26-Apr-2008 to 05-Jul-2008	-353 m	12-Jan-2006 to 16-Feb-2006	27 m				
26-Apr-2008 to 09-Aug-2008	-212 m	12-Jan-2006 to 23-Mar-2006	123 m				
26-Apr-2008 to 13-Sep-2008	-24 m	12-Jan-2006 to 01-Jun-2006	-510 m				
26-Apr-2008 to 18-Oct-2008	-249 m	12-Jan-2006 to 19-Oct-2006	331 m				
26-Apr-2008 to 22-Nov-2008	-212 m	16-Feb-2006 to 23-Mar-2006	96 m				
26-Apr-2008 to 27-Dec-2008	-115 m	16-Feb-2006 to 01-Jun-2006	-537 m				
26-Apr-2008 to 31-Jan-2009	-64 m	16-Feb-2006 to 19-Oct-2006	304 m				
31-May-2008 to 05-Jul-2008	-266 m	23-Mar-2006 to 19-Oct-2006	208 m				
ENVISAT ascending track 61	**ENVISAT ascending track 61**	**ENVISAT descending track 140**	**ENVISAT descending track 140**	**ALOS-1 ascending track 133**	**ALOS-1 ascending track 133**	**ALOS-1 descending track 474**	**ALOS-1 descending track 474**
Small baseline interferogrmas	*Perpendicular baseline*	*Small baseline interferograms*	*Perpendicular baseline*	*Small baseline interferograms*	*Perpendicular baseline*	*Small baseline interferograms*	*Perpendicular baseline*
31-May-2008 to 09-Aug-2008	-125 m	27-Apr-2006 to 08-Mar-2007	-312 m				
31-May-2008 to 13-Sep-2008	63 m	19-Oct-2006 to 08-Mar-2007	349 m				

31-May-2008 to 18-Oct-2008	-161 m	19-Oct-2006 to 12-Apr-2007	174 m				
31-May-2008 to 22-Nov-2008	-124 m	19-Oct-2006 to 17-May-2007	7 m				
31-May-2008 to 27-Dec-2008	-28 m	19-Oct-2006 to 21-Jun-2007	78 m				
31-May-2008 to 31-Jan-2009	23 m	19-Oct-2006 to 26-Jul-2007	85 m				
05-Jul-2008 to 09-Aug-2008	141 m	19-Oct-2006 to 30-Aug-2007	-14 m				
05-Jul-2008 to 13-Sep-2008	329 m	19-Oct-2006 to 04-Oct-2007	139 m				
05-Jul-2008 to 18-Oct-2008	104 m	08-Mar-2007 to 12-Apr-2007	-175 m				
05-Jul-2008 to 22-Nov-2008	141 m	08-Mar-2007 to 17-May-2007	-342 m				
05-Jul-2008 to 27-Dec-2008	238 m	08-Mar-2007 to 21-Jun-2007	-271 m				
09-Aug-2008 to 13-Sep-2008	188 m	08-Mar-2007 to 26-Jul-2007	-264 m				
09-Aug-2008 to 18-Oct-2008	-36 m	08-Mar-2007 to 30-Aug-2007	-363 m				
09-Aug-2008 to 22-Nov-2008	1 m	08-Mar-2007 to 04-Oct-2007	-210 m				
09-Aug-2008 to 27-Dec-2008	97 m	08-Mar-2007 to 08-Nov-2007	-170 m				
09-Aug-2008 to 31-Jan-2009	148 m	12-Apr-2007 to 17-May-2007	-167 m				
09-Aug-2008 to 16-May-2009	-3 m	12-Apr-2007 to 21-Jun-2007	-96 m				
13-Sep-2008 to 18-Oct-2008	-225 m	12-Apr-2007 to 26-Jul-2007	-89 m				
13-Sep-2008 to 22-Nov-2008	-188 m	12-Apr-2007 to 30-Aug-2007	-188 m				
ENVISAT ascending track 61	**ENVISAT ascending track 61**	**ENVISAT descending track 140**	**ENVISAT descending track 140**	**ALOS-1 ascending track 133**	**ALOS-1 ascending track 133**	**ALOS-1 descending track 474**	**ALOS-1 descending track 474**
Small baseline interferogrmas	*Perpendicular baseline*	*Small baseline interferograms*	*Perpendicular baseline*	*Small baseline interferograms*	*Perpendicular baseline*	*Small baseline interferograms*	*Perpendicular baseline*
13-Sep-2008 to 27-Dec-2008	-91 m	12-Apr-2007 to 04-Oct-2007	-35 m				
13-Sep-2008 to 31-Jan-2009	-40 m	12-Apr-2007 to 08-Nov-2007	4 m				
18-Oct-2008 to 22-Nov-2008	37 m	12-Apr-2007 to 17-Jan-2008	-201 m				

18-Oct-2008 to 27-Dec-2008	133 m	12-Apr-2007 to 21-Feb-2008	-167 m
18-Oct-2008 to 31-Jan-2009	184 m	12-Apr-2007 to 01-May-2008	-79 m
18-Oct-2008 to 16-May-2009	33 m	12-Apr-2007 to 05-Jun-2008	21 m
22-Nov-2008 to 27-Dec-2008	96 m	17-May-2007 to 21-Jun-2007	71 m
22-Nov-2008 to 31-Jan-2009	147 m	17-May-2007 to 26-Jul-2007	78 m
22-Nov-2008 to 16-May-2009	-4 m	17-May-2007 to 30-Aug-2007	-21 m
27-Dec-2008 to 31-Jan-2009	51 m	17-May-2007 to 04-Oct-2007	132 m
27-Dec-2008 to 16-May-2009	-100 m	17-May-2007 to 08-Nov-2007	171 m
31-Jan-2009 to 16-May-2009	-151 m	17-May-2007 to 17-Jan-2008	-34 m
31-Jan-2009 to 03-Oct-2009	-169 m	17-May-2007 to 21-Feb-2008	0 m
16-May-2009 to 20-Jun-2009	-324 m	17-May-2007 to 01-May-2008	88 m
16-May-2009 to 03-Oct-2009	-18 m	21-Jun-2007 to 26-Jul-2007	7 m
16-May-2009 to 12-Dec-2009	241 m	21-Jun-2007 to 30-Aug-2007	-92 m
16-May-2009 to 16-Jan-2010	-2 m	21-Jun-2007 to 04-Oct-2007	61 m
20-Jun-2009 to 03-Oct-2009	305 m	21-Jun-2007 to 08-Nov-2007	101 m
03-Oct-2009 to 12-Dec-2009	259 m	21-Jun-2007 to 17-Jan-2008	-105 m
03-Oct-2009 to 16-Jan-2010	17 m	21-Jun-2007 to 21-Feb-2008	-71 m
03-Oct-2009 to 20-Feb-2010	146 m	21-Jun-2007 to 01-May-2008	17 m
03-Oct-2009 to 27-Mar-2010	-21 m	21-Jun-2007 to 05-Jun-2008	118 m
03-Oct-2009 to 01-May-2010	-97 m	21-Jun-2007 to 14-Aug-2008	42 m

ENVISAT ascending track 61	**ENVISAT ascending track 61**	**ENVISAT descending track 140**	**ENVISAT descending track 140**	**ALOS-1 ascending track 133**	**ALOS-1 ascending track 133**	**ALOS-1 descending track 474**	**ALOS-1 descending track 474**
Small baseline interferogrmas	*Perpendicular baseline*	*Small baseline interferograms*	*Perpendicular baseline*	*Small baseline interferograms*	*Perpendicular baseline*	*Small baseline interferograms*	*Perpendicular baseline*

12-Dec-2009 to 16-Jan-2010	-243 m	26-Jul-2007 to 30-Aug-2007	-100 m				
12-Dec-2009 to 20-Feb-2010	-114 m	26-Jul-2007 to 04-Oct-2007	53 m				
12-Dec-2009 to 27-Mar-2010	-280 m	26-Jul-2007 to 08-Nov-2007	93 m				
12-Dec-2009 to 01-May-2010	-357 m	26-Jul-2007 to 17-Jan-2008	-112 m				
16-Jan-2010 to 20-Feb-2010	129 m	26-Jul-2007 to 21-Feb-2008	-78 m				
16-Jan-2010 to 27-Mar-2010	-38 m	26-Jul-2007 to 01-May-2008	10 m				
16-Jan-2010 to 01-May-2010	-114 m	26-Jul-2007 to 05-Jun-2008	110 m				
20-Feb-2010 to 27-Mar-2010	-167 m	26-Jul-2007 to 14-Aug-2008	34 m				
20-Feb-2010 to 01-May-2010	-243 m	26-Jul-2007 to 18-Sep-2008	-30 m				
27-Mar-2010 to 01-May-2010	-76 m	30-Aug-2007 to 04-Oct-2007	153 m				
		30-Aug-2007 to 08-Nov-2007	193 m				
		30-Aug-2007 to 17-Jan-2008	-13 m				
		30-Aug-2007 to 21-Feb-2008	21 m				
		30-Aug-2007 to 01-May-2008	109 m				
		30-Aug-2007 to 05-Jun-2008	210 m				
ENVISAT ascending track 61	**ENVISAT ascending track 61**	**ENVISAT descending track 140**	**ENVISAT descending track 140**	**ALOS-1 ascending track 133**	**ALOS-1 ascending track 133**	**ALOS-1 descending track 474**	**ALOS-1 descending track 474**
Small baseline interferogrmas	*Perpendicular baseline*	*Small baseline interferograms*	*Perpendicular baseline*	*Small baseline interferograms*	*Perpendicular baseline*	*Small baseline interferograms*	*Perpendicular baseline*
		30-Aug-2007 to 14-Aug-2008	134 m				
		30-Aug-2007 to 18-Sep-2008	70 m				
		04-Oct-2007 to 08-Nov-2007	40 m				
		04-Oct-2007 to 17-Jan-2008	-166 m				
		04-Oct-2007 to 21-Feb-2008	-132 m				

		04-Oct-2007 to 01-May-2008	-43 m				
		04-Oct-2007 to 05-Jun-2008	57 m				
		04-Oct-2007 to 14-Aug-2008	-19 m				
		04-Oct-2007 to 18-Sep-2008	-83 m				
		04-Oct-2007 to 23-Oct-2008	123 m				
		08-Nov-2007 to 17-Jan-2008	-206 m				
		08-Nov-2007 to 21-Feb-2008	-172 m				
		08-Nov-2007 to 01-May-2008	-83 m				
		08-Nov-2007 to 05-Jun-2008	17 m				
		08-Nov-2007 to 14-Aug-2008	-59 m				
		08-Nov-2007 to 18-Sep-2008	-123 m				
		08-Nov-2007 to 23-Oct-2008	83 m				
		08-Nov-2007 to 01-Jan-2009	15 m				
		17-Jan-2008 to 21-Feb-2008	34 m				
ENVISAT ascending track 61	**ENVISAT ascending track 61**	**ENVISAT descending track 140**	**ENVISAT descending track 140**	**ALOS-1 ascending track 133**	**ALOS-1 ascending track 133**	**ALOS-1 descending track 474**	**ALOS-1 descending track 474**
Small baseline interferogrmas	*Perpendicular baseline*	*Small baseline interferograms*	*Perpendicular baseline*	*Small baseline interferograms*	*Perpendicular baseline*	*Small baseline interferograms*	*Perpendicular baseline*
		17-Jan-2008 to 01-May-2008	122 m				
		17-Jan-2008 to 05-Jun-2008	223 m				
		17-Jan-2008 to 14-Aug-2008	147 m				
		17-Jan-2008 to 18-Sep-2008	82 m				
		17-Jan-2008 to 23-Oct-2008	289 m				
		17-Jan-2008 to 01-Jan-2009	221 m				

		21-Feb-2008 to 01-May-2008	88 m				
		21-Feb-2008 to 05-Jun-2008	189 m				
		21-Feb-2008 to 14-Aug-2008	113 m				
		21-Feb-2008 to 18-Sep-2008	48 m				
		21-Feb-2008 to 23-Oct-2008	255 m				
		21-Feb-2008 to 01-Jan-2009	187 m				
		01-May-2008 to 05-Jun-2008	100 m				
		01-May-2008 to 14-Aug-2008	24 m				
		01-May-2008 to 18-Sep-2008	-40 m				
		01-May-2008 to 23-Oct-2008	167 m				
		01-May-2008 to 01-Jan-2009	98 m				
		05-Jun-2008 to 14-Aug-2008	-76 m				
		05-Jun-2008 to 18-Sep-2008	-140 m				
ENVISAT ascending track 61	**ENVISAT ascending track 61**	**ENVISAT descending track 140**	**ENVISAT descending track 140**	**ALOS-1 ascending track 133**	**ALOS-1 ascending track 133**	**ALOS-1 descending track 474**	**ALOS-1 descending track 474**
Small baseline interferogrmas	*Perpendicular baseline*	*Small baseline interferograms*	*Perpendicular baseline*	*Small baseline interferograms*	*Perpendicular baseline*	*Small baseline interferograms*	*Perpendicular baseline*
		05-Jun-2008 to 23-Oct-2008	66 m				
		05-Jun-2008 to 01-Jan-2009	-2 m				
		14-Aug-2008 to 18-Sep-2008	-64 m				
		14-Aug-2008 to 23-Oct-2008	142 m				
		14-Aug-2008 to 01-Jan-2009	74 m				
		18-Sep-2008 to 23-Oct-2008	207 m				
		18-Sep-2008 to 01-Jan-2009	138 m				

		23-Oct-2008 to 01-Jan-2009	-68 m				
		01-Jan-2009 to 17-Dec-2009	-64 m				
		01-Jan-2009 to 21-Jan-2010	100 m				
		17-Dec-2009 to 21-Jan-2010	164 m				
		17-Dec-2009 to 25-Feb-2010	-176 m				
		17-Dec-2009 to 01-Apr-2010	120 m				
		17-Dec-2009 to 06-May-2010	220 m				
		21-Jan-2010 to 25-Feb-2010	-340 m				
		21-Jan-2010 to 01-Apr-2010	-44 m				
		21-Jan-2010 to 06-May-2010	56 m				
		25-Feb-2010 to 01-Apr-2010	297 m				
		25-Feb-2010 to 06-May-2010	396 m				
ENVISAT ascending track 61	**ENVISAT ascending track 61**	**ENVISAT descending track 140**	**ENVISAT descending track 140**	**ALOS-1 ascending track 133**	**ALOS-1 ascending track 133**	**ALOS-1 descending track 474**	**ALOS-1 descending track 474**
Small baseline interferogrmas	*Perpendicular baseline*	*Small baseline interferograms*	*Perpendicular baseline*	*Small baseline interferograms*	*Perpendicular baseline*	*Small baseline interferograms*	*Perpendicular baseline*
		01-Apr-2010 to 06-May-2010	99 m				

Synthetic data

Results

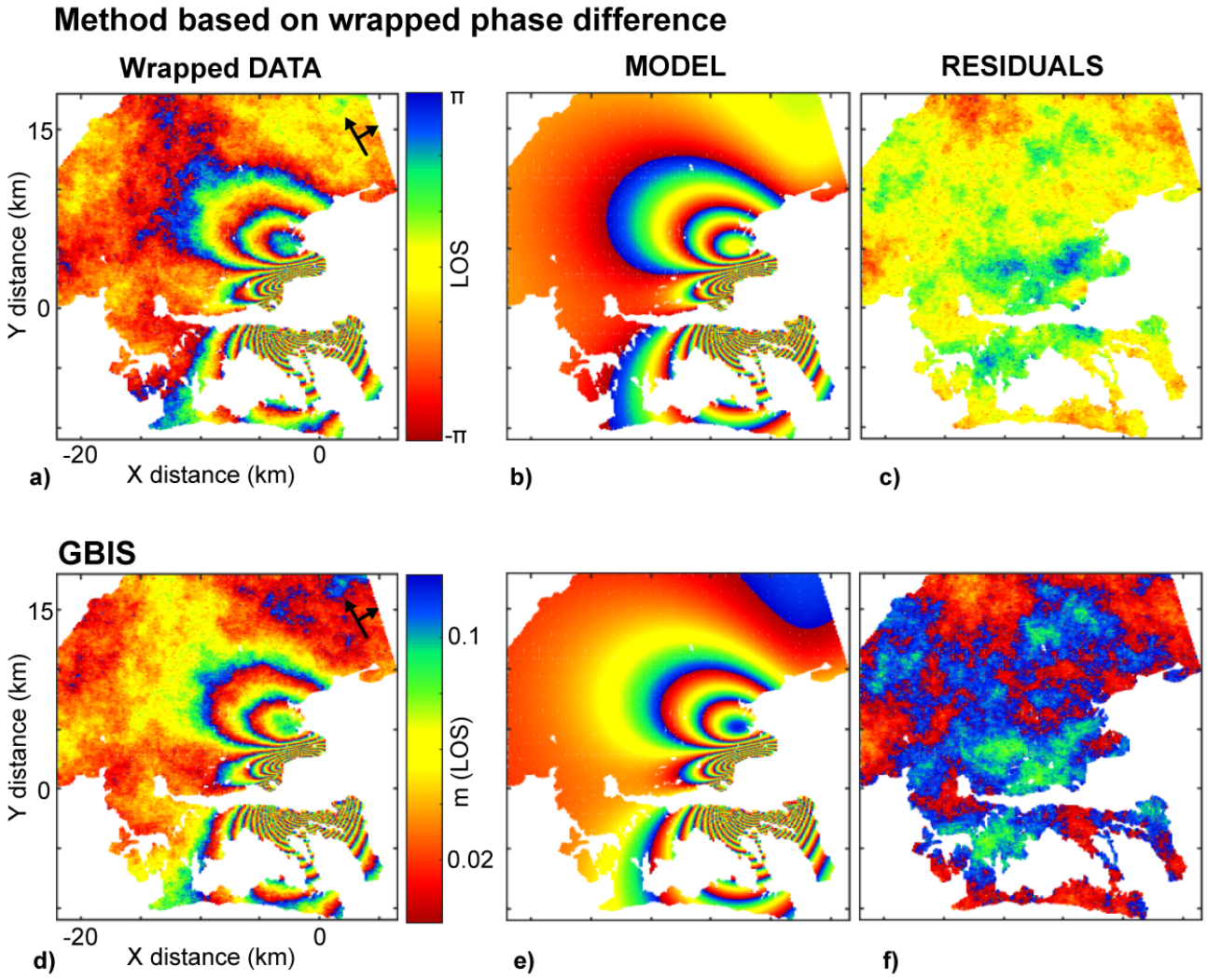

Figure S1 *a and d) Simulated wrapped data. b and e) Predicted displacements for the respective rectangular dislocation model using the MAP solutions (see Table S2). c and f) Related residuals Each fringe (full colour cycle) represents 2π radians of phase change corresponding to 2.8 cm of range change in the LOS direction. Results in panels b-c were obtained using the method based on the wrapped phase differences, while results in panels e-f were obtained with GBIS.*

Table S2 *Results of the Bayesian analysis for the synthetic data.*

Parameters of the synthetic model										
	X (m)	**Y (m)**	**Z (m)**	**L (m)**	**W (m)**	**θ**	**dip**	**strike**	**Op (m)**	**ΔV(km^3)**
	-1000	1300	3300	4300	3700	0	70	75	4	63.6
Method based on the wrapped phase difference										
	X (m)	**Y (m)**	**Z (m)**	**L (m)**	**W (m)**	**θ[a]**	**dip**	**strike**	**Op. (m)**	**ΔV (x10^6 m^3)**
Optimal	-1032	1283	3296	4476	3741	0	70.05	74.66	3.84	64.3
2.50%	-1069	1253	3227	4316	3534	0	69.35	74.09	3.7	62.5
97.50%	-995	1323	3353	4599	3964	0	70.56	75.32	4.06	66.1
Lower	-10000	-10000	2800	1000	1000	0	40	1	0	
Upper	10000	10000	4000	6000	5000	0	85	90	5	
GBIS										
	X (m)	**Y (m)**	**Z (m)**	**L (m)**	**W (m)**	**θ[a]**	**dip**	**strike**	**Op. (m)**	**ΔV (x10^6 m^3)**
Optimal	-992	1287	3340	4281	3828	0	69.89	74.91	3.91	64.1
2.50%	-1028	1253	3278	4174	3600	0	69.44	74.35	3.77	62.6
97.50%	-965	1325	3402	4388	3993	0	70.52	75.66	4.12	65.7
Lower	-10000	-10000	2800	1000	1000	0	40	1	0	
Upper	10000	10000	4000	6000	5000	0	85	90	5	

*Notes. X and Y are the coordinates of the centre of the RD. Z is the depth of the centre of the RD with respect to the surface (positive downward). θ is the angle between the RD upper edge and the intersection of the RD plane with the free surface. L and W are the length and width, respectively. Op. is the opening. ΔV is the volume change calculated with the formula ΔV=L*W*Op.*
Optimal is the MAP solution. 2.50% and 97.50% are the lower and upper bounds of the 95% confidence interval. Prior lower and upper are the bounds of the prior distribution used for the inversion.

[a] *Parameter held fixed.*

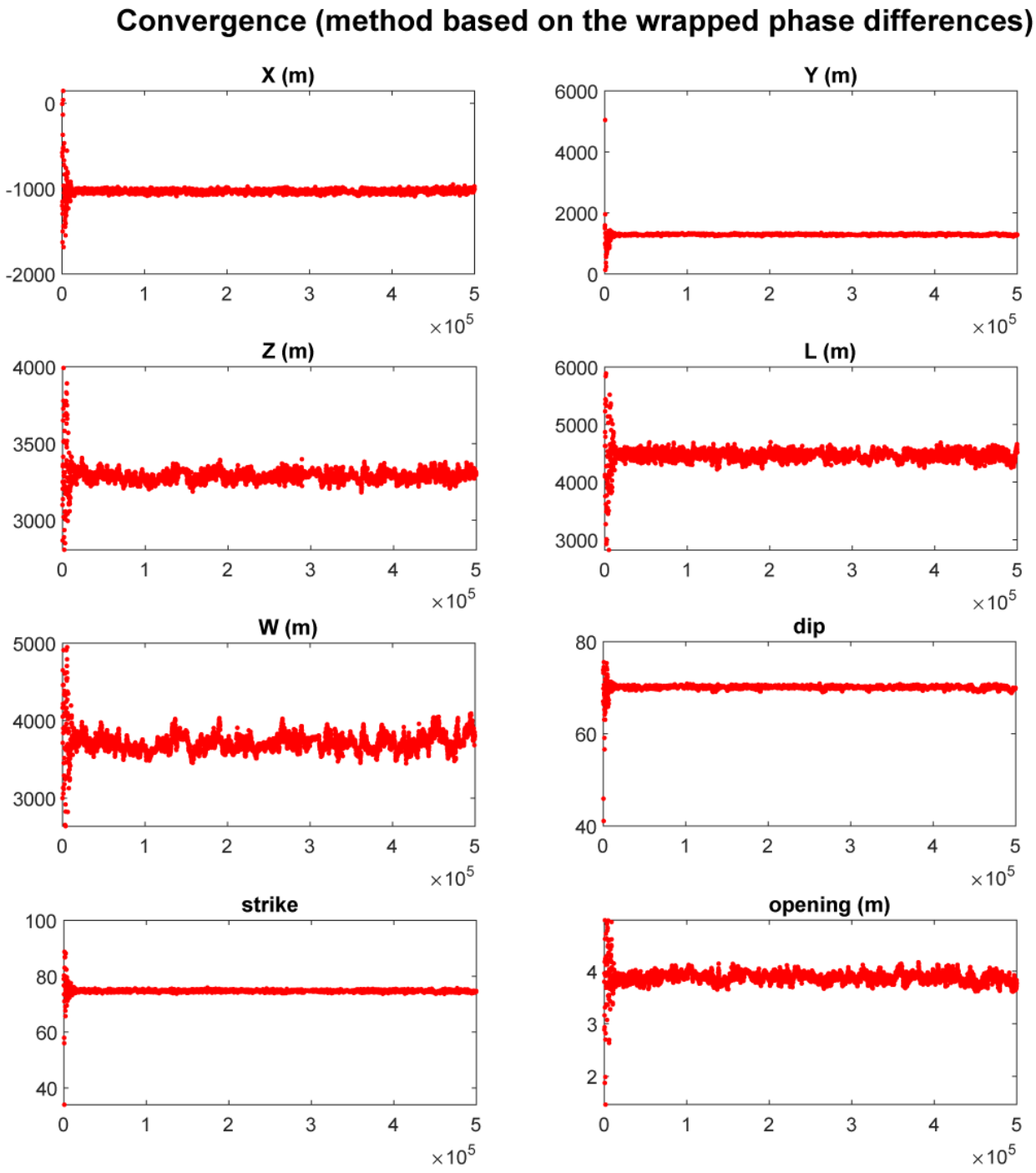

Figure S2 *Trace plots for the model parameters (see Table S1) obtained with the method base on the wrapped phase difference. On the horizontal axes are reported the number of samples.*

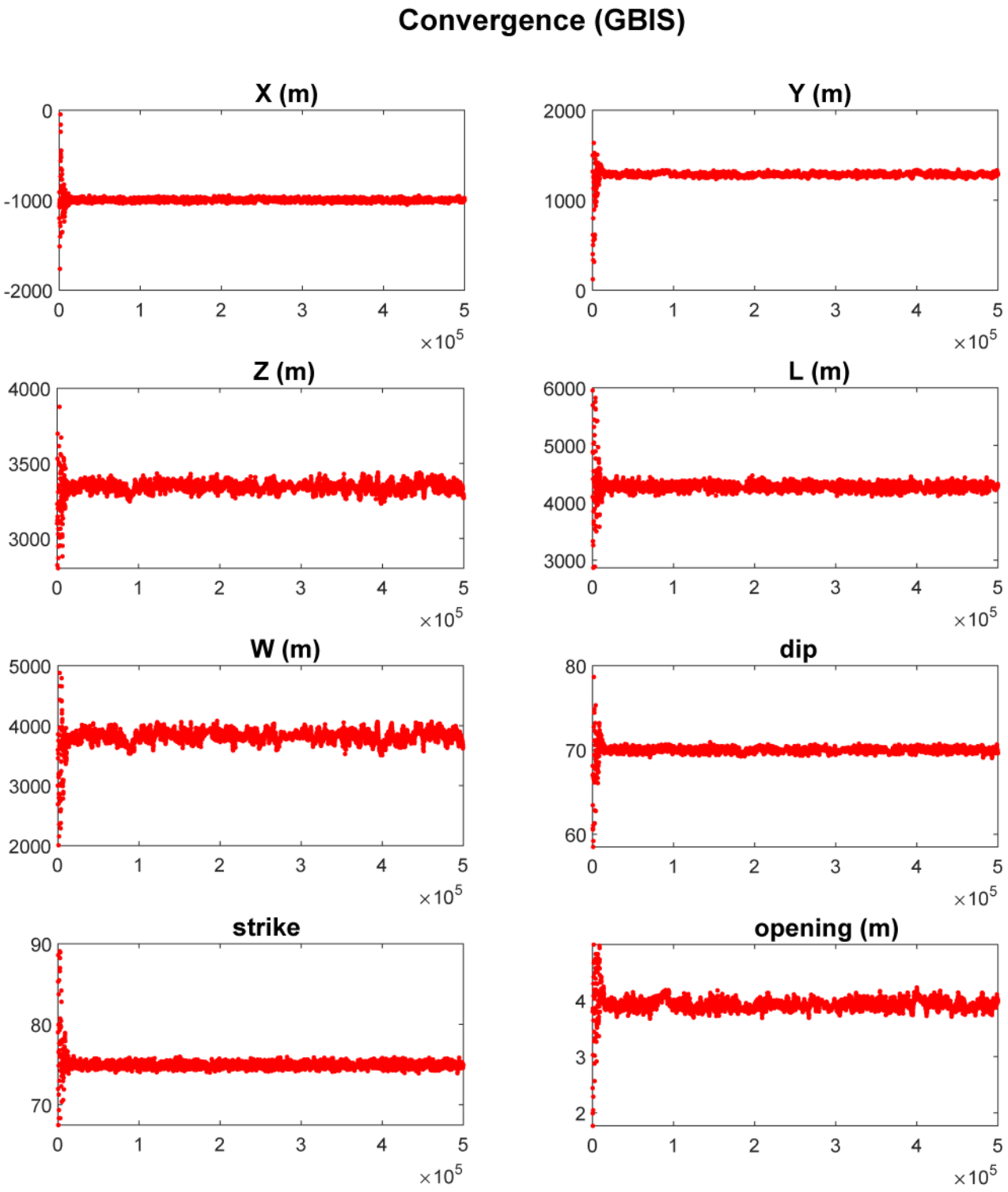

Figure S3 *Trace plots for the model parameters (see Table S1) obtained with GBIS. On the horizontal axes are reported the number of samples.*

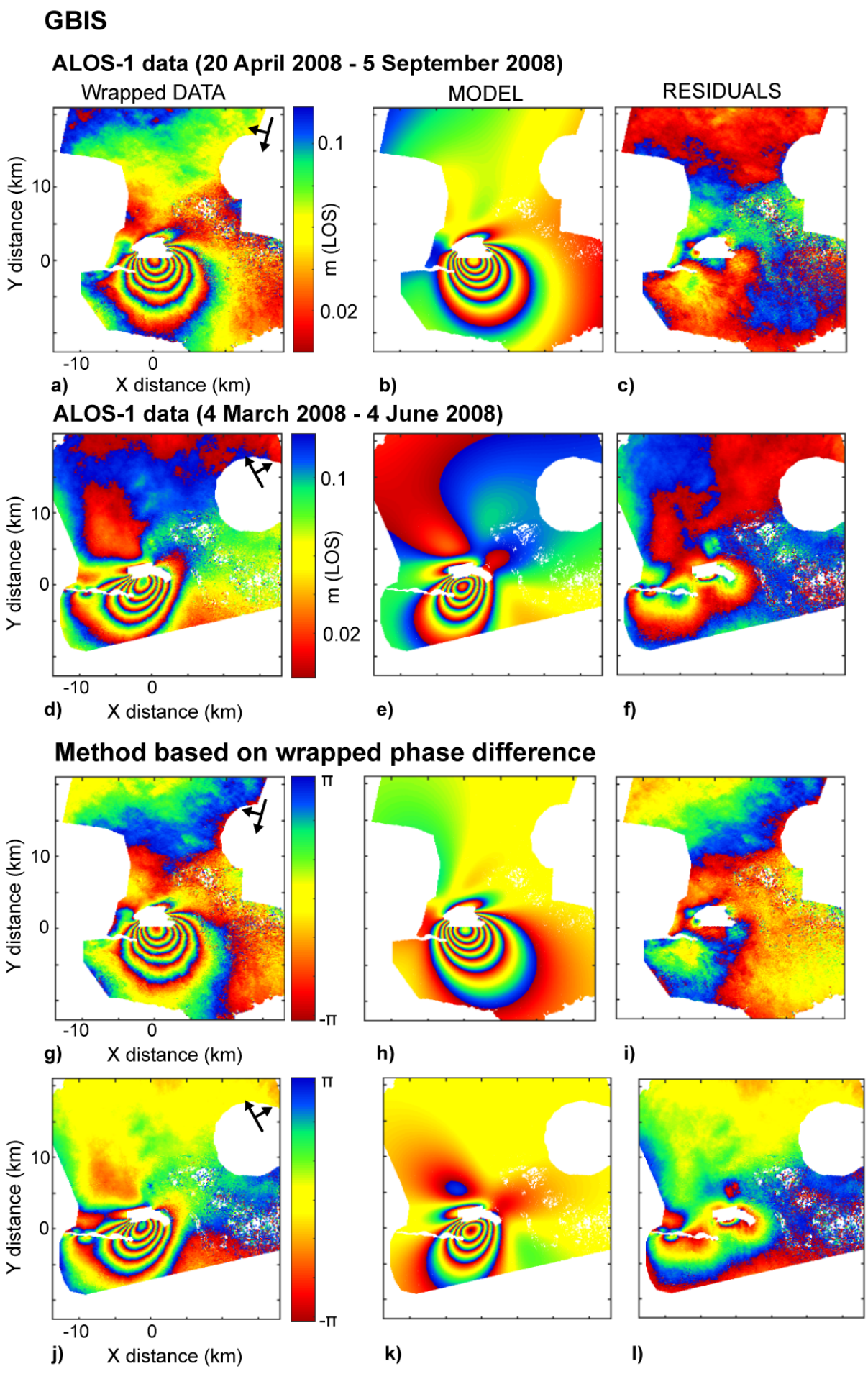
GBIS
ALOS-1 data (20 April 2008 - 5 September 2008)
Wrapped DATA
MODEL
RESIDUALS
0.1
m (LOS)
0.02
Y distance (km)
10
0
-10
0
X distance (km)
a)
b)
c)
ALOS-1 data (4 March 2008 - 4 June 2008)
d)
e)
f)
Method based on wrapped phase difference
π
-π
g)
h)
i)
j)
k)
l)

Figure S4 *a and g) Wrapped ALOS-1 phase for descending track 474. d and j) Wrapped ALOS-1 phase for the ascending track 133. b, e, h, k) Predicted displacements for the respective rectangular dislocation model using the MAP solutions (see Table S3). c, f, i, l) Related residuals Each fringe (full colour cycle) represents 2π radians of phase change corresponding to 11.8 cm of range change in the LOS direction. The local origin for all panels is 91°26'W and 0°93'S.*

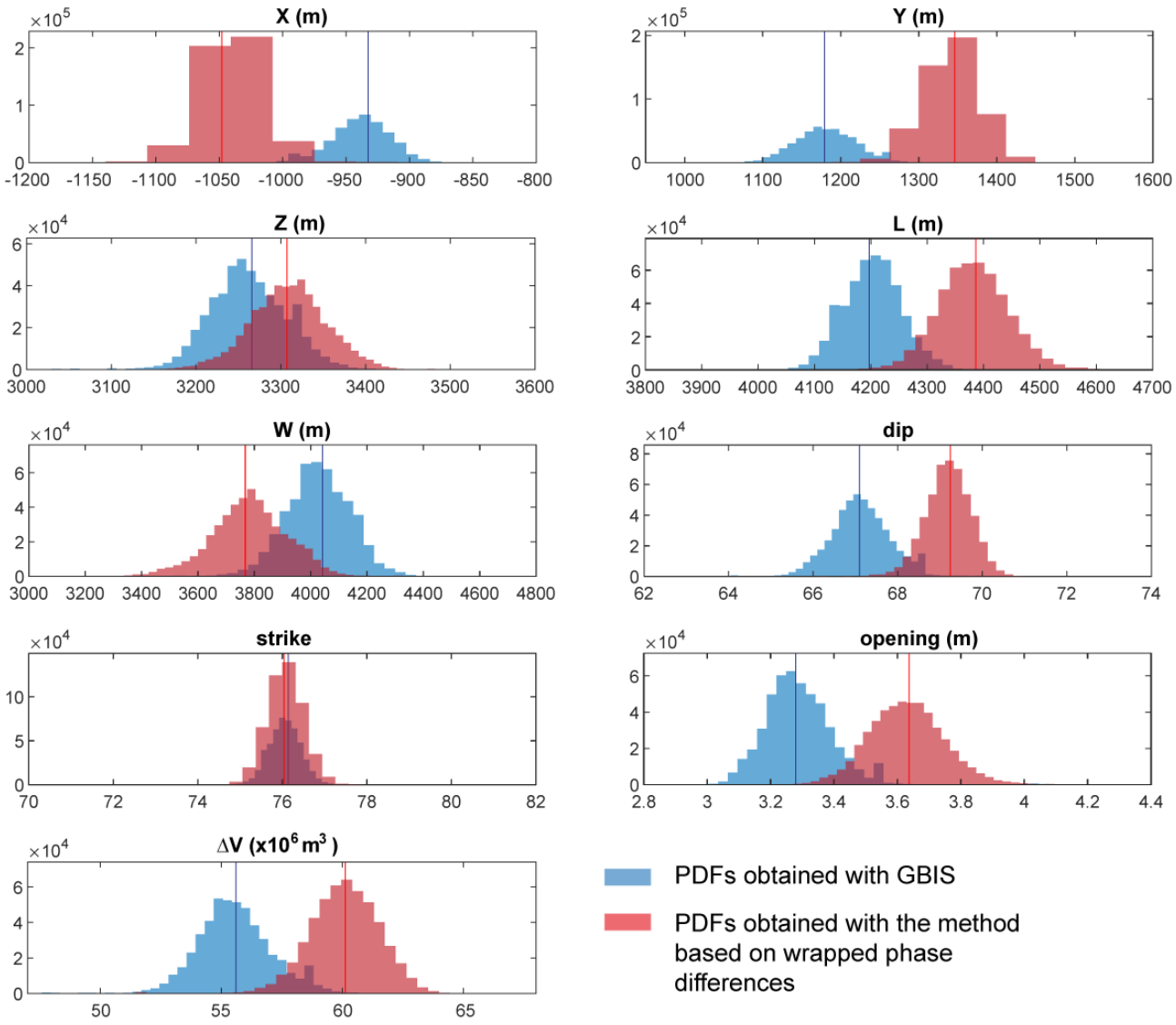

Figure S5 *Posterior probability density distribution (PDFs) for each individual model parameter from the jointly inversion of ALOS-1 ascending and descending data usind both the new method and GBIS. The red and blue lines representing the MAP solutions obtained with the new method and GBIS, respectively.*

Table S3 *Results of the Bayesian analysis for the jointly inversion of ALOS-1 data.*

GBIS										
	RD dike									
	X (m)	**Y (m)**	**Z (m)**	**L (m)**	**W (m)**	**θ[a]**	**dip**	**strike**	**Op. (m)**	**ΔV (x10^6 m^3)**
Optimal	-933	1179	3266	4197	4041	0	67.09	76.14	3.28	55.6
2.50%	-991	1107	3164	4097	3717	0	65.73	75.29	3.1	52.5
97.50%	-894	1273	3351	4313	4240	0	68.56	76.83	3.56	58.8
Lower	-10000	-10000	2800	1000	1000	0	40	1	0	
Upper	10000	10000	4000	6000	5200	0	85	90	5	

Method based on wrapped phase difference										
	RD dike									
	X (m)	**Y (m)**	**Z (m)**	**L (m)**	**W (m)**	**θ[a]**	**dip**	**strike**	**Op. (m)**	**ΔV (x10^6 m^3)**
Optimal	-1048	1346	3307	4386	3768	0	69.24	76.04	3.64	60.1
2.50%	-1088	1268	3215	4260	3474	0	67.97	75.19	3.4	57.1
97.50%	-992	1410	3402	4512	4039	0	70.21	76.98	3.89	62.8
Lower	-10000	-10000	2800	1000	1000	0	40	1	0	
Upper	10000	10000	4000	6000	5000	0	85	90	5	

*Notes. X and Y are the local coordinates of the centre of the RD with respect to the local origin (see Figure S4a and d) at 91° 26' W and 0° 93' S. Z is the depth of the centre of the RD with respect to the surface (positive downward). θ is the angle between the RD upper edge and the intersection of the RD plane with the free surface. L and W are the length and width, respectively. Op. is the opening. ΔV is the volume change calculated with the formula ΔV=L*W*Op.*

Optimal is the MAP solution. 2.50% and 97.50% are the lower and upper bounds of the 95% confidence interval. Prior lower and upper are the bounds of the prior distribution used for the inversion.

[a] *Parameter held fixed.*

Supplementary Materials for Chapter 4

Figure S1 shows an attempt at including the very limited data from deeper (>4-6 km) magma reservoirs, at Fernandina and Hudson. Figure S1 includes also data for Axial Seamount excluded from Figure 1c, as Nooner and Chadwick, (2016) recently related its uplift to the inflation of a vertical magma conduit and no more to that of a shallow reservoir . Our results highlight an overall consistent behaviour with that of the shallower reservoirs of Figure 1c. In addition, the high rates promoting the unrest-triggered dike in <1 year are consistent with the sin-eruptive rates of Kilauea in the last 40 years (usually Q >9 x10^{-2} km^3/yr; purple line on y axis in Figure S1), which provided an almost constant migration of magma from the shallow reservoir to the Eastern Rift (Poland et al., 2014).

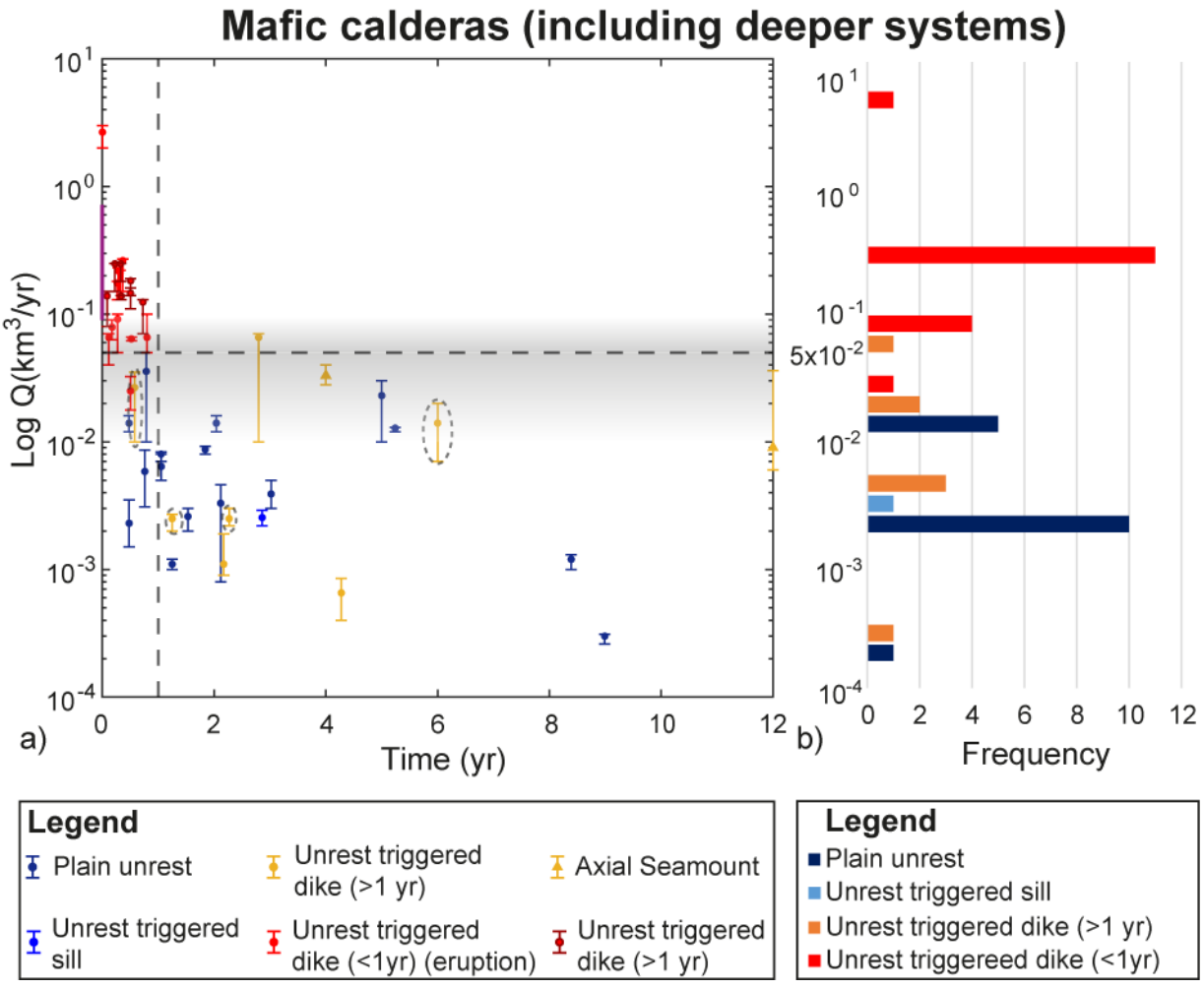

Figure S1 *a) Duration of unrest and the corresponding injection rates (Q). We included also the data from the deeper system of Fernandina, Hudson (marked with a dotted grey ellipse) and data from Axial Seamount. The dotted grey area and lines have the same meaning than those in Figure 1a and c. The purple line on the y axis marks the sin-eruptive rates of Kilauea in the last 40 years. b) Histogram of frequency of the rates associated with the unrest episodes.*

Table S1 *Geodetic data from the deeper systems of Fernandina and Huston and from Axial Seamount.*

	Start	End	V(km^3)	Q (km^3/year)	Qe (km^3/year)	Code	Depth (km)	Time (yr)	References
Fernandina	18/01/2003	26/04/2005	0.00507	0.0025	0.0022-0.003	3[a]	4-6	2.27	(Chadwick et al., 2011)
Fernandina	09/08/2005	07/11/2006	0.00293	0.0025	0.002-0.0027	3	4-6	1.25	(Chadwick et al., 2011)
Fernandina[b]	28/09/2007	26/04/2008	0.0154	0.0266	0.01-0.035	3[a]	4-6	0.578	(Bagnardi & Amelung, 2002)
Hudson	2004	2010		0.014	0.007-0.02	3[a]	9-12		(Delgado et al., 2014)
Axial Seamount[c]	1999	2011		0.009	0.006-0.036	3[a]	3.5-4	12	(Chadwick et al., 2006; Nooner & Chadwick, 2009; 2016)
Axial Seamount	2011	2015		0.033	0.028-0.040	3[a]	3.5-4	4	(Nooner & Chadwick, 2016)

Start and end are the dates of the onset and the end of the unrest. Time is the duration of the unrest. V and Q are respectively the volume and the rates estimated from the inversion of geodetic data. Q_e is the interval of confidence of the rates. Code is referred to the outcome of the unrest (0=non-eruptive; 1=Unrest-triggered sill; 2= unrest-triggered dike >1 year; 3=unrest-triggered dike <1 year). Depth is the depth of the modelled source (with respect to the surface).

[a] *The dike fed an eruption.*

[b] *The eruption occurred 1 year after the end of this inflation. For this reason, we classified this inflation as unrest triggered dike >1 year (see point5 in the Method section).*

[c] *Chadwick et al., (2006) estimated rates of about 1.4 $x10^{-2}$ km^3/year from 2000 to 2004. Then, rates decrease to a values of about 7.5 $x10^{-3}$ km^3/year (Nooner & Chadwick, 2009; 2016).*